Study of Complex Magnetic Permeability and Structural Properties of Nanocrystalline Fe-Cu-M-Si-B (M=Mo, Cr & W) Alloys

BY
PRITISH KUMAR ROY
ROLL No - 0055509
SESSION: 2000-2001

A THESIS SUBMITTED TO THE DEPARTMENT OF PHYSICS KHULNA UNIVERSITY OF ENGINEERING AND TECHNOLOGY IN PARTIAL FULFILMENT OF THE REQUIREMENT FOR THE DEGREE OF MASTER OF PHILOSOPHY

DEPARTMENT OF PHYSICS
KHULNA UNIVERSITY OF ENGINEERING & TECHNOLOGY
KHULNA-920300, BANGLADESH

MAY, 2007

KHULNA UNIVERSITY OF ENGINEERING & TECHNOLOGY
DEPARTMENT OF PHYSICS
CERTIFICATION OF THESIS WORK

A THESIS ON

STUDY OF COMPLEX MAGNETIC PERMEABILITY AND STRUCTURAL PROPERTIES
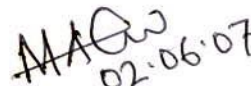OF NANO CRYSTALLINE Fe-Cu-M-Si-B (M=Mo, Cr & W) ALLOYS

By
PRITISH KUMAR ROY

has been accepted as satisfactory in partial fulfillment for the degree of Master of Philosophy in
Physics and certified that the student has demonstrated a satisfactory knowledge on the field
covered by this thesis in an oral examination held on June 02, 2007.

1. Professor Dr. Shibendra Shekher Sikder
    Department of Physics
    Khulna University of Engineering & Technology
    Khulna-920300

    ....
    Chairman & Supervisor

2. Head
    Department of Physics
    Khulna University of Engineering & Technology
    Khulna-920300

    ......02.06.07......
    Member

3. Dr. A. K. M. Abdul Hakim
    Chief Engineer and Head
    Materials Science Division
    Atomic Energy Centre, Dhaka-1000

    ....
    Member & Co-Supervisor

4. Professor Dr. Md. Mahbub Alam
    Department of Physics
    Khulna University of Engineering & Technology
    Khulna-920300

    ......02.06.07......
    Member

5. Md. Abdullah Elias Akhter
    Assistant Professor
    Department of Physics
    Khulna University of Engineering & Technology
    Khulna-920300

    Akhter 02.06.07
    Member

6. Professor Dr. Md. Feroz Alam Khan
    Department of Physics
    Bangladesh University of Engineering & Technology
    Dhaka-1000

    ....
    Member (External)

CERTIFICATE

This is to certify that this thesis which the candidate has presented for M. Phil degree has been done by the candidate himself and does not contain any matrix extracted from elsewhere or from a work published by any body else. The work of this thesis has not been presented for another degree or diploma in any other university or institute. No other person's work has been used without due acknowledgement.

Supervisor

Candidate

TO MY FATHER
AND
LATE MOTHER

Acknowledgement

ABSTRACT

The Fe-Cu-M-Si-B (M=Mo, Cr & W) alloys show excellent soft magnetic properties when they are heated just above the crystallization temperature of the amorphous state and produce homogeneous ultra fine grain of α-Fe(Si) with bcc structure having average grain diameter $D_g = 7 - 37$nm. DTA runs for these three samples show the existence of two exothermic peaks one for α-Fe(Si) and other for Fe_3B. Crystallization temperatures and activation energies of these two phases are studied by DTA. All the alloys have been annealed in the temperature range 450°C – 675°C for 30 minutes and taken under XRD experiment in order to study the effect of structural parameters such as lattice parameter, grain size, silicon content of the nanocrystalline α-Fe(Si) grains on the initial permeability. Structural parameters are found to depend on the metalloid content of the alloy and also correlated with the magnetic properties. The temperature and frequency dependence of initial permeability, imaginary part of complex permeability and relative quality factor of amorphous and devitrified toroid shaped samples have been measured with the help of an impedance analyzer. The initial permeability for the optimum annealed samples has been found to be order of 10^2 to 10^3 as compared with 250 to 300 for its amorphous counter part. The suitable annealing temperatures for maximum permeability, for frequency independence of permeability, for highest quality factor and effective frequency band have been found out experimentally for these samples. Curie temperature measurements are made by using a furnace in which the heating wire is wounded in accordance with the bifilar technique. We have also studied the effects of Cr addition for Fe in FINEMET alloy.

Contents

Chapter-I Introduction

Chapter-II Preparation of Nanocrystalline Amorphous Ribbon by Rapid Quenching Method

Chapter-III Theoretical Aspect

Chapter-IV Experimental Details

Chapter-V Results and Discussion

Chapter-V I

List of Figures

List of Tables

List of symbols

TM	=	Transition metal
TM-M	=	Transition metal metaloid
DTA	=	Differential Thermal Analysis
Tm	=	Melting temperature
Tg	=	Glass transition temperature
Tx	=	Crystallization temperature
λ	=	Wave length of the X-ray
I	=	X-ray beam intensity
μ_a	=	Absorption coefficient
μ_m	=	Mass absorption coefficient
XRD	=	X-ray diffraction
θ	=	Diffraction angle
μ	=	Permeability
FWHM	=	Full width at half maxima
a_0	=	Lattice parameter
D_g	=	Grain size
b	=	Si(at %)
μ'	=	Real part of the complex permeability
μ''	=	Imaginary part of the complex permeability
Hc	=	Coercive field
Tp	=	Crystallization peak temperature
Tc	=	Curie temperature
$Q^*\mu'$	=	Relative quality factor
$\tan\delta$	=	Loss factor
β	=	Heating rate
Q	=	$1/\tan\delta$ (quality factor)

Chapter-I

INTRODUCTION

1.1 Introduction

Magnetism is the oldest phenomena in the history of science. It is said that magnetite or lodestone had already been found to be a natural magnet several centuries before Christ which was found mostly in the magnesia of Asia Minor. It was called magnetite from which the word magnetism was derived. Scientific investigations on magnet were first made in the sixteenth century by W. Gilbert, who studied terrestrial magnetism, magnetic conduction and so on, and found that a magnet loses its magnetism at high temperature [1.1].

Enabled by the significant content of ferromagnetic elements, mainly Fe, in the earth'crust, spontaneous magnetism and magnetic phenomena were discovered many centuries ago by ancient culture in all continents including Indian, Persian, Mesoamerican, Greek and Chinese, However, even today, magnetism is astonishingly, continuing to surprise us with the observation of new phenomena and the discovery of novel advanced materials. Magnetism has played a major role in several scientific revolutions, thus transcending their pure scientific significance for society. For example, the introduction of relatively soft magnetic steels as magnetic cores in transformers around one hundred years ago enabled the more efficient distribution of electrical energy from its source to factories, public spaces and private homes. More recently magnetic recording has been contributing very significantly to modify and improve the way of life. It is clear that the present trends in scientific and technological research in magnetism are related to the recent advances in nanosciences and nanotechnologies. With the availability of modern sophisticated and precission experimental techniques, new phenomena have been demonstrated which have stimulated the emergence of new research areas. It should be emphasized that progress is, to a large extent, being made possible by the current development of techniques for the fabrication and processing of materials with controlled characteristics on the nanoscale. Nanocrystalline ferromagnetic materials offer a new possibilities for tailoring advantageously a variety of phenomena including soft, hard and superparamagnetic behavior. The detailed properties depend upon the interaction mechanism and on the ratio between structural and magnetic correlation length.

Over the past several decades, amorphous and more recently nanocrystalline materials have been investigated for applications in magnetic devices requiring

1

magnetically soft materials such as transformers, inductive devices, etc. Most recently, research interest in nanocrystalline soft magnetic alloys has dramatically increased. This is due, inpart, to properties common to both amorphous and crystalline materials and the ability of these alloys to compete with their amorphous and crystalline counterparts. The benefits found in the nanocrystalline alloys stem from their chemical and structural variations on a nanoscale which are important for developing optimal magnetic properties.

Amorphous soft magnetic alloys are now well accepted and mature materials. At first the great interest in amorphous metals stems from reports by Duwaz et.al [1.2] on the preparation and properties of amorphous metallic alloys. Simpson and Brandley [1.3] appear to have been the first to point out that the amorphous alloys are expected to have no magnetocrystalline anisotropy and should have very low coercivity. Progress in this field is often characterized by further improvements according to specific requirements of particular applications. Recent advances have been reviewed in several papers [1.4-1.10]. Basically there are two groups of amorphous alloys. On the one hand the Fe rich magnetic alloys which exhibit the highest saturation flux densities among the amorphous materials and which are based on inexpensive raw materials. The Co- based metallic glasses on the other hand are distinguished by their low or vanishing magnetostriction leading to highest permeabilities and lowest core losses. Both groups of metallic glasses are in current commercial use. Fe rich alloys are mainly used in power electrical devices whereas the Co- based alloys dominates in inductive components for electronics. The losses of the magnetic material used in this type of high frequency device can be controlled by the ribbon thickness. Ribbon thickness is therefore one of the important parameter for optimizing magnetic losses in the device.

Nanocrystalline soft magnetic materials were first reported in 1988 by Yoshizawa et.al [1.11]. Exploitation of this novel material in practical applications started shortly after the discovery and manufactured by Hitachi Co. Ltd. under the trade names FINEMET[1.12] and VITROPERM[1.13]. The originally proposed composition was $Fe_{73.5}Cu_1Nb_3Si_{13.5}B_9$ alloy[1.14-1.19]. The alloy in the form of ribbon with amorphous state has been produced initially by rapid solidification technique.

An appropriate thermal treatment above the crystallization temperature corresponding to this alloy gives rise to extraordinary soft magnetic properties. A heat

treatment around 555°C i.e. above the crystallization temperature of the amorphous state, produces a homogeneous, ultrafine grain structure of α-Fe(Si) with bcc structure having a typical grain diameter D_g = 10-20nm and random texture. Usually on crystallization of amorphous alloys much larger grains with D_g = 0.1-1 μm is obtained. The formation of these nanocrystalline structures is ascribed to the combined addition of Cu and Nb, which both are not soluble in α-Fe. Hereby Cu is thought to increase the nucleation of α-Fe grains, whereas Nb lowers its growth rate [1.14]. The ultra fine grain structures of these alloys give rise to excellent soft magnetic properties that are superior to those of Co-based amorphous alloys. Soft magnetic properties of nanocrystalline alloys are strongly dependent on the grain size and grain boundary structure. The excellent soft magnetic properties of this alloys have been successfully explained by Herzer[1.15] on the basis of random anisotropy model (RAM). The model was first proposed by Alben et.al.[1.21] for amorphous magnetic alloys.

Herzer explained the grain size dependence of the coercivity based on random anisotropy model considering the nanocrystalline materials as single phase magnetic system. Harnando et.al.[1.22] extended this model for two phase materials and was able to explain the thermal dependence of the coercivity[1.21,1.23-1.24]. The explanation of the soft magnetic properties of this nanocrystalline alloy is based on the random anisotropy model and has been consolidated by Herzer[1.14]. It is related to the ratio of the exchange correlation length of the orientation fluctuation of randomly distributed local easy axes, or in other words, the ratio of the domain wall thickness to the mean crystallite size. This model explained the main feature of the dependence of coercivity on grain size[1.25-1.26]. Recently, experiments showed that magnetic hardening takes place at the very beginning of nanocrystallization[1.27-30] which falls out of the capabilities of Herzer's description.

The novel nanocrystalline soft magnetic materials is basically a two phase material having various volume fraction of nanocrystalline α-Fe(Si) phase and remaining amorphous phase. The ratio of these two phases can be adequately controlled through heat treatment, temperature an time. Thus as a function of measuring temperature, a single sample combines a variety of phenomena ranging from soft to hard and finally to super-paramagnetic behavior[1.31] depending on the ratio of the exchange correlation length to the average crystallite size and also on the crystallized volume fraction as affected by thermal treatments.

This review is intended to summarize recent developments in the synthesis, structural characterization, properties and application of nanocrystalline and amorphous magnets. The term "Nanocrystalline alloy" will be used for those alloys that have a majority of grain diameters in the typical range from $\approx$ 1-50nm. This term will include alloys made by rapid solidification, deposition and solid state reaction methods where the initial material may be in the amorphous state and subsequently crystallized. We consider processing routes and method to control chemistry and microstructural morphology on increasingly smaller length scales and various developing experimental techniques which allow more accurate and quantitative probes of structure including magnetic domain structure on smaller length scales. The impact of microstructural control on the development of state of the art soft magnetic materials.

Conventional physical metallurgy approaches to improving soft ferromagnetic properties involve tailoring the chemistry and optimizing the microstructure. The significance in the optimizing of the microstructure is recognition of the fact that a measure of the magnetic hardness is roughly inversely proportional to the grain size (D_g) for grain sizes exceeding $\approx$ 0.1-1μm where the grain size exceeds the domain (Bloch) wall thickness (δ_w). In such cases grain boundaries act as impediments to domain wall motion, and thus fine grain materials are usually magnetically harder than large grain materials. Significant recent developments in the understanding of magnetic coercivity mechanisms have lead to the realization that for very small grain sizes $D_g \sim 100$ nm[1.14-1.15, 1.26, 1.32-1.34]. H_c decreases rapidly with decreasing grain size. This can be understood by the fact that the domain wall thickness, δ_w exceeds the grain size, now sample several grains so that fluctuations in magnetic anisotropy on the grain size length scale are irrelevant to domain wall pinning. This important concept suggests that nanocrystalline and amorphous alloys have significant potential as soft magnetic materials. Soft magnetic properties requires that nanocrystalline grain be exchanged complied and therefore any of the processing routes yielding free standing nanoparticles must include a compaction method in which the magnetic nonoparticle end up exchange coupled. Similar ideas have been stated for so called spring exchange hard magnetic materials [1.35-1.37]. The development of nanocrystalline materials for soft magnetic application is an emerging field for which we will try to offer a current perspective that may well evolve further with time.

It is well accepted that good magnetic properties are obtained when $D \ll L_{ex}$ where L_{ex} is the ferromagnetic exchange length [1.22, 1.38] and D is the average grain diameter. According to calculation, for Fe-Si alloy $L_{ex} \sim 35$ nm[1.39]. Respond of nanostructured magnetic material to the frequency of the external field can be controlled by the varying grain size and their distribution. The magnetic properties of this type of amorphous nanostructured material can be tailored in different ways. These freedoms of tailoring the magnetic properties enhance the scope of their technical applications. Such a Fe-Si-B based amorphous nanostructured alloys with composition $Fe_{73.5}Cu_1Nb_3Si_{13.5}B_9$, which is widely studied by different authors and several papers [1.40-1.42] have come out.

One of the important features of this magnetic system is that one can play with different compositions, annealing temperatures and time to control the grain size and their distribution upon which the magnetic properties of these new materials strongly depend. In choosing the composition one has to consider the magnetic components like Fe, Co, Ni, Al etc. the crystallization component e.g. Cu and the component Nb for stabilizing the nanocrystal growth by inhibiting the grain growth and glass forming materials like Si, C, B etc. Amorphous ferromagnetic materials based on Fe-Si-B show good magnetic properties when they are heat-treated below their crystallization temperature. While the Fe-Cu-Nb-Si-B alloys exhibit extraordinary high permeability, two orders of magnitude higher than their conventional Fe-Si-B alloys due to the heat treatment just above the crystallization temperature for a specific time.

$Fe_{73.5}Cu_1Nb_3Si_{13.5}B_9$ alloy with a nanocrystalline grain structure is a very attractive soft magnetic material since it exhibits excellent permeability while maintaining a high saturation magnetization [1.11, 1.43-1.44]. This material is prepared by annealing a melt-spun amorphous nanocrystalline alloy at temperature in the range of $520-580^0C$. The microstructure produced by this process consists of ultrafine grains of a metastable b.c.c. phase. The average grain size is approximately 10nm, and it has been thought that the random distribution of these ultrafine grains causes a reduction of the net magnetocrystalline anisotropy [1.44-1.46, 1.15]. This ultrafine grain structure is achieved by a combined addition of Cu and Nb into Fe-Si-B amorphous alloy [1.44]. Since Cu is virtually insoluble in Fe, it has been speculated that the inhomogeneity of Cu occurs at an initial stage of crystallization, which causes an increased number of nucleation sites of the b.c.c. crystalline phase. It has been thought that the Nb addition retards the grain growth during the crystallization process, and hence that the combined addition of Cu and Nb results in

the formation of fine grain structure. Our present study compares the results of nanocrystalline composition of $Fe_{73.5}Cu_1Nb_3Si_{13.5}B_9$ alloys with the replacement of Nb by W and Mo such as compositions are $Fe_{73.5}Cu_1W_3Si_{13.5}B_9$ and $Fe_{73.5}Cu_1Mo_3Si_{13.5}B_9$ alloys. Another composition $Fe_{71.5}Cr_2Cu_1Nb_3Si_{13.5}B_9$ having Cr substituted for Fe to observe the crystallization and magnetic properties.

1.2 Technical Consideration of Nanocrystalline Soft Magnetic Materials

The development of nanocrystalline soft magnetic materials for applications requires attention to variety of intrinsic magnetic properties as well as development of extrinsic magnetic properties through an appropriate optimization of the microstructure. As intrinsic properties we take to mean microstructure insensitive properties. Among the fundamental intrinsic properties which depend on alloy chemistry and crystal structure as well as the saturation magnetization, Curie temperature, magnetocrystalline anisotropy and the magnetostrictive can be considered as extrinsic in that for a two-phase material they depend on the microstructure. The desire for large magnetic induction typically limits choices to alloy of Fe and Co. These are the elemental transition metal magnets with the largest atomic dipole moments. Curie temperature are also largest for elemental Fe (770°C) and Co (1100°C), suggesting the use of Fe or Co or Fe-Co alloys especially in high temperature applications. Magnetocrystalline anisotropy and magnetosriction, which are determining factors in the case in which the magnetization vector can be rotated into the direction of the applied field are also sensitively dependent on alloy chemistry. Many important soft magnetic alloy systems have zero crossings of the magnetocrystalline anisotropy, or magnetostriction coefficients which can be exploited in the development of premiere nanocrystalline soft magnetic materials.

Though new discoveries continue to be made in this area, it can be safety stated that a more wide-open area in the development of magnetic materials for applications is the fundamental understanding and exploitation of micro structural influence on the extrinsic magnetic properties. Important micro structural features include grain size, shape distribution, and orientation, defect concentrations, compositional inhomogeneities, magnetic domains and domain walls. The interaction of magnetic domain walls with microstructure impediments to their motion is of particular importance to the

understanding of soft magnetic materials including the magnetic permeability and the coercivity, which typically have an inverse relationship. Remanant magnetization, squarencess of the hysteresis loop and magnetic anisotropy are also important in determining magnetic softness. Magnetic hysteresis is a useful attribute of a permanent magnet material in which we wish to store a large metastable magnetization. On the other hand, a large class of applications requires small hysteresis losses per cycle. These include application as inductors, low and high frequency transformer, alternating current machines motors, generators and magnetic amplifiers.

1.3 Organization of the Thesis Work

The preparation procedures are described in chapter-2. The theroretical aspects of the stability of amorphous alloys, theories of X-ray diffraction and permeability are described in chapter-3, Chapter-4 contains the experimental details including Differential Thermal Analysis (DTA), X-ray Diffractometer and Impedance Analyzer.

The details of the results regarding DTA, X-ray diffraction (XRD) method after heat treatment of these compositions ($Fe_{73.5}Cu_1W_3Si_{13.5}B_9$, $Fe_{73.5}Cu_1Mo_3Nb_3Si_{13.5}B_9$ and $Fe_{71.5}Cr_2Cu_1Nb_3Si_{13.5}B_9$) at different temperatures, annealing effects on frequency dependence of initial complex permeability and temperature dependence of initial permeability are discussed in chapter-5. It also contains comments on the suitability of the specimens studied, in respect of relative quality factor, loss factor and the frequency range in which these materials can be used. Chapter-6 contains conclusions, achievement of the work and future suggestions on the present work.

Chapter-II

PREPARATION OF NANOCRYSTALLINE AMORPHOUS SOFT MAGNETIC MATERIALS BY RAPID QUENCHING METHOD

2.1 Introduction

The study of metallic glasses dates back to the pioneering work of Pol Duwez at Caltech in the 1950s. Duwez employed atomization [2.1] prior to splat quenching [2.3-2.4]. Ferromagnetic amorphous alloys were first reported by Mader and Nowik[2.5]. Soon after, Tsuei and Duwez[2.6] reported splatquenched amorphous ferromagnets with interesting soft magnetic properties. Rapid solidification processing is reviewed only in a cursory manner here, citing techniques, which have been employed to produce materials.

Nanocrystalline alloys can be described in general as $TL_{1-x}(TE, M, NM)_x$, where TL denotes a late ferromagnetic transition metal element, TE is an early transition metal element, M is a metalloid and NM is a noble metal. This composition usually has $x<0.20$ i.e. with as much late ferromagnetic transition metals (TL of Co, Ni, or Fe) as possible. The remaining early transition metals (TE = Zr, Nb, Hf, Ta etc.) and metalloids (M =B, P, Si etc.) are added to promote glass formation in the precursor. The noble metal elements (TN = Cu, Ag, Au etc.) serve as nucleating agents for the ferromagnetic nanocrystalline phase. The compositions are limited by where glass formation can occur prior to the nanocrystallization route. These alloys may be single phase (Type-I) but are generally two-phase materials with a nanocrystalline ferromagnetic phase and a residual amorphous phase at the grain boundaries (Type-II). The type-II nanocrystalline alloys might have general properties (i) relatively high resistivity ($50-80\mu\Omega$-cm) (ii) low magnetocrystalline anisotropy and (iii) increased mechanical strength. With properties such as these, nanocrystalline alloys have great potential as soft magnetic properties.

Nanocrystalline Fe-Cu-Nb-Si-B alloys have been patented by Yoshizawa et-al under the trade name FINEMET[2.7-2.8]. Soft materials based on Fe-M-Cu-B have been patented by Kojima et-al [2.9] under the trade name NANOPERM. These Fe-M-Cu-B (M =Zr, Nb, Hf,.....) nanocrystalline alloys have all been optimized to achive small magnetostrictive coefficients and concomitant large permeabilities. More recently (Fe, Co)-M-Cu-B [M= Nb, Hf, or Zr) nano crystalline alloys, called HITPERM have been shown to have attractive induction (1.6-2.1Tesla) combined with high permeabilities and high Curie temperatures. In FINMENTS α-FeSi nanoparticles with a DO_3 structure are observed, in NANOPERM α-Fe particles with BCC structure are formed. In HITPERM alloys nanocrystalline α and α-BCC and B2-FeSi (B2)-FeCo are formed with

significantly improved high temperature magnetic properties than in the former two. The new nanocrystalline alloys prepared by such techniques were used in the early works to explore the many possibilities opened up by these new rapid quenching techniques.

2.2 An Overview of Nanocrystalline Materials

Nanocrystalline amorphous ribbons can be considered as an off-shoot of amorphous materials. In fact nanocrystalline amorphous ribbon is a composite meterial where nanocrystals are embedded in an amorphous matrix. Nanocrystalline materials represent one of the most active research area in recent times for the atomic tailoring of materials with specific properties and property combinations. However, it is still in its infancy since its emergence as potential materials has just began at this stage of development. There have been glimpses of exciting new properties like super plasticity, giant magnetoresistance (GMR), transparency in opaque ceramics, enhanced homogeneity, unusual soft ferromagnetic and giant magnetocaloric effects, possessed by these materials when reduced to nanometer dimension. In addition to the understanding of the usual properties possessed by nanophase materials, there are three other associated areas, which need serious attention:

(i)   Identification and development of suitable preparation methods, especially those which are capable of providing large industrial quantities of nanometer scale materials.

(ii)   Development of processing methods for manufacturing these materials into useful size and shapes without losing there desirable nanometer size feature and

(iii)   Identification of proper characterization methods, where the nanometer size range of these materials falls just below or at the resolution limit of the conventional tools.

Nanocrystalline soft magnetic alloys have received considerable attention due to their excellent soft magnetic properties [2.10]. Small addition of Cu and Nb into Fe-Si-B amorphous materials changes considerably their crystallization process, which is executed under appropriately controlled conditions and the specific purpose of these additions are:

9

(i)   The element Cu is used for helping the formation of nuclei of ultrafine grains.

(ii)   The element Nb is used to impede the growth of the crystallites.

In this material, the nanocrystalline state is composed of a fine structure of α-Fe(Si) and is usually around 10 nm. For such an average grain size the exchange interaction dominates the magnetic behavior of randomly oriented crystallites guided by random anisotropy [2.11]. In the present thesis work two nanocrystalline alloys are prepared by replacing Nb with Mo and W of the well-accepted nanostructed $Fe_{73.5}Cu_1Nb_3Si_{13.5}B_9$ FINEMET amorphous alloys. Another nanocrystalline alloy prepared by partial substitution of Fe by Cr of FINMENT $Fe_{73.5}Cu_1Nb_3Si_{13.5}B_9$

2.3   Nanocrystalline Alloy Design Issues

Alloy design issues include issues of chemistry and processing designed to (i) optimize one of a number of important intrinsic and or extrinsic magnetic properties as well as to (ii) optimize structural or microstructural features which promote important magnetic properties. The first of these issues concerns the choice of chemistry so as to impact the intrinsic magnetization of the material. The second issue pertinent to further discussions here are alloy additions means to an end or as a precursor to producing a nanocrystalline material.

Theory/
Philosophy

```
┌─────────────┐      ┌─────────┐     ┌──────────────┐
│Slater-Pauling│     │  Phase  │     │  Eutectic of │
│    Curve     │     │ Diagram │     │ Glass Forming│
└─────────────┘      └─────────┘     │   Elements   │
                                      └──────────────┘
┌─────────────┐
│  Good Soft  │          ┌─────────────┐
│  Magnetic   │─────────▶│ Composition │
│  Qualities  │          └─────────────┘
└─────────────┘
```

```
┌─────────┐                              ┌──────────┐
│   DTA   │              ┌──────────┐    │  Herzer  │
└─────────┘              │ Melt Spin│    │ Diagram  │
                         └──────────┘    └──────────┘
┌─────────┐                              ┌──────────┐
│   SEM   │                              │Conventional│
└─────────┘                              │    XRD    │
                                         └──────────┘
```

Processing

```
┌─────────┐              ┌──────────┐
│   TEM   │              │ Isothermal│
└─────────┘              │  Anneal  │
                         └──────────┘
┌─────────┐
│   MFM   │
└─────────┘
```

Analysis

```
┌────────────┐           ┌──────────────┐   ┌───────────┐
│   SQUID    │           │Nanocrystalline│  │ Syncrotron │
│ Magnetometer│          │    Alloy     │   │    XRD     │
└────────────┘           └──────────────┘   └───────────┘

                                            ┌───────────┐
                                            │  Neutron  │
                                            │ Diffraction│
                         ┌──────────────┐   └───────────┘
┌────────────┐           │ Soft Magnetic│
│AC Permeameter│─────────▶│  Propeties  │   ┌───────────┐
└────────────┘           └──────────────┘   │    VSM    │
                                            └───────────┘
```
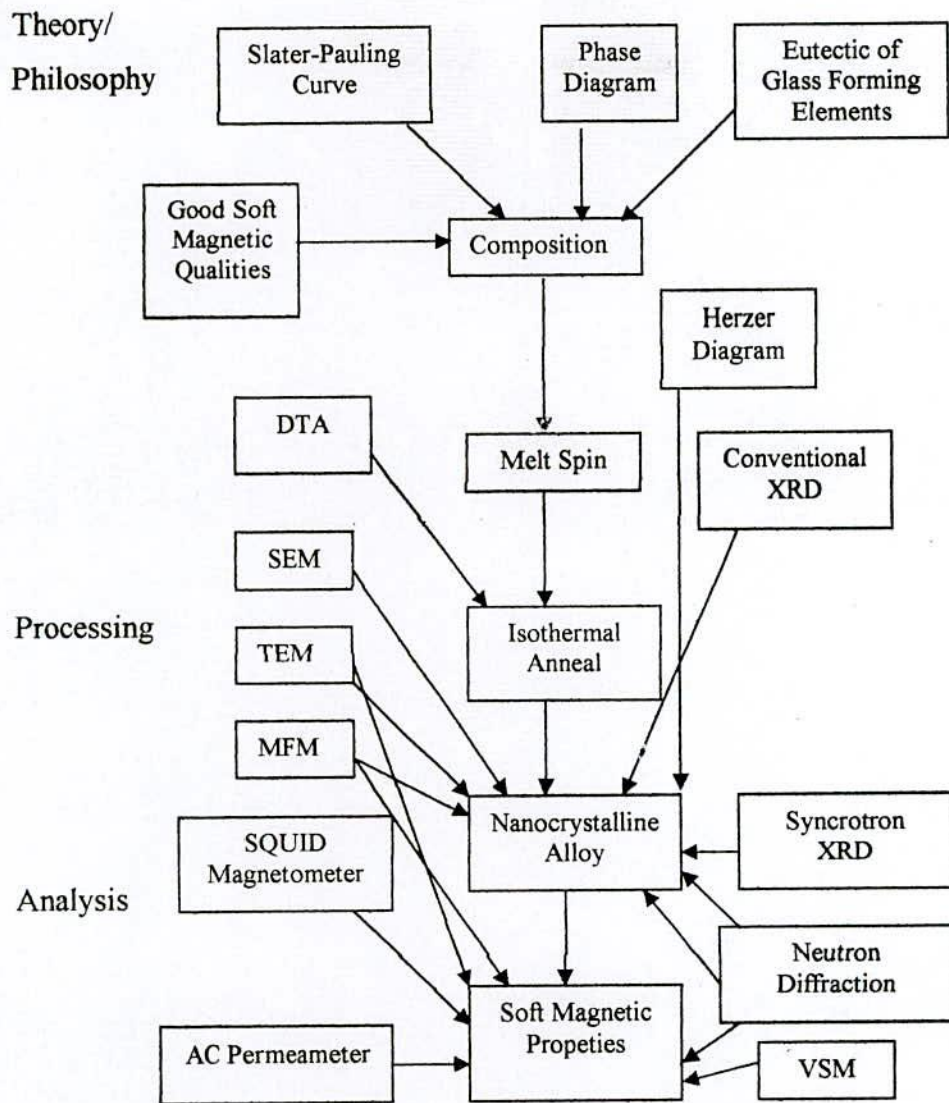
Fig.2.1   Flow chart for the consideration in designing and developing a nanocrystalline soft magnetic material from an amorphous precursor route

Alloy design issues are in many ways influenced by the processing routes used to achieve desired microstructures. Fig-2.1 illustrates a flowchart for the considerations in designing and developing a nanocrystalline soft magnetic material from an amorphous precursor route as one example of the design process. Here, we consider first the effects of alloy composition on intrinsic magnetic properties. This is followed by consideration of alloying additions necessary to produce an appropriate amorphous precursor. Typical experimental steps used to identify the structure and properties of the resulting materials are also illustrated.

2.4 Conditions for the Formation of Nanocrystalline State

The Nanocryatalline state is achieved by annealing at temperatures typically between $500\text{-}600^0$ C, which leads to primary crystallization of bcc Fe. The resulting microstructure is characterized by randomly oriented, ultrafine grains of bcc Fe-Si, 20 at % with typical grain size of 10-15nm embedded in a residual amorphous matrix which occupies about 20-30% of the volume and separates the crystallites at a distance of about 1-2nm. These features are basis for the excellent soft magnetic properties indicated by the high values of the initial permeability of about 10^5 and corresponding low coercivities of less than 1 A/m. The nanocrystalline microstructure and the accompanying soft magnetic properties are rather insensitive to the precise annealing conditions within a wide range of annealing temperature $T_a \approx 525\text{-}580^0C$. They develop in a relatively short period of time (about 10-15 minutes) and do not improve much even after prolonged heat treatment of several hours [2.12]. A typical heat treatment like T_a at 540^0C in most cases yields a nanocrystalline microstructure to the quasi-equilibrium state and characteristic for the individual alloy composition.

Only annealing at more elevated temperatures above about 600^0C leads to the precipitation of small fractions of boride compounds like $Fe_2 B$ or Fe_3B. The formation of the particular nanocrystalline structure is essentially related to the combined addition of Cu and Nb and their low solubility in bcc Fe. Copper enhances he nucleation of the bcc grains while niobium impedes coarsening and at the same time, inhibits the formation of boride compounds. The microstructure evolution is schematically illustrated in fig.2.2 and can be summarized as follows.

The phase separation tendency between Cu and Fe leads to the formation of Cu rich clusters, about 5nm in size and probably still amorphous, in the initial stage of annealing before the onset of the primary crystallization of the bcc Fe-Si phase [2.12-2.13]. The presence of Nb, hereby seems to promote the formation of these Cu rich clusters on a much finer scale than in an Nb free alloy composition [2.14]. The cluster formation causes a concentration fluctuation of Fe, since Cu substitutes for Fe. Thus, the regions in between the Cu-rich clusters provide a significantly increased density of nucleation sites for the crystallization of bcc Fe.
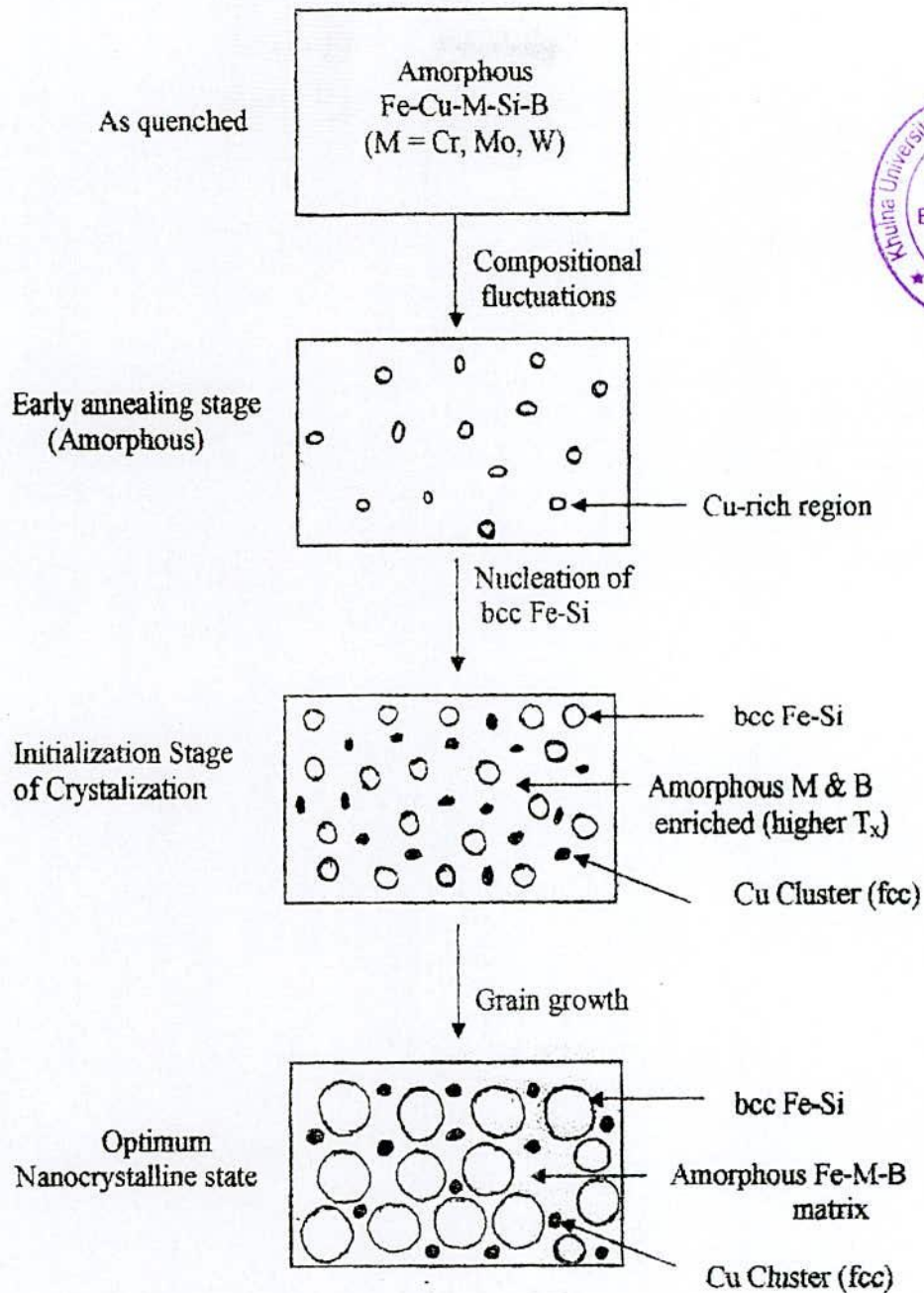
Fig.2.2   Schematic illustration of the formation of the nanocrystallization structure in Fe-Cu-Nb-Si-B alloys based on atom probe analysis results and transmission electron microscopy observation [2.12-2.13]

The consequence is an extremely fine nucleation of bcc Fe-Si crystallites at a high rate which subsequently grow in a diffusion controlled process [2.15] as the annealing proceeds further. As the bcc Fe-Si phase forms, M and B are excluded from the crystallites because of their low solubility in bcc Fe and are enriched in the residual

amorphous matrix. At the same time effectively all Si tends to be partitioned into the bcc Fe-Si phase [2.16-2.17]. The enrichment with B and in particular, with M increasingly stabilizes the residual amorphous matrix and, thus hinders coarsening of the bcc grains. The presence of M at the same time inhibits the formation of Fe boride compounds. The transformation finally causes in a metastable two-phase microstructure of bcc Fe-Si embedded in an amorphous Fe-M-B matrix.

2.5   Synthesis of Nanocrystalline Alloys

The processing method is necessary to produce alloys in the amorphous state. Circumventing the crystallization process is also necessary for alloy formation in the amorphous state, either as an end product or a precursor to nanocrystallization. The following four synthesis routes which are viable for producing alloys for larger scale applications, as opposed to thin film synthesis for microelectronic applications, for example. These synthesis are:

(i)   Powder synthesis techniques: Magnetic nanocrystals may be synthesized as free standing powders or nanoencapsulates which must then be compacted to form a bulk alloy with nanocrystalline grains. Examples of these techniques include carbon-arc synthesis, plasma torch synthesis and gas atomization techniques, among others.

(ii)   Rapid Solidification Processing: Amorphous alloys can be produced by a variety of rapid solidification processing routes. These typically require cooling rates of $> 10^4 K/sec$ for typical alloys at a eutectic composition. Examples of these techniques include splat quenching, melt-spinning, etc.

(iii)   Solidification processing of bulk amorphous alloys: Bulk amorphous alloys are formed by more conventional solidification routes with slower cooling rates. The so-called large glass forming abilities of these alloys for production of amorphous materials with much larger dimensions, thus the name bulk amorphous alloys.

(iv)   Crystallization of Amorphous Precursors: Bulk alloys with nanocrystalline grains can also be produced by solid reaction (crystallization) of an amorphous precursor.

14

2.6 Viscosity Condition for the Formation of Metallic Glass

In terms of viscosity and diffusion co-efficient we find the condition for formation of glass:

(i) The metals atomic bonding is metallic, the viscosity is lower than the diffusion co-efficient and mobility is high.

(ii) In the amorphous state viscosity becomes high and the diffusion co-efficient decreases. Atomic bounds tend to be covalent as in the case of silicate (SiO_2).

2.7 Conditions Necessary for Preparing Nanocrystalline Materials

The necessary conditions for preparing nanocrystalline materials are:

(i) The magnetic properties are highly dependent on grain size; if the grain size is longer, the magnetic anisotropy would be very high, which in turn will have diverse effect on the soft magnetic properties specially the permeability.

(ii) There should be nucleation centers initiated for the crystallization process to be distributed throughout the bulk of the amorphous matrix.

(iii) There must be a nucleation for stabilizing the crystallites.

(iv) Nanocrystalline materials obtained from crystallization must be controlled so that the crystallites do not grow too big. The grain growth should be controlled so that the grain diameter is within 15-20nm.

(v) The sizes of the grains can be limited to nanometer scale by doping group –II metals etc.

$$\rightarrow Cu\left(Au............\right)$$
$$\rightarrow Nb, W, Mo, Cr, Ta, \text{etc.}$$

(vi) The stability must be lower and the crystallization temperature must be higher.

2.8. Rapid Solidification Processing

Amorphous metallic alloys are synthesized by rapid solidification processing techniques in alloy systems where the liquid phase remains stable to low temperature and

there are competing crystalline phases below the liquidus, i.e. systems with deep eutectics. These are typically metastable phases. Amorphous alloys can be produced by a variety of rapid solidification processing routes including splat quenching, melt spinning, gas atomization and condensation from the gas phase. These typically require cooling rates of greater than 10^4K/sec for binary alloys at a eutectic composition. Among the most common rapid solidification processing technique is melt spinning which yields amorphous metallic ribbons typically 20µm in thickness and gas atomization techniques that yield several µm to submicron powders the smallest of which can be made amorphous.

Massalski [2.18] has discussed the thermodynamic and kinetic considerations for the synthesis of amorphous metallic phases. Glass forming ability (GFA) involves suppressing crystallization by preventing nucleation and growth of the stable crystalline phase so as to maintain a metastable quenched liquid phase. The solidification of eutectic liquid involves partitioning of the constituents so as to form the stable crystalline phase. Glass forming ability can be correlated with the reduced glass-forming temperature, T_{rg}, which is defined as

$$T_{rg} = \frac{(T_L - T_g)}{T_L},$$ where T_L and T_g are the liquidus and glass transition

temperatures, respectively. Five criteria have been enumerated for promoting the partitionless (i.e. with no composition change) freezing of a liquid to form a metallic glass. There are:

(i)   Quenching to below the T_0 curve: The so-called T_0 curve represents the temperature below which there is no thermodynamic driving force for partitioning and the liquid freezes into a solid of the same composition.

(ii)   Morphological stability depends on the comparison of imposed heat flow and the velocity of the interface between the amorphous solid and liquid phase.

(iii)   Heat flow: The super cooling of the liquid phase must exceed $\frac{L}{C}$, where L is the latent heat of solidification and C is the specific heat of the liquid, so as to prevent segregation.

(iv)   Kinetic criteria: A critical cooling rate, R_c, for quenching in the liquid phase is empirically known to depend intimately on the reduced glass forming temperature, T_{rg}.

(v)   Structural: Different atomic size ratios typically with difference exceeding $\approx 13\%$ are desired to retard the diffusional motion necessary for partitioning.

2.9   Rapid Quenching Method

As shown in a schematic diagram in fig-2.3, the rapid quenching technique apparatus consists mainly of a copper roller, an induction heater and a nozzle. A variable speed motor drives the roller via a tooth belt. The angular velocity was 2000 rev/min. Use of log wheel rotation enabled us to vary the surface velocity in the range of 20 to 30m/s. The diameter of the copper roller was 10cm. The use of copper as the roller material was chosen for its conductivity and mechanical softness, which allowed cleaning and polishing to be carried out easily
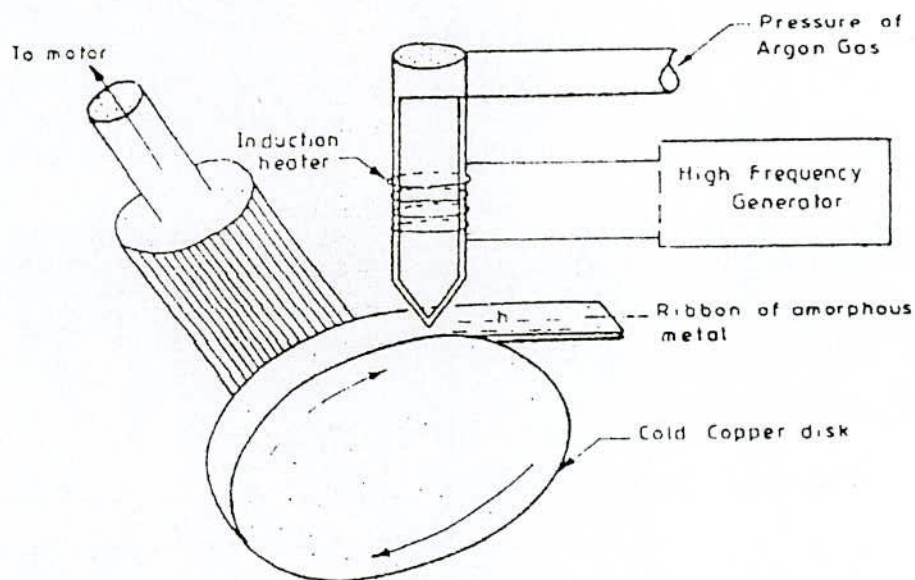
Fig.2.3   Thin layer of molten alloy having intimate contact with the outer surface of metallic rotor is quenched into amorphous ribbon.

In this process one has to consider that variation of the roller should be well below the high frequency vibration of the melt puddle to avoid any influence of it on the geometry and uniformity of the ribbon. One has to be careful and see that the ribbon does not remain in contact with surface of the roller for a whole revolution and be hit, from the

back. A bigger diameter is thus preferred for the roller. The induction heater coil is made of hollow copper tubing, which is cooled simultaneously by circulating water is to be adjusted to produce proper temperature gradient. This is to avoid sudden cooling of the melt in its way out of the crucible and blocking the nozzle. The quartz tubing having outer diameter 20mm which is narrowed down conically to 1mm with a whole fort he nozzle 0.1 t o 0.2mm.

The nozzle geometry is selected to minimize the contraction in the cross-sectional area of the molten jet as it leaves the nozzle orifice. Quartz tube is suitable for repeated use in several successful runs and should be transparent to make the melting process visible. It should withstand the sudden fast changes in temperature.

2.10   Experimental Details of the Preparation of Nanocrystalline Amorphous Ribbons

The component elements of the alloys are weighing 50 gms first melted in an induction furnace and quenched in water to get master alloys. Thus results in a button shaped specimens, the buttons prepared are about 50 grams each. Care is taken to ensure through mixing and homogeneity of the alloy composition, by turning over and re-melting each button few times. The mother alloys which are formed in the form of buttons in a furnace is then cut into small pieces and is introduced in the quartz tube. The quartz tube is connected from the top by rubber "O" rings and metal rings to the argon cylinder through a valve and a pressure gauge. After proper cleaning of the roller surface and adjusting its speed to the desired value, as measured by stroboscope the induction furnace is powered using high frequency generator. When the melting temperature is reached as observed through a protective spectacle, the injection pressure is applied by opening the pressure valve. To avoid the turbulence of the wind, arising from the high speed of the roller in disturbing the melt puddle, cotton pad and metallic shield are usually used just beneath the roller.

To avoid oxidation of the ribbon during its formation an inert atmosphere can be created around the roller by a slow stream of helium or argon gas. The speed of the roller, the volumetric flow rate, the diameter, the substrate orifice distance, the injection angle etc. are adjusted by trial and error method to get the best result in respect of the quality and the geometry of the ribbon.

2.10.1 Important Factors to Control the Thickness of Ribbons

    (i)   Rotating speed

        (a) Angular velocity $\omega = 2000$ rev/min

        (b) Surface velocity $V = 20$ m/s

    (ii)   Gap between nozzle and rotating copper drum $h = 100$ to 150 µm

    (iii)   Oscillations of rotating copper drum both static and dynamic have maximum displacement 1.5 to 5 µm.

    (iv)   Pressure = 0.2 to 0.3 argon atmosphere.

    (v)   Temperature of molten metals $T_m \cong 1500^0$ C; other wise quartz tube would be melted.

    (vi)   A steady flow of the molten metal on the surface of the rotating drum needs to be ensured.

2.11 Confirmation of Amorphousity of Ribbons

The amorphousity of the three ribbons have been conformed by X-ray diffraction using Cu-K$_a$ radiation using Phillips (PW 3040) X Pert PRO XRD system located at Atomic Energy Centre, Dhaka (AECD).
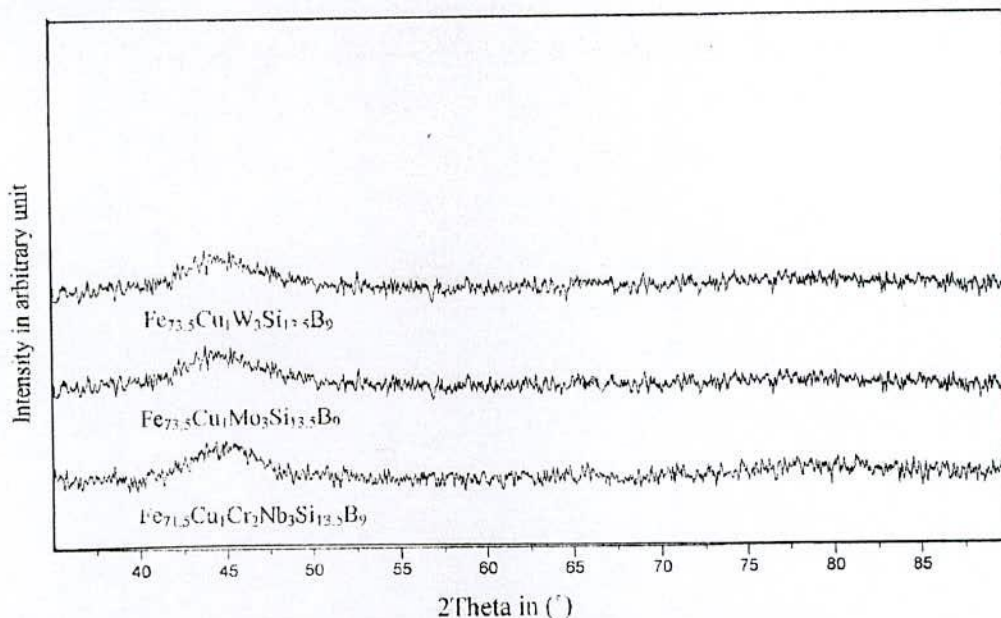
Fig.2.4   X-ray diffraction of as-cast Nanocrystalline amorphous ribbons with composition $Fe_{73.5}$ Cu_1 M_3 $Si_{13.5}$ B_9 [M =Mo & W] and $Fe_{71.5}Cr_2$ Cu_1 Nb_3 $Si_{13.5}$ B_9

From the X-ray diffraction pattern of the samples in fig.2.4, no peaks are observed within the scanning range. Although there are few small humps are shown in diffraction pattern but these can not be regarded due to the crystalline effects. So from the over all pattern of the X-ray diffraction it is confirmed that all the three samples are in pure amorphous state.

Chapter-III

THEORETICAL ASPECTS

3 THEORETICAL ASPECTS

3.1 Stability of Amorphous Nanocrystalline Materials

Amorphous alloys are in a metastable state and tend to transform into stable crystalline phases. There are three kinds of stability of significance for amorphous magnetic ribbons:

i)   Their resistance to the initiation of crystallization.

ii)   Structural relaxation effects and

iii) The relaxation or reorientation of directional order.

Actually, controlled crystallization from the amorphous state seems to be the only method presently available to synthesize nanocrystalline alloys with attractive soft magnetic properties. The amorphous nancrystalline ribbon is prepared by rapid solidification from the melt-a meanwhile well established technique for large scale production of amorphous alloys. Amorphous alloys are in a metastable state and tend to transform into stable crystalline phases. At temperature below the crystallization temperature, structural relaxation effects take place and are caused by atomic rearrangements. The formation and resultant stability of amorphous alloys are important topic both for theoretical understanding and technical application. From the thermodynamic view point [3.1-3.2], the ability of an alloy to be quenched into the glassy state is generally measured by the magnitude of the quantity.

$$\Delta T_g = T_m - T_g \tag{3.1}$$

where T_m and T_g are the melting and glass temperature respectively. In a similar manner the stability of the glass after formation is generally measured by the magnitude of the quantity.

$$\Delta T_x = T_x - T_g \tag{3.2}$$

Where T_x is the temperature for the onset of crystallization. As the temperature decreases from T_m the rate of crystallization will increase rapidly but then fall rapidly as the temperature decreases below T_g. Thus if one quenched a molten alloy rapidly enough to temperature below T_g a quasi-equilibrium amorphous phase is obtained. There is no direct relation between the ease of formation and the resultant stability of an amorphous

alloy. The amorphous alloy composition most favorable for glass formation is near eutectic i.e. the composition in which the transformation from the liquid state to solid state takes place instantaneously without passing through liquid plus solid mixed phase. The deeper the eutectic the better is the glass formation ability [3.3]. At such a point the liquid is particularly stable against crystallization. There have been three approaches for relating the stability of the glass, i.e., its microstructure.

[i] Barnal's model of randomly packed hard sphere's [3.4]. The metal atoms are assumed to from a random network of close packed hard spheres and the smaller metalloid atoms fill the holes inherent in such a structure.

[ii] The effect of atomic sizes and interatomic interactions [3.5], i.e. chemical bonding and suggested that it is chemical bonds which are the dominating factors in glass formation and stability.

[iii] The third approach [3.6] is based on the role of the electron gas and showed that under certain circumstances a nearly free electron gas will produce a barrier against crystallization.

The crystallization is associated with nucleation and growth process. Since the formation of an amorphous alloy depends on the absence of long-range order, change of composition is expected to affect T_g and T_x. This is because the long range ordering of atoms depends on the free energy difference between the crystalline state and the amorphous state. The change of composition affects the growth kinetics in a complicated way, which can only be determined experimentally. The transition to the glassy state and the crystalline state is accompanied by an exothermic heat effect giving rise to a sharp peak in temperature dependence of the heat flow. Therefore, differential thermal analysis (DTA) is a widely used technique to study thermally induced transformations in amorphous alloys and to determine T_g and T_x. The magnitude of T_g and T_x are very different for amorphous materials and depend strongly on composition. The activation energy ranges typically between 2 and 6 eV.

The dependence of T_x on the heating rate $\beta = \dfrac{dT}{dt}$ can be used to determine the activation energy of crystallization [3.7]. Considering the fraction x of amorphous material

transformed into the crystalline state in time t and at temperature T, one obtains for the first- order rate process [3.8-3.9].

$$\left(\frac{\delta x}{\delta t}\right)_T = K(1-x) \tag{3.3}$$

For thermally activated process, the rate constant K obeys an Arrhenius type of equations

$$K = K_o e^{-\left(\frac{\Delta E}{RT}\right)} \tag{3.4}$$

where K_o is a constant and ΔE is the activation energy. Combining eq^n(3.3) and eq^n(3.4)

and using $dx = \left(\frac{\delta x}{\delta t}\right)_T dt + \left(\frac{\delta x}{\delta t}\right)_t dT$ with $\left(\frac{\delta x}{\delta t}\right)dt \cong 0$, one obtains

$$\frac{dx}{dt} = K_o(1-x)e^{-\left(\Delta E/RT\right)} \tag{3.5}$$

$$\frac{d^2x}{dt^2} = \frac{d}{dt}\left[K_0(1-x)e^{-\Delta E/RT}\right]$$

$$= -K_0\frac{dx}{dt}e^{-\Delta E/RT} + K_0(1-x)\frac{d}{dT}\left(e^{-\Delta E/RT}\right)\frac{dT}{dt}$$

$$= -K_0\frac{dx}{dt}e^{-\Delta E/RT} + \frac{dx}{dt}\left(\frac{\Delta E}{RT^2}\right)\beta$$

At the peak of the exothermic heat, the change of the reaction rate $\frac{d^2x}{dt^2} = 0$, yielding

with T=T_x but $\frac{dx}{dt} \neq 0$

$$K_o e^{-\left(\frac{\Delta E}{RT_x}\right)} = \left(\frac{\Delta E}{RT_x^2}\right)\beta \tag{3.6}$$

ΔT_x for the stability of amorphous alloys as given by eq^n(3.2) and is obtained from DTA. The values of ΔE also appear to correlate well with the number of atomic species in the alloy; the more complex the alloy the greater is ΔE. Similar correlation between thermal stability as measured by ΔT_x and ΔE appears to small.

From the measured data of the heating rate (β) and the respective crystallization temperature (T_r), the activation energy can be deduced from the slope of a plot of

$\ln\left(\dfrac{\beta}{T^2_x}\right)$ versus $\dfrac{1}{T_x}$. Eq^n(3.6) can be derived from transformation theory, where ΔE is

the activation energy for versus flow, and other terms have been omitted because they have an insignificant temperature dependence in this region of temperature. The values of ΔE also appear to correlate well with the number of atomic species in the alloy; the more complex the alloy the greater is ΔE.

3.1.1   Characteristics of the Glass Transition Temperature

Glass transition temperature (T_g) occurs when the timescale of molecular rearrangements are too long for equilibrium to be maintained.

i) T_g means the time scale of the experiment matters.

ii)   A high frequency/short time scale experiment allows less long for equilibrium to be established – even for an identical cooling rate.

iii) So NMR (high frequency technique 10^{15}Hz) always measures a higher T_g than DTA (differential thermal analysis, 1Hz).

iv)   In the glass itself, entropy is similar to the crystal, and originals in vibrational modes, which are still present.

v)   Long range transnational motions are frozen out. The temperature T_g Configuration freezes out, relaxation (including transnational motion) but vibrational relaxations are still in equilibrium.

vi) T_g decreases as melt cooled more and more slowly.

vii) When the timescale of the experiment and the configurational relaxation time coincide, begin to see departure from equilibrium.

viii) The timescale for configuration relaxation will be related to rotational or translational diffusion co-efficient.

ix)   Operational definition of T_g is when the viscosity of the super cooled liquid exceeds 10^{13} NSm^{-2}. Where as in the liquid there is an Arrenhius type with a Boltzmann factor containing an activation energy.

3.1.2 Differential Thermal Analysis

Differential thermal analysis (DTA) is an important technique for the study of structural change both in solid and liquid materials under heat treatment. The principle of differential thermal analysis is widely used to understand the crystallization nature of

amorphous. Differential thermal analysis is a direct and effective technique for analyzing the kinetics of amorphous materials and stability with respect to crystallization process. Nanocrystalline amorphous ribbons prepared by rapid quenching method have been subjected to differential thermal analysis (DTA) using a Shimadzu thermal analyzer. Different peaks, crystallization temperatures, crystallization activation energies are obtained from this analysis.

From the DTA curves of different heating rates the crystallization activation energies of different phases can be calculated using heating rate and crystallization peak temperature. For the study of crystallization kinetics the following assumptions were under taken, each crystallization peak can be described by a kinetic equation of the form [3.10]

$$\frac{d\alpha}{dt} = K(T)f(\alpha) \tag{3.7}$$

Where $K(T) = A\exp[-\frac{E}{RT}]$ is the Arrhenius temperature dependent rate constant E is the apparent activation energy, A is the pre-exponential factor and $f(\alpha)$ characterizes is the type of transformation mechanism. The activation energy of crystallization (E) was calculated from non isothermal measurements using the Kissinger method [3.11] which relates the dependence of T_p on heating rate β through the following equation:

$$\ln\frac{\beta}{T_p^2} = -\frac{E}{RT_p} + \ln(\frac{AR}{E}) \tag{3.8}$$

The value of E was obtained from the slop of $\ln\frac{\beta}{T_p^2}$ versus $\frac{1000}{T_p}$ plot and the pre exponential factor A from the intercept.

3.2   Theory of X-ray powder Method

Nanocrystalline alloys are basically crystalline, and because of their crystallinity they exhibit Bragg scattering peaks in X-ray diffraction experiments. However, due to their small size, significant fine particle broadening is observed in the Bragg peaks. The X-ray scattering from a crystalline solid is given by Bragg's Law:

$$2d\sin\theta = n\lambda \tag{3.9}$$

A single crystal with a particular set of atomic planes oriented toward the X-ray beam is different X-ray at an angle θ determined by the Bragg equation.

$$2d\sin\theta = \lambda, \tag{3.10}$$

25

where λ is the wavelength of X-ray, d is distance between the planes. Most materials are not single crystals but are composed of billions of very small crystallite. This type of material is referred to as a powder of polycrystalline aggregate. In these materials, there are a great number of crystalline in all possible orientations. Thus, when a powder is placed in an X-ray beam all possible inter atomic planes will be seen by the beam but diffraction from each different type of plane will only occur at its characteristics diffraction angleθ. Thus, instead of a dot pattern, a powder is series of concentric rings.

The powder diffraction patterns can be recorded on a strip of film surrounding the sample. The camera which carries out this diffraction is called a Debye- Scherred camera. Today most patterns are obtained from powder diffractometer.

Each peak in pattern shown in fig.3.1 corresponds to diffraction from a particular set of inter atomic planes, whose spacing d_{hkl} may be calculated from the Bragg equation. We use X-ray of known wavelength and the value of θ can be measured directly on the diffraction pattern. Further, we can find the index $[hkl]$ of each peak that means to define the inter-atomic plane corresponds to the peak. After index we can define the type of the structure of the crystallographic cell, calculate the crystallographic parameter. The calculation mentioned above depends on the symmetry of the crystal. For the cubic system, the index is following:

We have,

$$\frac{1}{d_{hkl}^2} = \frac{1}{a^2}\left(h^2 + k^2 + l^2\right) \qquad (3.11)$$

and from the Bragg equation,

$$d_{hkl} = \frac{\lambda}{2\sin\theta} \qquad (3.12)$$

So, $\quad \sin^2\theta = \frac{\lambda^2}{4a^2}\left(h^2 + k^2 + l^2\right) \qquad (3.13)$

or, $\sin\theta = \frac{\lambda}{2a}\sqrt{h^2 + k^2 + l^2} \qquad (3.14)$

$$y = Kx$$
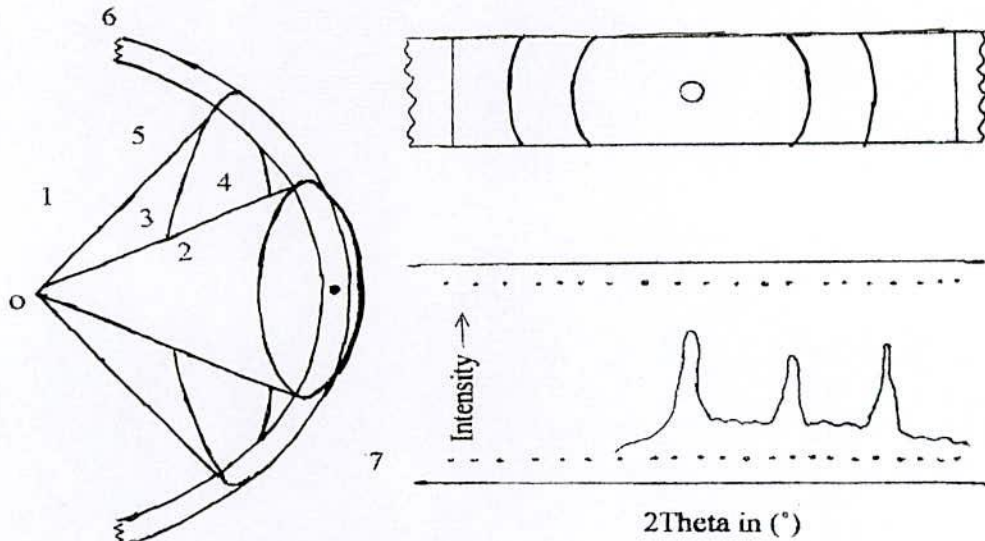
Fig.3.1:   1:   Ewald sphere

2, 3:   Sphere of $\vec{G}$ extremities

4, 5:   Cone of diffraction directions

6:      Diffraction lines on the strip of film around the sample

7:      Diffraction diagram from diffractometer

For every plane (every set of $[hkl]$) $K = \sqrt{h^2 + k^2 + l^2}$ is an integer and is constant. So $y = \sin\theta$ is linear function of $x = \dfrac{\lambda}{2a}$.

We can draw graphics $y = Kx$ with different value of as shown in fig.-3.2.

Every set of the values $\sin\theta$ from the diffraction pattern corresponds to the value $y = \sin\theta$ on the graphic at definite value $x = \dfrac{\lambda}{2a}$. We can find this value if we mark on the strip of paper all values $\sin\theta$ calculated from the diffraction pattern and move the strip parallel to the abscises (fig.3.2) until all the marks coincides with the value $y = \sin\theta$ on the graphics. So we can define $\dfrac{\lambda}{2a}$ and the index h, k, l of every peak is found directly on the graphic.

In comparison with the graphic, may be there are not equivalent marks on the strip of paper, that means these reflections indirect structure factor $([hkl] = 0)$.

So after index, we can define the type of the cell (simple cubic, fcc, bcc, diamond)

27

Because

$$a = d_{hkl}\sqrt{h^2 + k^2 + l^2} = \frac{\lambda}{2\sin\theta}\sqrt{h^2 + k^2 + l^2} \ ,$$ (3.15)

the value λ is given with high accuracy. So,

$$\left|\frac{\Delta a}{a}\right| = \cot\theta \times \Delta\theta \ ,$$ (3.16)

$\cot\theta$ decrease to 0 when θ increase to 90^0. This is the reason why for measuring a, we have to choose some peaks corresponds to the large θ and make an extrapolation to $\theta = 90^0$.
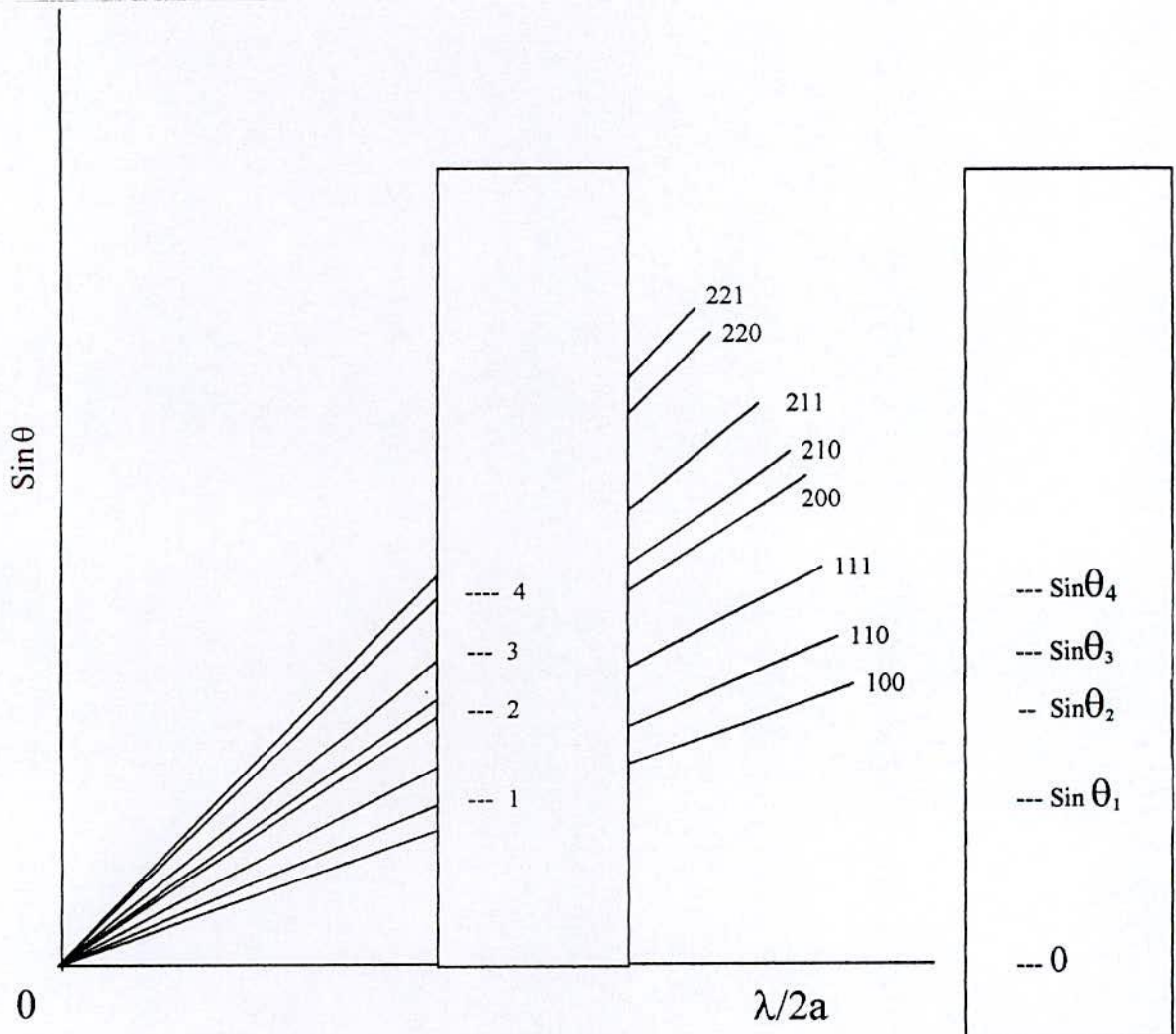
Fig.-3.2   Index diffraction lines (Cube system).

28

3.2.1 Effect of Fine Particle Size

To better understand the phenomenon of fine particle broadening following argument of Cullity[3.12] is outlined below. We consider a finite crystal of thickness, $D_g = md$, where m is an integer, and d is the distance between crystalline planes, i.e., there are m m planes in D_g. Considering Fig.-3.3, if the broadened Bragg peak begins at an angle $2\theta_2$ and ends at $2\theta_1$, the breadth of the peak or full width at half maximum is given as:

$$\beta = \frac{1}{2}(2\theta_1 - 2\theta_2) = \theta_1 - \theta_2 \qquad (3.17)$$

Now consider the path differences for each of the two angles θ_1 and θ_2, for X-rays travelling the full thickness of the crystal. The width β is usually measured in radians, an intensity equal to half the maximum intensity. As a rough measure of β, we can take half the difference between the two extreme angles at which the intensity is zero, which amounts to assuming that the diffraction line triangular in shape.

We now write path difference equations for these two angles, related to the entire thickness of the crystal rather to the distance between adjacent planes.

$$2D_g \sin\theta_1 = (m+1)\lambda \qquad (3.18)$$

$$2D_g \sin\theta_2 = (m-1)\lambda \qquad (3.19)$$

By subtraction we find:

$$D_g(\sin\theta_1 - \sin\theta_2) = \lambda \qquad (3.20)$$

$$D_g \cdot 2\cos\left(\frac{\theta_1 + \theta_2}{2}\right)\sin\left(\frac{\theta_1 - \theta_2}{2}\right) = \lambda \qquad (3.21)$$
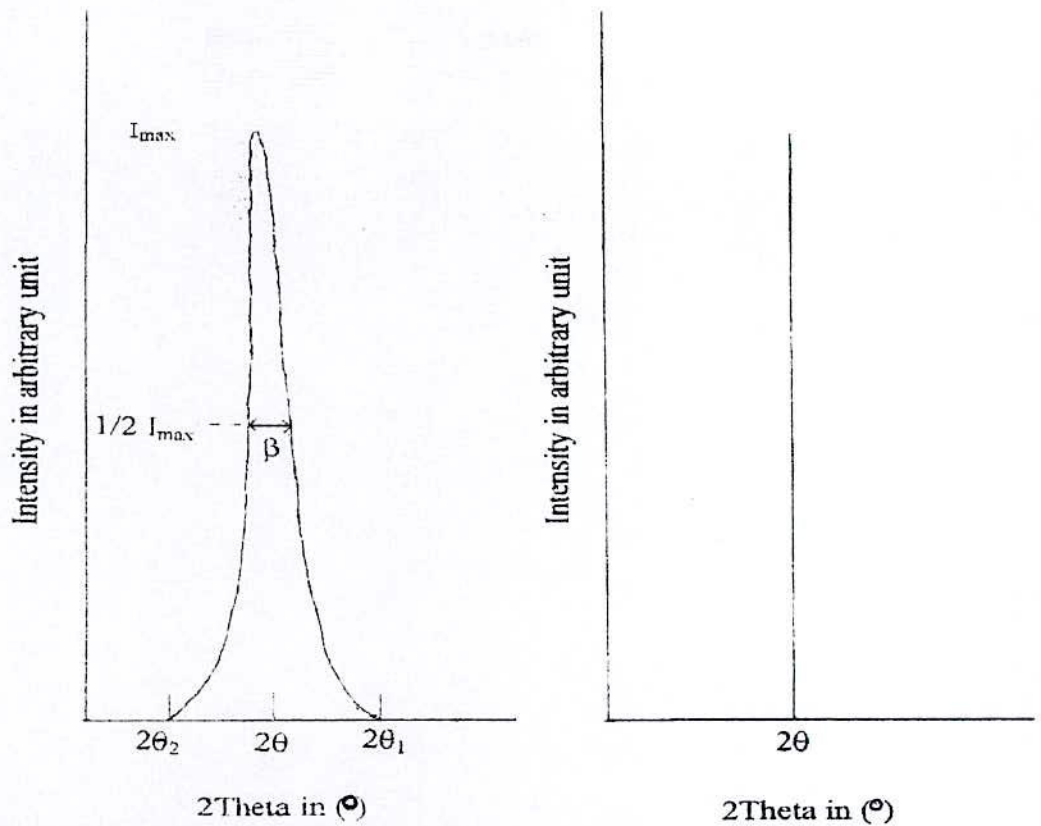
Fig.3.3   Effect of fine particle size on diffraction curves (schematic)

But θ_1 and θ_2 are both very nearly equal to θ, so that $\theta_1 + \theta_2 \approx 2\theta$ and $\sin\left(\dfrac{\theta_1 - \theta_2}{2}\right) \approx \left(\dfrac{\theta_1 - \theta_2}{2}\right)$ so that equation (3.21) can be written as:

$$2D_g \cos\theta \left(\frac{\theta_1 - \theta_2}{2}\right) = \lambda \tag{3.22}$$

From equation (3.17) and equation (3.22) we get:

$$\beta . D_g \cos\theta = \lambda \tag{3.23}$$

$$D_g = \frac{\lambda}{\beta \cos\theta} \tag{3.24}$$

A more exact empirical treatment yields:

$$D_g = \frac{0.9\lambda}{\beta \cos\theta} \tag{3.25}$$

which is known as the Scherrer formula. It is used to estimate the particle size of very small crystals from the measured width of their diffraction curves.

30

3.2.2 Effect of Particle Size on Different Parameters

The smallness of the size of the crystallite causes a broadening of the interference function which obviously means that the corresponding Laue-Bragg Condition will be modified as:

$$a_1.s = h_i + u_i \qquad (3.26)$$

Where h_i's integer and u_i's are fraction less than unity. This signifies that the intensity will not be sharply concentrated at the corresponding Bragg angle θ. In terms of reciprocal lattice, there will be speed of intensity around the reciprocal lattice point h_i corresponding to θ, and the spread which will be dependent on crystalline size is a measure of the smallness of the size provided there is no other defect in the sample under study. Let as now discuss one by one the effect and relationship of particle size with different line broadening parameters as defined earlier.

3.2.2.1 Intensity Factors

Powder diffraction intensity depends on the following factors:

(i)   Structure factor

(ii)   Multiplicity factor

(iii)   Lorentz-polarization factor

(iv)   Absorption factor.

(i)   Structure Factor

Any scattered wave in the complex exponential form is

$$Ae^{i\phi} = fe^{2\pi i(hu+kv+lw)} \qquad (3.27)$$

The resultant wave scattered by all the atoms of the unit cell is called the structure factor, because it describes how the atom arrangement, given by u v w for each atom, affects the scattered beam. The structure factor designated by the symbol F is obtained by simply adding together all the waves scattered by the individual atoms. If a unit cell contains atoms 1, 2, 3,--------, N with fractional co-ordinates [u_1 v_1 w_1], [u_2 v_2 w_2], [u_3 v_3 w_3]---------, and atomic scattering factors f_1, f_2, f_3------, then the structure factor for the [*hkl*] reflection given by

$$F = f_1 e^{2\pi(hu_1+kv_1+lw_1)} + f_2 e^{2\pi(hu_2+kv_2+lw_2)} + f_3 e^{2\pi(hu_3+kv_3+lw_3)} + \ldots\ldots \quad (3.28)$$

This equation may be written more compactly as

$$F_{hkl} = \sum_{n=1}^{N} f_n e^{2\pi i (hu_n + kv_n + lw_n)} \qquad (3.29)$$

where the summation extends over all the N atoms of the unit cell. F is, in general, a complex number, and it expresses both the amplitude and phase of the resultant wave, its absolute value $|F|$ gives the amplitude of the resultant wave in terms of the amplitude of the wave scattered by a single electron.

Like the atomic scattering factor f, $|F|$ is defined as a ratio of amplitudes.

$$|F| = \frac{\text{Amplitude of the wave scattered by all the atoms of a unit cell}}{\text{Amplitude of the wave scattered by one electron}}$$

The intensity of the beam diffracted by all the atoms of the unit cell in a direction predicted by the Bragg law is proportional simply to $|F|^2$, the square of the amplitude of the resultant beam, and $|F|^2$ is obtained by multiplying the expression given for F in equation (3.29). By its complex conjugate equation (3.29) is therefore a very important relation in X-ray crystallography, since it permits a calculation of the intensity of any [hkl] reflection from knowledge of the atomic positions.

(ii) Multiplicity Factor

Relative proportion of planes contributing to the same reflection enters the intensity equation as the quantity multiplicity factor (p), which may be defined as the number of different planes in a form having the same spacing. Parallel planes with different planes in a form having the same spacing. Parallel planes with different Miller indices, such as (100) and (100), are counted separately as different planes, yielding numbers, which are double these given in the preceding paragraph. Thus the multiplicity factor for the {100} planes of a cubic crystal is 6 and for the {111} planes 8. The value of multiplicity factor depends on the crystal: in a tetragonal crystal, the (100) and (001) planes do not have the same spacing, so that the value of multiplicity factor for {100} planes is reduced to 4 and the value for {001} planes to 2. Values of the multiplicity factor as a function [hkl] and crystal system.

32

(iii) Lorentz-Polarization Factor

The Thomson equation for the scattering of an X-ray beam by a single crystal. The intensities two scattered components:

$$I_p = I_0 \frac{k}{r^2} \left(\frac{1 + \cos^2 2\theta}{2} \right) \tag{3.30}$$

The intensity of the structure beam is only a minute fraction of the intensity of the incident beam; the value of $k = 7.94 \times 10^{-30} m^2$ and $\frac{I_p}{I_0} = 7.94 \times 10^{-26}$ in the forward direction at 1cm from the electron. The last factor of equation (3.30) i.e. $\frac{1}{2}(1 + \cos^2 2\theta)$ is called the polarization factor.

The breadth of the diffraction curve varies in the opposite way, being larger at larger values of 2θ, where the half maximum breadth to be proportion to $\frac{1}{\cos\theta}$. The integrated intensity of the reflections is given by the area under the diffraction curve and is proportional to $\left(\frac{1}{\sin\theta} \right)\left(\frac{1}{\cos\theta} \right)$ or $\left(\frac{1}{\sin 2\theta} \right)$. Thus as a crystal is rotated through the Bragg angle, the integrated intensity of a reflection, which is the quantity of most experimental interest turns out to be greater for large and small values of 2θ than for intermediate values, other things being equal. The number of crystals favorably oriented is thus proportional to $\cos\theta$ and is quite for reflections in the backward direction. The relative intensity per unit length of line is proportional to $\left(\frac{1}{\sin 2\theta} \right)$.

In intensity calculations, the three factors just combined into one and called the Lorentz factor.

$$\text{Lorentz factor} = \left(\frac{1}{\sin\theta} \right)\cos\theta\left(\frac{1}{\sin 2\theta} \right)$$

$$= \frac{1}{4\sin^2\theta\cos\theta} \tag{3.31}$$

The combined Lorentz-polarization factor, which, with a constant factor $\frac{1}{8}$ omitted, is given by.

$$\text{Lorentz-Polarization factor} = \frac{1+\cos^2 2\theta}{\sin^2\theta\cos\theta} \qquad (3.32)$$

The over all effect of these geometrical factors is to decrease the intensity of reflection at intermediate angles compared to those in forward or backward directions.

(iv)   Absorption Factor

X-ray is attenuated when passing through matter. This loss of electromagnetic energy is due to two effects, conversion of energy to thermal and scattering X-ray beam of intensity I that changes to I+dl passing thorough a thickness dx of a material. The law which holds good is

$$-\frac{di}{i} = \mu x \qquad (3.33)$$

By integration and putting $I=I_0$ when x=0, we get

$$I = I_0 e^{-\mu x}, \qquad (3.34)$$

An expression called Bear's law. The factor μ has the dimension of a reciprocal length and depends on the state of the material. It is called the linear absorption coefficient.

In addition to the linear absorption coefficient, two further types of absorption coefficients are used. The first, denoted by μ_m, is the ratio μ and the density d, and called the mass absorption coefficient

$$\mu_m = \frac{\mu}{d} \qquad (3.35)$$

Unlike linear absorption coefficient, mass absorption coefficient is independent of the physical and chemical state of the material. Hence the mass absorption coefficient of a substance consisting of several elements can be calculated by simple addition of the mass absorption coefficients of the individual elements with proper weightings. The 2nd is called the atomic absorption coefficient, which is defined for a material for a material of single element as:

$$-\frac{dI}{I} = \mu_a dx, \qquad (3.36)$$

where dx is the number of atoms in the path of the beam per unit area and μ_a is the atomic absorption coefficient. The value of μ_a depends on the element. For a given element, μ_a

(and also $\frac{\mu}{d}$), depends on wavelength. Sharp discontinuities occur at particular value of λ. These discontinuities are called absorption edges, found one in the K-series, and when an X-ray quanta has energy less than the energy to remove 'an electron, their in the L-series. They can be understood in terms of electronic structure of the atoms. When an X-ray quanta has energy less than the energy to remove an electron, their photo-electrical absorption is possible and the quanta interact with the whole atom increasing in energy which is equivalent to increasing its temperature. If the critical energy is E_k and absorption edge attains the corresponding magnitude, $\lambda_k = \frac{hc}{E_k}$ the electron in K-shell is ejected.

Therefore μ_a increase discontinuously and λ_k. Between the absorption edges, μ_a is given by

$$\mu_a = eZ^4\lambda^{\frac{5}{2}} \quad , \tag{3.37}$$

where Z is the atomic number of the material and e is a constant. The value of e depends on the nature of two flanking absorption edges.

(v)   Temperature Factor

A crystal is a collection of atoms located at fixed points in the lattice. Actually the atoms undergo thermal vibration about their mean positions even at the absolute zero of temperature, and the amplitude of this vibration increases as the temperature increases. In aluminum at room temperature, the average displacement of an atom from its mean position is about 0.17A°, which is by no means negligible, being about 6 percent of the distance of closest approach of the mean atom positions in this crystal. Increased thermal vibration of the atoms, as the result of an increase in temperature, has three main effects:

(i)   The unit cell expands, causing changes in plane spacing d and therefore in the 2θ positions of the diffraction lines. If the positions of one or more lines are measured as a function of temperature the thermal expansion coefficient of the specimen can be determined by X-ray diffraction.

(ii)   The intensities of the diffraction lines decrease.

(iii)   The intensity of the background scattering between lines increases.

35

Here we are usually interested not in intensity changes with temperature, but in variations in intensity with 2θ of constant temperature (usally room temperature).

3.3 Initial Permeability of Nanocrystalline Alloys

Low effective magnetocrystalline anisotropy and low or vanishing magnetostriction are the key to superior soft magnetic properties. The nanocrystalline alloys offer the highest saturation induction, B_s and simultaneously, the highest level of permeability (μ'). Typical commercial grades by now available under the trade names FINEMET [3.13] and VITROPERM [3.14] are of the compositions $Fe_{70-74}Cu_1Nb_3Si_{13-16}B_{6-9}$ and offer a saturation induction of typically B_s = 1.2-1.3 T and initial permeability $\mu_i \approx$ 150×10^3. Highest permeabilities are required for magnetic cores in ground fault interrupters of common mode chokes.

The complex magnetic properties of initial permeability (μ_i) may be strongly affected by the presence of an electric current, particularly in ac condition. Moreover, the effects are rather different in as quenched amorphous nanocrystalline ribbons. The measurement of magnetic properties as a function of frequency and its analysis by means of the complex permeability formalism has recently led to the resolution of several aspects of magnetizations process [3.15 -3.16] The measurement of complex permeability gives as valuable information about the nature of the domain wall and their movements. Low losses, good high frequency properties are requirements fulfilled by the nancrystalline alloy. In dynamic measurement the eddy current loss is very important which occurs due to irreversible domain wall movements that are frequency dependent. The only draw-back of the nanocrystalline material seems to be the severe embrittlerment upon crystallization which requires limited final shape after annealing and restricts their application mainly to toroidally wound cores. The present goal of most of the recent nanocrystalline amorphous ribbons researches is to fulfill this requirement. Before going into the complexity of initial permeability measurement, we discuss in short the theories and mechanism involved in frequency spectrum of initial permeability and also how they are affected by annealing.

3.3.1 Theories of Permeability

The primary requirement is the highest possible permeability, together with low losses in the frequency range of interest. The initial permeability μ_i is defined as the derivative of induction **B** with respect to the initial field **H** in the demagnetization state.

$$\mu_i = \frac{dB}{dH}, H \rightarrow 0, B \rightarrow 0 \qquad (3.38)$$

At microwave frequency, and also in low anisotropic amorphous materials, dB and dH may be in different directions, the permeability thus a tensor character. In the case of amorphous materials containing a large number of randomly oriented magnetic atoms the permeability will be scalar. As we have

$$B = \mu_0 (H + M) \qquad (3.39)$$

and susceptibility,

$$\chi = \frac{dM}{dH} = \frac{d}{dH}\left(\frac{B}{\mu_0} - H\right) = \frac{1}{\mu_0}(\mu - 1) \qquad (3.40)$$

The magnetic energy density

$$E = \frac{1}{\mu_0}\int H.dB \qquad (3.41)$$

For time harmonic fields $H = H \sin\omega t$, the dissipation can be described by a phase difference δ between **H** and **B**. In the case of permeability, defined as the proportional constant between the magnetic field induction **B** and applied intensity **H**;

$$B = \mu H \qquad (3.42)$$

This naive definition needs further sophistication. If a magnetic material is subjected to an ac magnetic field as we get,

$$B = B_0 e^{i\omega t} \qquad (3.43)$$

Then it is observed that the magnetic flux density B experiences a delay. This is caused due to the presence of various losses and is thus expressed as,

$$B = B_0 e^{i(\omega t - \delta)}, \qquad (3.44)$$

where δ is the phase angle and marks the delay of B with respect to H, the permeability is then given by

$$\mu = \frac{B}{H} = \frac{B_0 e^{i(\omega t - \delta)}}{H_0 e^{i\omega t}}$$

$$= \frac{B_0 e^{-i\delta}}{H_0}$$

$$= \frac{B_0}{H_0}\cos\delta - i\frac{B_0}{H_0}\sin\delta$$

$$\mu = \mu' - i\mu'' \quad , \tag{3.45}$$

$$\text{where } \mu' = \frac{B_0}{H_0}\cos\delta \tag{3.46}$$

$$\text{and } \mu'' = \frac{B_0}{H_0}\sin\delta \tag{3.47}$$

The real part μ' of complex permeability μ as expressed in equation (3.45) represents the component of B which is in phase with H, so it corresponds to the normal permeability. If there are no losses, we should have $\mu = \mu'$. The imaginary part μ'' corresponds to that part of B, which is delayed by phase δ from H. The presence of such a component requires a supply of energy to maintain the alternation magnetization, regardless of the origin of delay. It is useful to introduce the loss factor or loss tangent $(\tan\delta)$. The ratio of μ'' to μ', as is evident from equation gives.

$$\frac{\mu''}{\mu'} = \frac{\dfrac{B_0}{H_0}\sin\delta}{\dfrac{B_0}{H_0}\cos\delta} = \tan\delta \tag{3.48}$$

This $\tan\delta$ is called the loss factor. The Q-factor or quality factor is defined as the reciprocal of this loss factor i.e.

$$Q = \frac{1}{\tan\delta} \tag{3.49}$$

And the relative quality factor $= \dfrac{\mu'}{\tan\delta}$. The behavior of μ' and μ'' versus frequency is called the permeability spectrum. The initial permeability of a ferromagnetic substance is the combined effect of the wall permeability and rotational permeability mechanism.

3.3.2 High Frequency Behavior and Losses

The frequency dependence of the absolute value of complex permeability and its imaginary part μ'' are expressed in terms of the relative loss factor $\dfrac{\mu''}{|\mu|^2}$. The later is directly related to the cycle losses at constant induction amplitude B by

$$\frac{P}{f} = \frac{\pi B^2 \mu''}{\mu_0 |\mu|^2}$$

(3.50)

The frequency dependence of permeability and the core losses of the nanocrystalline Fe-Cu-Nb-Si-B alloys are comparable to those of amorphous Co-based alloys and by pass the properties of conventional materials, even that of ferrites, over the whole frequency range up to several 100 kHz.

The favorable high frequency behavior is essentially related to (1) the thin ribbon gauge of $d \approx 20 \mu m$ inherent to the production technique (ii) to a relatively high electrical resistively of typically $\rho \approx 115 \mu \Omega - cm$ related to the high Si content in the bcc grains [3.17] and the intergranular amorphous phase. Both parameters are comparable to amorphous metals and yield low eddy current losses P_e, which in thin sheets at a frequency f and a induction level B are given per volume by [3.18].

$$P_e = \frac{3\sinh x - \sin x}{x\cosh x - \cos x} \frac{(\pi df B)^2}{6\rho}$$

$$P_e \big|_{x \angle\angle 1} \approx \frac{(\pi df B)^2}{6\rho}$$

(3.51)

with

$$x = 2\sqrt{\frac{f}{f_w}}$$

where

$$f_w = \frac{4\rho}{\pi \mu_0 \mu_i d^2},$$

(3.52)

is the limiting frequency above which the exciting magnetic field no longer fully penetrates the specimen and, accordingly, the permeability decreases as a function of the frequency.

39

Chapter-IV

EXPERIMENTAL DETAILS

4.1 The Differential Thermal Analysis

4.1.1 Introduction

The differential thermal analysis (DTA) is an important technique for studying the structural change occurring both in solid and liquid materials under heat treatment. These changes may be due to dehydration, transition, from one crystalline variety to another, destruction of crystalline lattice, oxidation, decomposition etc. The principle of DTA consists of measuring the heat changes associated with the physical or chemical substance is gradually heated. This technique can also be used to identify magnetic ordering of amorphous ribbons. In order to discuss the possible applications of DTA in amorphous nanocrystalline materials, let us briefly define the various temperature, that are useful in characterizing amorphous nanocrystalline alloys.

This technique has been used in determining the first crystallization temperature $\left(T_{x_1}\right)$ and second crystallization temperature $\left(T_{x_2}\right)$ of our nanocrystalline soft magnetic material. The first crystallization temperature is defined as the temperature at which the alloy passes from the solid to liquid state. For our purposes it is sufficient to describe T_{x_1} as the temperature at which atomic mobility is great enough to allow diffusive atomic rearrangement to occur in a matter of minutes. The crystallization temperature T_{x_2} defined as the temperature at which crystallization occurs with long range ordering and is usually determined by DTA technique by heating rate of $\approx 20^0$C/min. Metallic nanocrystalline glass ribbons usually are ductile in the as-quenched condition, but may often be embrittled by exposure to elevated temperature. DTA measurements on as-cast ribbons where performed with increasing rates of 10^0C/min to 50^0C/min in argon atmosphere. Based on the Kissinger plots, we have evaluated the crystallization activation energy of T_{x_1} and T_{x_2} phases. The DTA technique has been used in determining T_{x_1} and T_{x_2} of our nanocrystalline amorphous ribbon with compositions are $Fe_{73.5}Cu_1W_3Si_{13.5}B_9$, $Fe_{73.5}Cu_1Mo_3Si_{13.5}B_9$ and $Fe_{71.5}Cr_2Cu_1Nb_3Si_{13.5}B_9$.

4.1.2 The Principle of Differential Thermal Analysis

The DTA technique was first suggest by Le Chatelier [4.1] in 1887 and was applied to the study of clays and ceramics. DTA is the process of accurately measuring the difference in the temperature between a thermocouple embedded in a sample and a thermocouple in a standard inert material such aluminum oxide, while both are being heated at the uniform rate. These differences of temperature arise due to the phase transitions or chemical reactions in the sample involving the evolution of heat or absorption of heat due to exothermic reaction or endothermic reaction measured.. The exothermic and endothermic reactions are generally shown in the DTA trace as positive and negative deviations respectively from a base line. So DTA gives a continuous thermal record of reactions occurring in a sample.
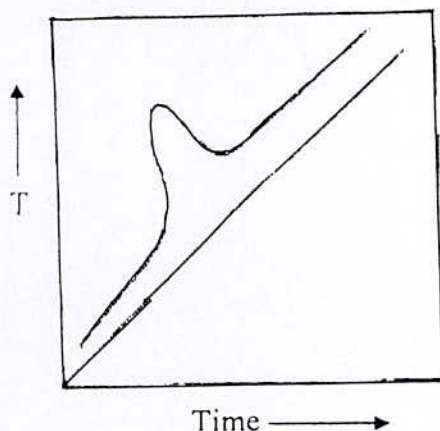
Fig. 4.1(a) Heating curve of sample and reference substance

When a sample and reference substance are heated or cooled at a constant rate under identical environment, their temperature differences are measured as a function of time or temperature as shown by the curve in Fig.4.1 (a). The temperature of the reference substance, which is thermally inactive, rises uniformly when heated, while the temperature of the sample under study changes anomalously when there is physical or a chemical change of the active specimen at a particular temperature. When there is an exothermic reaction there is a peak in the temperature versus time curve, heat supplied from outside is consumed by the reaction. And when the reaction is over, the sample temperature gradually catch up the temperature of the inactive specimen. The temperature difference ΔT is detected, amplified and recorded by a peak as shown in Fig. 4.1(b).

41

ΔT
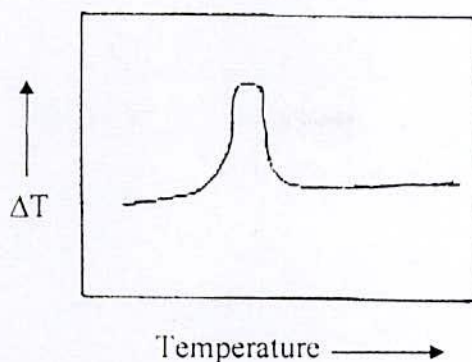
Temperature ⟶

Fig. 4.2(b) DTA Curve

For any endothermic reaction or change the active specimen absorbs heat which is reflected in the corresponding the trough in temperature versus time curve. The temperature in the sample holder is measured by a thermocouple, the signal of which is compensated for the ambient temperature and fed to the temperature controller. This signal is compared with the program signal and the voltage impressed to the furnace is adjusted. Thus the sample and reference substance are heated or cooled at a desired rate. The temperature in the sample holder is digitally displayed on the DTA measurements model TG/DTA 6300 (Differential Thermal Analyzer, Shimadzu Corporation, Kyoto, Japan) and is also recorded on the recorder.

4.1.3 Apparatus

The apparatus for the differential thermal analysis consists of a thin walled refractory specimen holder made of sintered alumina with two adjacent cubical compartments of exactly the same size, 1cm in length shown in fig.-4.2. Of these one is for the reference inert material and the order for the test material, the compartments being separated by a 1mm wall. The specimen holder is placed in the cavity of the heating block which is operated in the center of the cylindrical refractory tube of an electrical furnace. This supplies a uniform heating rate. The furnace $(9'' \times 6'' \times 9'' deep)$ is peaked with calcined china clay. The input of current in to the furnace is secured through the secondary of a Varian transformer, which controls the current. Fine chromelallumel wires $(28 gauge)$ are used for thermocouple.

A cold junction is used for thermocouple leads and the e. m. f. is recorded almost continuously, while the temperature of the inert material is measured at 3minute intervals.

It is essential to use perfectly dry materials, as otherwise errors will be introduced in the analysis. Approximately 0.1gm anhydrous alumina is used in the reference cup and the sample weight varies over a range 0.05 to 0.125gm; depending on their peaked density. A heating rate of 10^0C per minute of the furnace is conveniently kept, and this gives satisfactory results in most cases. A block diagram of DTA is shown in fig.- 4.3.
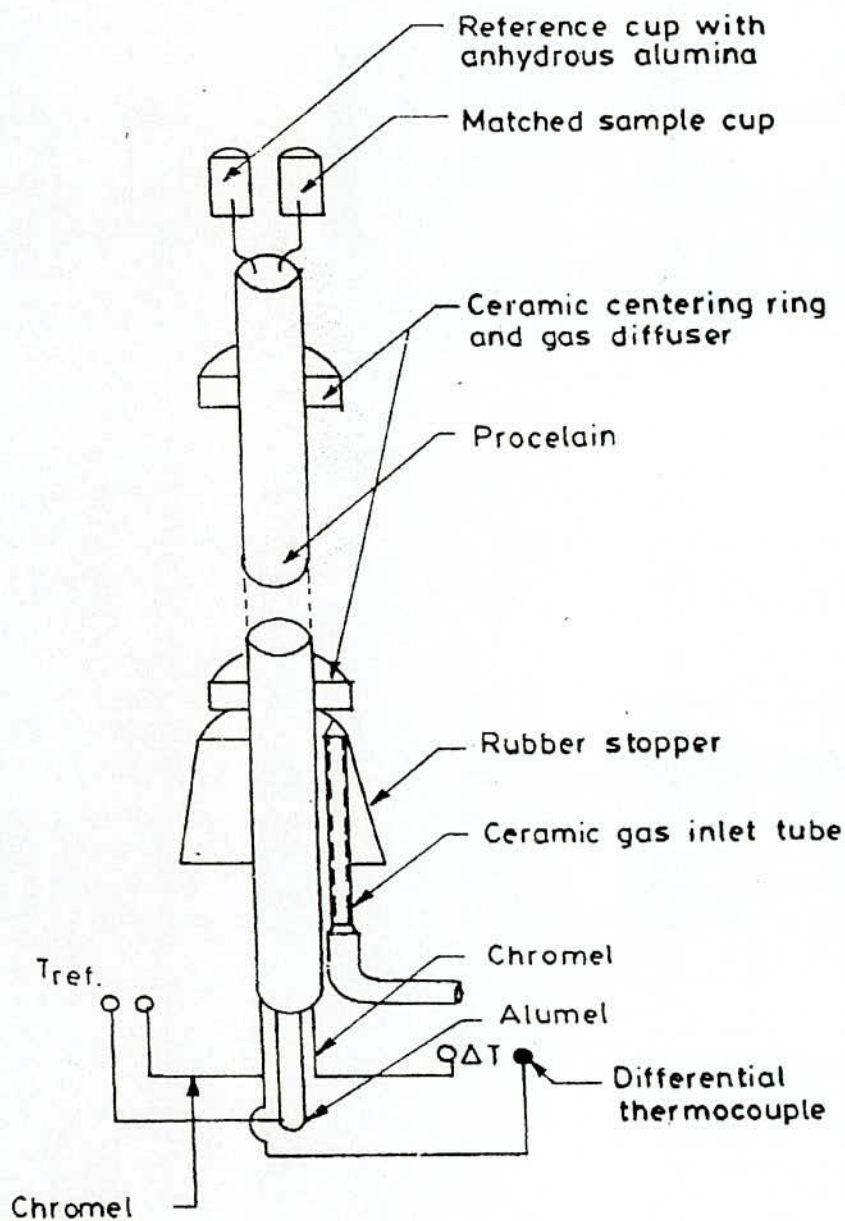
Fig. 4.2   DTA Thermocouple assembly

The thermal analysis runs generally for 1 to 1.5hrs. Thermal analysis curves are obtained by plotting heating temperature and the difference between the temperature of the test and reference substances. From these plots the reaction temperature could be determined. Under standard conditions of the experiment; characteristic curves for different compositions of $Fe_{73.5}Cu_1W_3Si_{13.5}B_9$, $Fe_{73.5}Cu_1Mo_3Si_{13.5}B_9$ and $Fe_{71.5}Cr_2Cu_1Nb_3Si_{13.5}B_9$ nanocrystalline amorphous ribbons. T_{x_1} and T_{x_2} points are indicated, by sharp exothermic peaks.
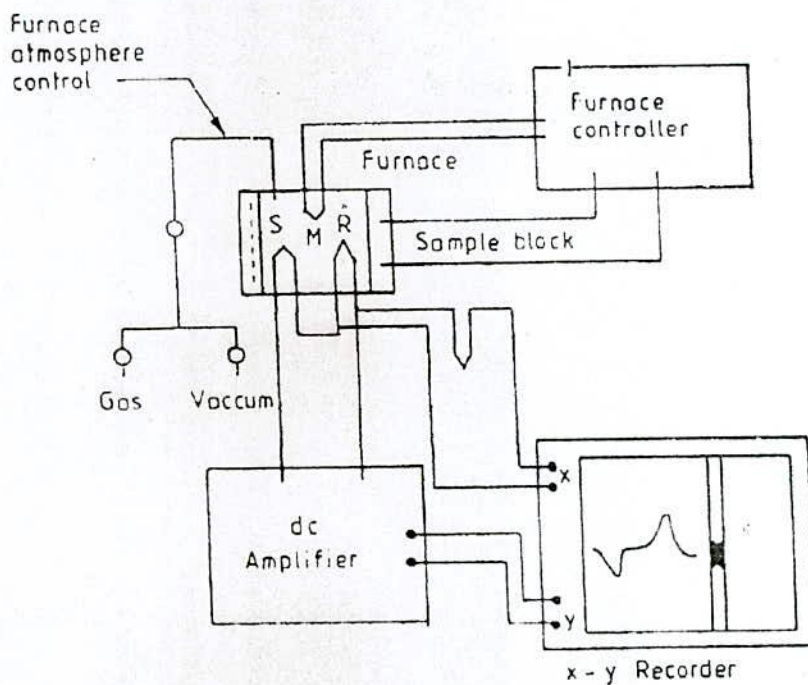
Fig. 4.3   Block diagram of a differential thermal analysis equipment, (S) sample thermocouple, (R) reference thermocouple, (M) monitor thermocouple.

All experiments are run at atmospheric pressure in continuous flow of a purified inert gas argon. Gausses are normally purged into the furnace chamber at the lower end through a purification train in which oxygen and water are removed by heated copper wool and exhausted from the top into a condensate trap for collecting the condensable volatile products.

4.2   Experimental Technique for X-ray Diffraction

X-ray diffraction (XRD) is a versatile non-destructive analytical technique for identification and quantitative determination of various crystalline phases of powdered or

solid samples of any compound. A PHILIPS X pert PRO X-ray diffraction system was used to get X-ray data for the samples at the Material Science Division, Atomic Energy Centre, Dhaka, which is a sophisticated X-ray diffractometer installed very recently, shown in Fig. 4.4 and Fig. 4.5. The powder diffraction technique was used with a primary beam power of 40 kV and 30mA for Cu radiation. A nickel filter was used to reduce Cu-K_β radiation and finally Cu-K_α radiation was only used as the primary beam. A (θ-2θ) scan was taken from 20° to 120° to get all possible fundamental peaks of the sample with the sampling pitch of 0.02° and time for each step data collection was 1.0 sec. Both the programmable divergence and receiving slits were used to control the irradiated beam area and output intensity from the sample, respectively. An anti scatter slit was used just after the sample holder to reduce air scattering. Two solar slitts were used just after the tube and in front of the detector to get parallel beam only. All the data of the samples were stored in the computer memory and later analyzed them using computer software "X PERT HIGHSCORE".

For each set of composition, ribbons are cut into several pieces, each of length 20 mm. Heat treatment was performed on the amorphous ribbons using a Naber muffle furnace, where each piece of ribbon was wrapped by aluminum foil separately. After heat treatment, samples were removed from the aluminum foil carefully and kept separately for XRD experiment. For XRD experiment each sample was set on a glass slide and fixed the sample by putting adhesive tape at the two ends of the sample.

4.2.1 Interpretation of the XRD Data

The XRD data consisting of θ_{hkl} and d_{hkl} values corresponding to the different planes from which the following structural information of the nanocrystalline ribbon sample was evaluatrd.

(i)   Identification of phases

(ii)   Lattice parameter determination

(iii) Average grain size determination

(iv)   Si- content determination in nanograins
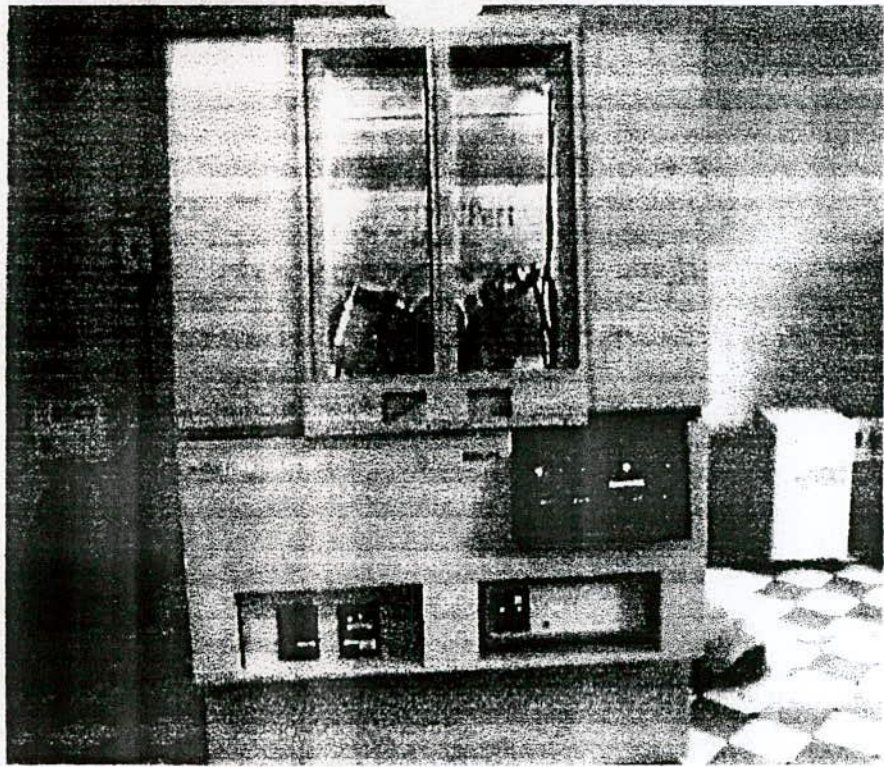
Fig. 4.4   Philips (PW 3040) X Pert PRO XRD system
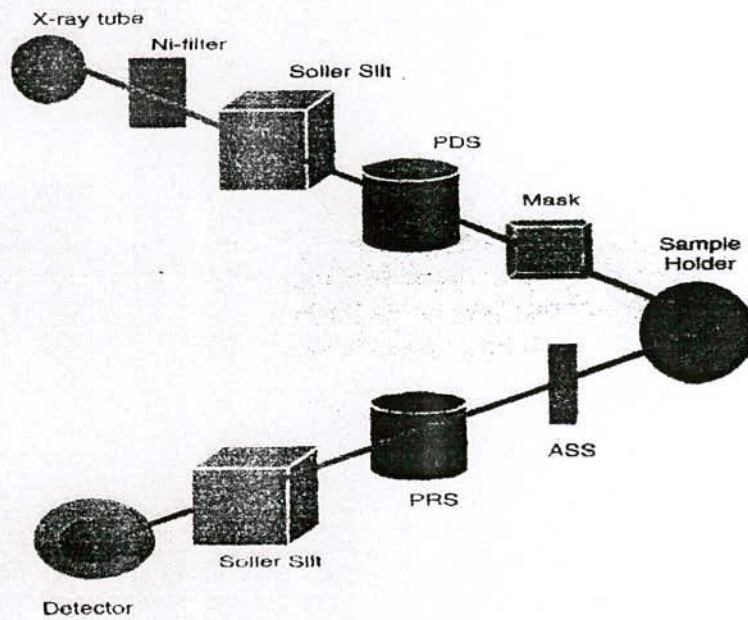
Fig. 4.5   Block diagrams of Philips (PW 3040) X Pert PRO XRD system

(i)   Identification of Phases

X-ray diffractometer has become a very popular and useful instrument for routine X-ray analysis of ribbon samples. In fact the diffractometry technique is often preferred to Debye-Scherrer technique owing to its several inherent merits. The most striking difference between the two methods is in the use of different intensity detection and measuring devices. XRD pattern of as-cast indicates just amorphous pattern of said composition. The XRD patterns of the well annealed samples were analized using serch and match software and were identified as bcc α-Fe-Si solid solution, which were developed on the amorphous ribbon after heat treatment. The peak pattern was observed for all the samples at different heat treatment temperatures indicating the bcc α-Fe-Si phase, which was developed on amorphous ribbons after heat treatment. Present experiment revels that 450°C is not sufficient temperature to start forming of crystalline nanograins of bcc Fe-Si on the amorphous ribbon of the studied alloy compositions.

(ii)   Lattice Parameter Determination

Lattice parameter of crystalline bcc Fe –Si nanograins was determined for all the two different amorphous compositions at different heat treatment temperatures. Normally, lattice parameter of an alloy composition is determined by the Debye-Scherrer method after extrapolation of the curve. In this method, at least five fundamental reflections are required to determine lattice parameter. In the present case, only one reflection (110) is prominent in all XRD patterns and we would like to understand how the value of lattice parameter changes with annealing temperature. We have, therefore, determined the lattice parameter using only that particular reflection using equation $2d\sin\theta = \lambda$ and $a_0 = d\sqrt{2}$, where $\lambda = 1.54178A^0$ for $Cu - K_\alpha$ radiation and a_0 is determined lattice parameter with in an error estimated to be $\pm 0.0005A^0$.

(iii)   Grain Size Determination

The main aim of the present study was to determine the nanocrystalline grain size for all the heat treatment samples of the alloy composition, which was determined using Scherrer method. The XRD pattern of (110) reflection for different steps of heat treatment temperature of the alloy composition was used to calculate grain size. Grain size was determined using the formula,

$$D_g = \frac{0.9\lambda}{\beta\cos\theta},\qquad\qquad(4.1)$$

where $\lambda = 1.54178 A^0$ for $Cu - K_\alpha$ radiation and $\beta = FWHM$ (full width at half maximum) of the peak in radian. Considering β in degree we get the relation,

$$D_g = \frac{79.5}{\beta\cos\theta}\qquad\qquad(4.2)$$

All the values of grain size for every steps of heat treatment temperature of the alloy composition were determined. The FWHM of the peak is large at the early heat treatment temperature and with the increase of heat treatment temperature the value of FWHM becomes smaller.

(iv) Si-Content in Nanograins

Crystalline nanograins were formed on the ribbon in the process of heat treatment having the composition of Fe-Si. It is, therefore important to determine the concentration of Fe and Si in the nanograin. As because the alloy consists of Fe and Si and we have experimentally determined the lattice parameter of the alloy nanograin for the two compositions at different temperatures. It is easy to calculate the Si content in the nanograins from the data of Pearsons who was established the relationship between the lattice parameter as dependent on Si content in Fe-Si alloys covering a wide range of composition [4.2]. From the relationship, we have constructed a simple equation to calculate Si content from lattice parameter. The equation is

$$X = \frac{(a_0 - 2.8812)}{0.0022}\qquad\qquad(4.3)$$

where X is at.% Si in the nanograins, a_0 is the determined lattice parameter of nanograins. Si contents for the nanograins develop during the isothermal annealing at various temperatures have been calculated.

4.3   Experimental Study of Complex Permeability

4.3.1 Determination of Real and Imaginary Components of Complex Permeability

Determinations of permeability normally involve the measurements of the change in self-inductance of a coil in the presence of magnetic core. Methods of measurement commonly used are:

    (i)   The LCR bridge method

    (ii)   Resonance circuits and

    (iii)   The standing wave method

The behavior of a self-inductance can now be described as follows. If we have an ideal lossless air coil of inductance L_0, on insertion of magnetic core with permeability μ, the inductance became μL_0. The complex impendence Z of this coil can then be expressed as

$$Z = R + iX = i\omega L_0 \mu \qquad (4.4)$$

$$= i\omega L_0 (\mu' - i\mu''),$$

$$= \omega L_0 \mu'' + i\omega L_0 \mu'$$

where the resistive part

$$R = \omega L_0 \mu'' \qquad (4.5)$$

and the reactive part is

$$X = \omega L_0 \mu' \qquad (4.6)$$

The r.f permeability can be from the complex impendence of a coil in eq^n (4.4). The core is taken in the toroidal form to avoid demagnetizing effects. The quantity L_0 is described geometrically as shown in section 4.3.3.

4.3.2 Preparation of the Samples for Complex Permeability Measurement

The amorphous ribbons were wound into toroidal having outer and inner diameters 13 to 15 mm and with the ratio of outer and inner diameters always kept less than 1.2 in order to improve the homogeneity of the applied field, as also to reduce the

possibility of an inhomogeneous inductance response. Toroids were wound with 10 turns around to apply ac magnetic fields over a wide range of amplitudes. While measuring the permeability of the amorphous ribbon cores at high frequency, the high electric resistance of these materials generally precludes the trouble some skin effect found in ribbons. However, the cross-section of the amorphous ribbon core to be measured may have to be kept small in order to avoid dimensional resonance phenomena. To avoid an increase in resistance owing to skin effect, braided copper wire is used at frequencies higher than 100 kHz.

At higher frequencies the capacitance arising from winding gives inaccurate values of R and L_s. It is, therefore, necessary to keep the capacitance of the winding as low as possible. Frequency response characteristics were then investigated on these ring shaped specimens as a function of frequency.

4.3.3 Frequency Characteristics of Nanocrystalline Materials

The frequency characteristics of the amorphous of the amorphous ribbons samples i.e the permeability spectra, were investigated using an impedance analyzer (LCR) bridge), Wayne Kerr 3255B model, Atomic Energy Centre, Dhaka. The measurements of inductances were taken in the frequency range 1 kHz to 500 kHz. The values of measured parameters of obtained as a function of frequency and the real and imaginary parts of permeability and the loss factor μ' is calculated by using the following formula.

$$L_s = L_0\mu'$$

$$\mu' = \frac{L_S}{L_0}.$$
(4.7)

$$\tan\delta = \frac{\mu''}{\mu'}$$

and

$$\mu'' = \mu'\tan\delta$$
(4.8)

where L_s is the self-inductance of the sample core and

$$L_0 = \frac{\mu_0 N^2 S}{\bar{d}},$$
(4.9)

50

where L_0 is the inductance of the winding coil without the sample core, N is the number of turns of coil and S is the area of cross section as given below

$$S = dh,$$ (4.10)

where $d = \dfrac{d_2 - d_1}{2}$ and h = height

and $\bar{d}$ is the mean diameter of the sample given as follows:

$$\bar{d} = \dfrac{d_1 + d_2}{2}$$ (4.12)

The relative quality factor is determined for the ratio $\dfrac{\mu'}{\tan \delta}$.

4.4 Curie Temperature Determination from Temperature Dependence of A. C. Permeability

The Curie temperature which is the measure of exchange interaction between the magnetic atoms is quite complicated in the case of nanocrystalline amorphous alloys and is very much an experimental parameter. Because, theories are helpful only as a guide in rationalizing the results obtained experimentally. So, the determination of Curie temperature (T_c) accurately is of great importance.

Our experimental set up for T_c measurement is shown in fig.-4.6. We made use of the excellent experimental facilities available at Material Science Division, AECD. The temperature dependence of A. C. permeability was measured by using induction method. A laboratory built technique using an oven in which a heating wire is wound bifillery i.e. two identical induction coils are wound in opposite directions such that the current induced fluxes in the two coils cancel each other. The sample is put inside the furnace for measurement. By varying temperature, A.C. permeability of the nanocrystalline amorphous ribbon samples of toroidal shapes as a function of temperature was measured. When the magnetic state inside the amorphous sample changes from ferromagnetic to paramagnetic, the permeability falls sharply. From the sharp fall at specific temperature the T_c is determined. This is the basic principle used in our experimental set up.
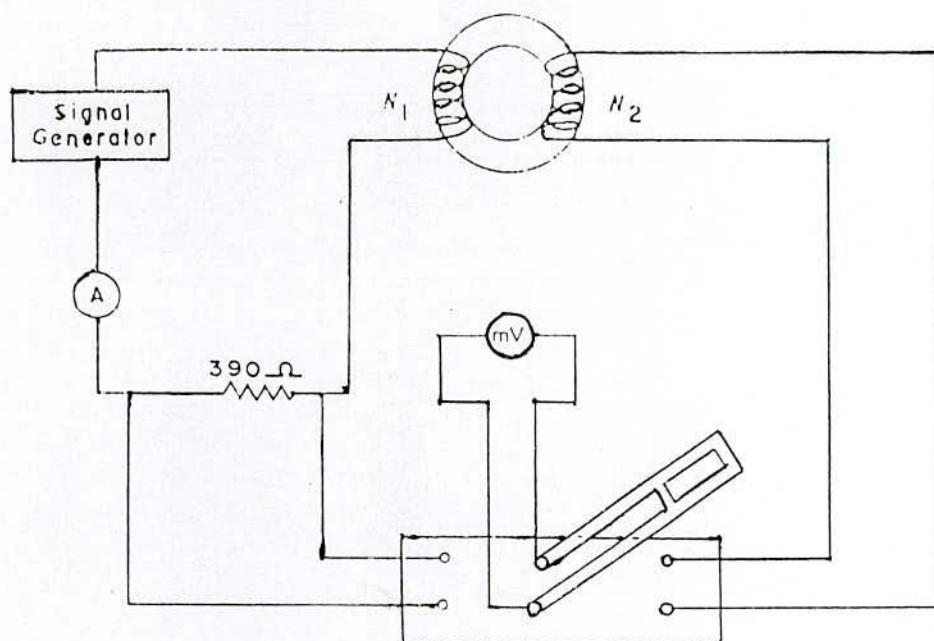
Fig.-4.6 Schematic diagram for the experimental set up for determination of Curie temperature

The thermocouple used in this system measures the temperature inside the oven and also the sample. The sample is kept just in the middle part of the cylindrical oven so that gradient is minimized. The temperature of the oven is raised slowly. If the heating rate is very fast then temperature of the sample may not follow the temperature inside the oven and there can be misleading information on the temperature of sample. The thermocouple showing the temperature in that case will be erroneous. Due to the closed winding wires the sample may not receive the heat at once. So, a slow heating rate is used to eliminate this problem. Also heating adjustment of nanocrystalline amorphous sample ensures accuracy in the determination of T_C. The oven was kept thermally insulated from the surroundings.

Chapter-V

RESULTS AND DISCUSSIONS

5.   EXPERIMENTAL RESULTS AND DISCUSSION

5.1   Differential Thermal Analysis Results

The understanding of the crystallization kinetics of magnetic amorphous alloys is of scientific interest as it represents a phase transformation occurring under extreme conditions far from equilibrium. Crystallization kinetics is often determined from differential thermal analysis (DTA) or differential scanning calorimetry (DSC), where the onset of crystallization, the temperature of crystallization and secondary crystallization events can be revealed. Calorimetric studies of amorphous alloys provide substantial fundamental information concerning the kinetics of crystallization and structural relaxation effects. The kinetics of the on set of crystallization have been studied calorimetrically by Clements and Cantor [5.1] and both calorimetrically and magnetically by Luborsky [5.2] in a variety of amorphous magnetic alloys.

The considerations for synthesizing amorphous metallic alloys often at add with the consideration for optimizing properties. This is because the addition of typical glass forming agents has a deleterious effect on such intrinsic magnetic properties as the saturation induction and the Curie temperature and composition of the eutectic, the terminal phases to the right and left of the eutectic composition, the slope of the liquidus as a function of composition etc. Since the amorphous alloy is to be used as a precursor for the production of FINEMET of Fe-Si-B-Cu-N based nanocrystalline material the primary and secondary crystallization temperature are of importance. Because the structure of the beneficial ferromagnetic nanocrystalline phase is composed of Fe-Si which is the product of primary crystallization. The secondary crystallization product is the Fe-B phase. This phase is detrimental for the soft magnetic properties because of its high anisotropy energy.

In the present investigation DTA technique has been used to study the crystalline behavior of nanocrystalline alloys $Fe_{73.5}Cu_1M_3Si_{13.5}B_9$, (M = Mo & W) and $Fe_{71.5}Cr_2Cu_1Nb_3Si_{13.5}B_9$. From the DTA curves of different heating rates the crystallization activation energies of different phases can be calculated using heating rate and crystallization peak temperature. DTA data are then analyzed within the framework of kinetic rate law and activation energy for corresponding crystallization peak extracted.

53

5.1.1 DTA Results of Nanocrystalline Amorphous Ribbon with Composition $Fe_{71.5}Cr_2Cu_1Nb_3Si_{13.5}B_9$

DTA trace of as-cast nanocrystalline amorphous ribbon sample recorded in a nitrogen atmosphere with a heating rate $10^0 C/_{min}$ has been presented in fig.-5.1. Two exothermic peaks are observed which corresponds to two different crystallization events at temperature T_{X_1} and T_{X_2} respectively. The softest magnetic ribbon corresponds to those in which primary crystallization (T_{X_1}) of α-Fe(Si) takes place. Secondary crystallization (T_{X_2}) of Fe_2B caused magnetic hardening of the nanocrystalline alloy. Mechanical hardening of the amorphous precursor has been observed in incipient primary crystallization and attributed to Cu nucleation. Two anomalies observed in the DTA curve are at 509°C and 650°C respectively. Both the anomalies are followed by sharp peaks, which corresponds to the release of heat at these temperatures due to change in the ordering of the atoms.
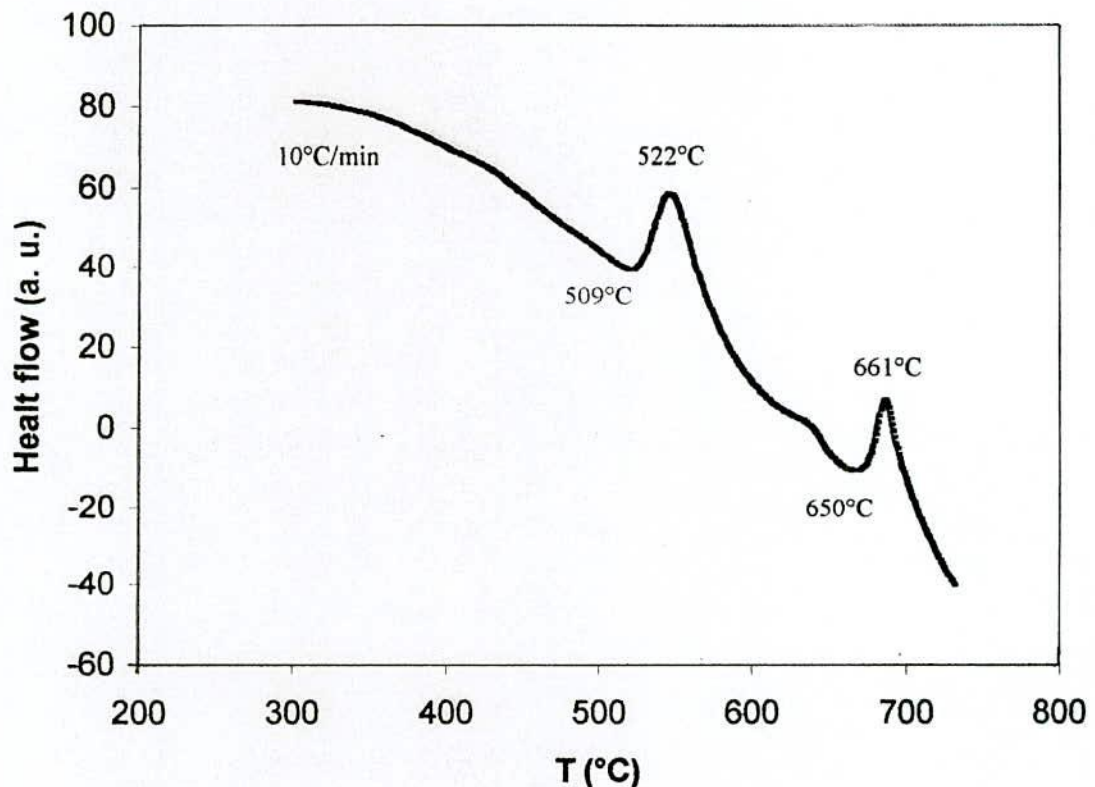
Fig.5.1   DTA trace of the as-cast nanocrystalline amorphous ribbon with composition $Fe_{71.5}Cr_2Cu_1Nb_3Si_{13.5}B_9$

Fig.5.2 shows DTA traces of $Fe_{71.5}Cr_2Cu_1Nb_3Si_{13.5}B_9$ amorphous ribbons taken in nitrogen atmosphere with heating at the rate of $10 - 50^0 C/min$ at the step of 10°C with continuous heating from room temperature to 800°C. It is observed that the crystallization of each phase has occurred over a wide range of temperatures and that the peak temperatures shift to higher values with the increase of heating rate. The crystallization of each phase occurs over a wide range of temperature.

Fig.5.2   Effects of heating rate on DTA traces of the nanocrystalline amorphous ribbon with composition $Fe_{71.5}Cr_2Cu_1Nb_3Si_{13.5}B_9$

In table-1 crystallization peak temperatures of two phases $\left(T_{p_1} \& T_{p_2}\right)$ and crystallization starting temperatures of two phases $\left(T_{X_1} \& T_{X_2}\right)$ are given for different heating rates.

Table - 5.1 Effects of heating rate on 1st and 2nd crystallization states of the nanocrystalline amorphous ribbon with composition $Fe_{71.5}\,Cr_2Cu_1Nb_3Si_{13.5}B_9$

Heating rate in $^0C/min$	1st starting T_{X_1} °C	1st peak T_{p_1} °C	Temperature range of 1st state in °C	2nd Starting T_{X_2} °C	2nd peak T_{p_2} °C	Temperature Range of 2nd State in °C	$T_{p_2} - T_{p_1}$ in °C
10	509	522	13	650	661	11	139
20	516	532	16	657	672	15	140
30	518	537	19	661	679	18	142
40	520	544	24	665	680	15	136
50	522	547	25	668	686	18	139

It has been observed that crystallization temperature range of first phase occurred within 13°C to 25°C but this range for the crystallization of second phase is 11°C to 18°C. So it is notable that the crystallization temperature range for the first peak is always larger than the second peak. It is also observed that the peak temperature shifts to higher values and the crystallization temperature range increases with the increase of heating rates. From fig 5.2 it is seen that two crystallization phenomena have taken place within a large temperature gap of around 140°C.

The activation energy of crystallization of T_{X_1} and T_{X_2} phases have been calculated using Kissinger equation [(5.3)]

$$\beta = T_p^2 e^{-E/KT_p}$$

$$\ln\left(\frac{\beta}{T_p^2}\right) = -\frac{E}{KT_p}$$

$$E = -KT_p \ln\left(\frac{\beta}{T_p^2}\right), \qquad\qquad (5.1)$$

where β is the heating rate, T_p is the crystallization peak temperature, E is the activation

Fig.5.3 $\frac{1}{T_p} \times 10^3$ versus $\ln\left(\frac{\beta}{T_p^2}\right)$ curve for T_{x_1} phase of the nanocrystalline amorphous

ribbon with composition $Fe_{71.5}Cr_2Cu_1Nb_3Si_{13.5}B_9$

Fig.5.4 $\frac{1}{T_p} \times 10^3$ versus $\ln\left(\frac{\beta}{T_p^2}\right)$ curve for T_{x_2} phase of the nanocrystalline amorphous

ribbon with composition $Fe_{71.5}Cr_2Cu_1Nb_3Si_{13.5}B_9$

energy and k is the Boltzmann constant. The activation energy of T_{X_1} [$\alpha - Fe(Si)$] and T_{X_2} [Fe_2B] phases have been calculated using Kissinger plot shown in fig.-5.3 and fig.-5.4 and are depicted in table-5.4. It is seen that the first thermal crystallization activation energy of $\alpha - Fe(Si)$ phase (E_1) is 2.45eV and second Fe_2B phase (E_2) is 3.43eV.

5.1.2 DTA Results of Nanocrystalline Amorphous Ribbon with Composition $Fe_{73.5}Cu_1Mo_3Si_{13.5}B_9$

Fig.5.5 shows DTA traces of $Fe_{73.5}Cu_1Mo_3Si_{13.5}B_9$ amorphous ribbons measured in nitrogen atmosphere with heating rate of $10 - 50^0 C/min$ at the step of 10°C with continuous heating from room temperature to 800 °C. Two well defined exothermic peaks typical for two steps of crystallization processes are manifested from the DTA traces. The first one corresponds to the crystallization of α- Fe-Si phase and the second one is related to the crystallization of Fe_2B. The on set of crystallization temperatures T_{X_1} & T_{X_2} have been estimated from the DTA data. In table-5.2 crystallization peak temperatures of two phases $(T_{p_1}$ & $T_{p_2})$ and crystallization onset temperatures $(T_{X_1}$ & $T_{X_2})$ are given for different heating rates.

Table - 5.2 Effects of heating rate on 1st and 2nd crystallization states of the nanocrystalline amorphous ribbon with composition $Fe_{73.5}Cu_1Mo_3Si_{13.5}B_9$

Heating rate in $^0C/min$	1st starting T_{X_1} °C	1st peak T_{p_1} °C	Temperature range of 1st state in °C	2nd Starting T_{X_2} °C	2nd peak T_{p_2} °C	Temperature range of 2nd state in °C	$T_{p_2} - T_{p_1}$ in °C
10	470	483	13	577	587	10	104
20	478	492	14	584	596	12	104
30	484	499	15	588	598	10	99
40	486	502	16	592	600	8	98
50	488	506	18	596	610	14	104

It is observed that the crystallization of first phase has occurred over a temperature range of 13°C to 18°C. But this range for the second phase is 8°C to14°C.
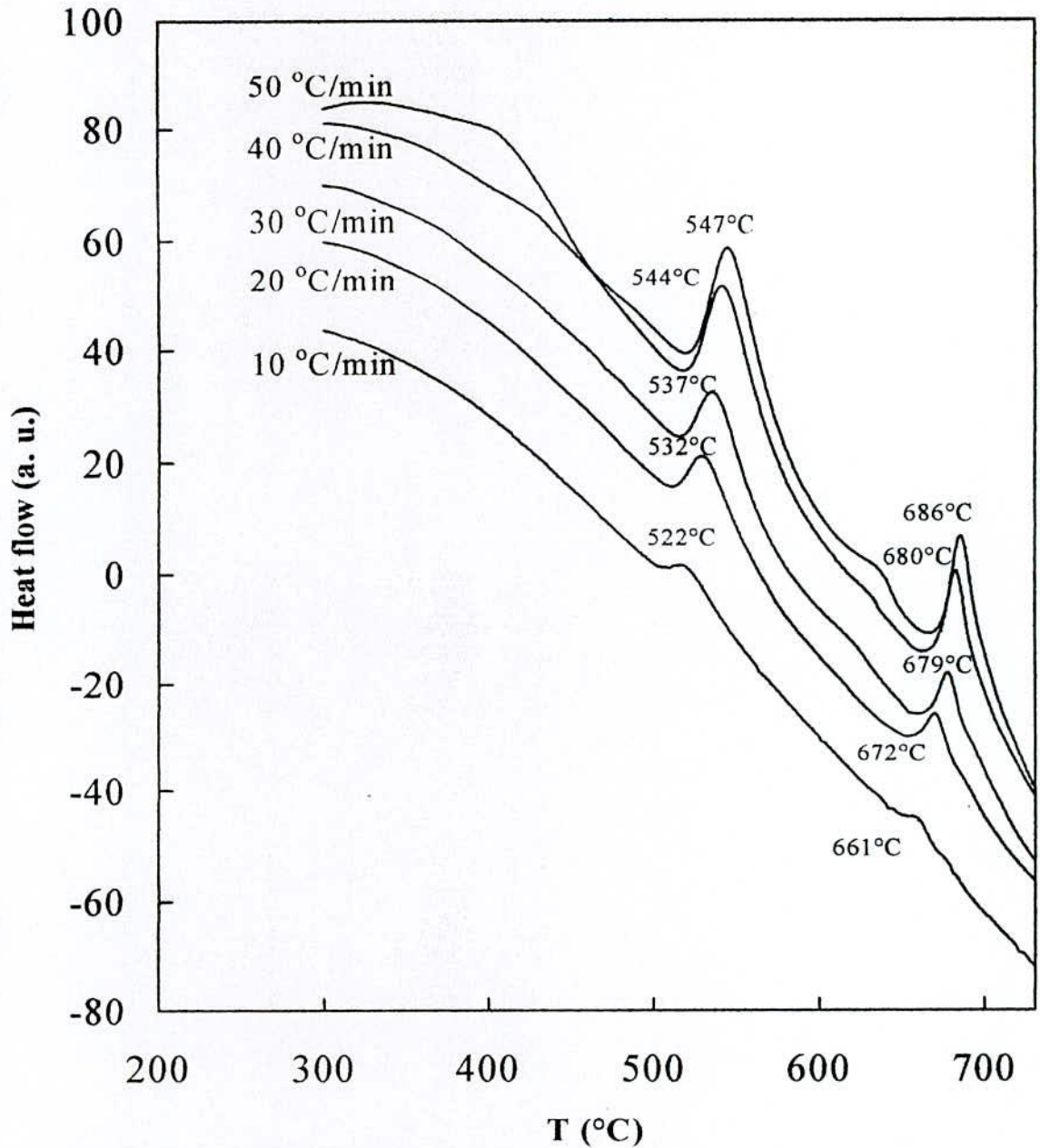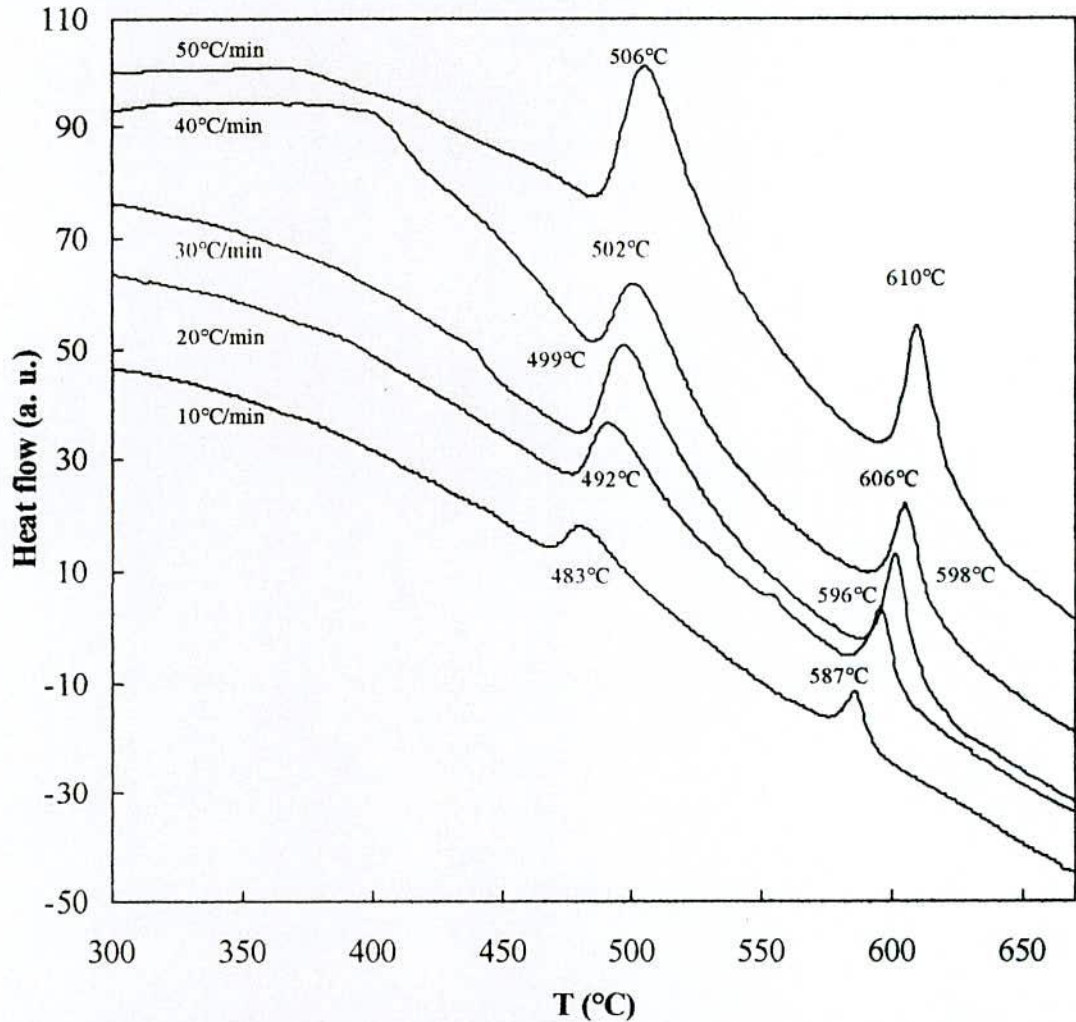

Fig.5.5   Effects of heating rate on DTA traces of the nanocrystalline amorphous ribbon with composition $Fe_{73.5}Cu_1Mo_3Si_{13.5}B_9$

So it is notable that this crystallization temperature range for the first peak is always larger than the second peak. It is also observed that the peak temperature shifts to higher values and the crystallization temperature range increases with the increase of heating rates. The crystallization temperature range for the first peak continues increasing with the increasing of heating rates. The crystallization temperature range for the second peak shows similar behavior except with the heating rate of 30°C/min and 40°C/min. From fig.5.5 it is seen that two crystallization phenomena have taken place within a temperature gap of around 100°C.This temperature gap is smaller than the Cr substituted counterpart.
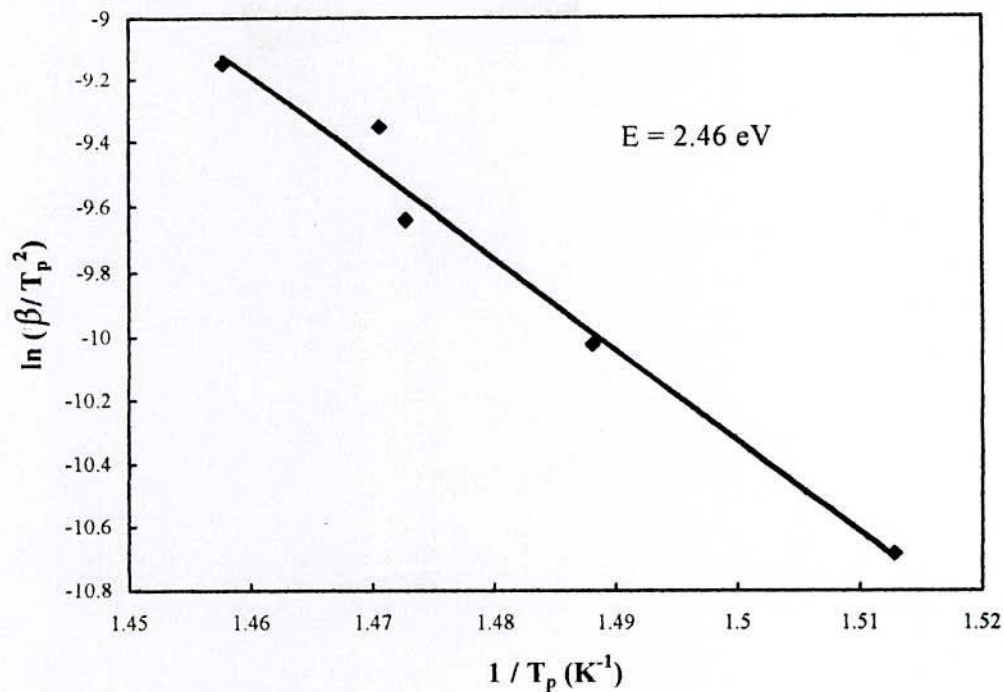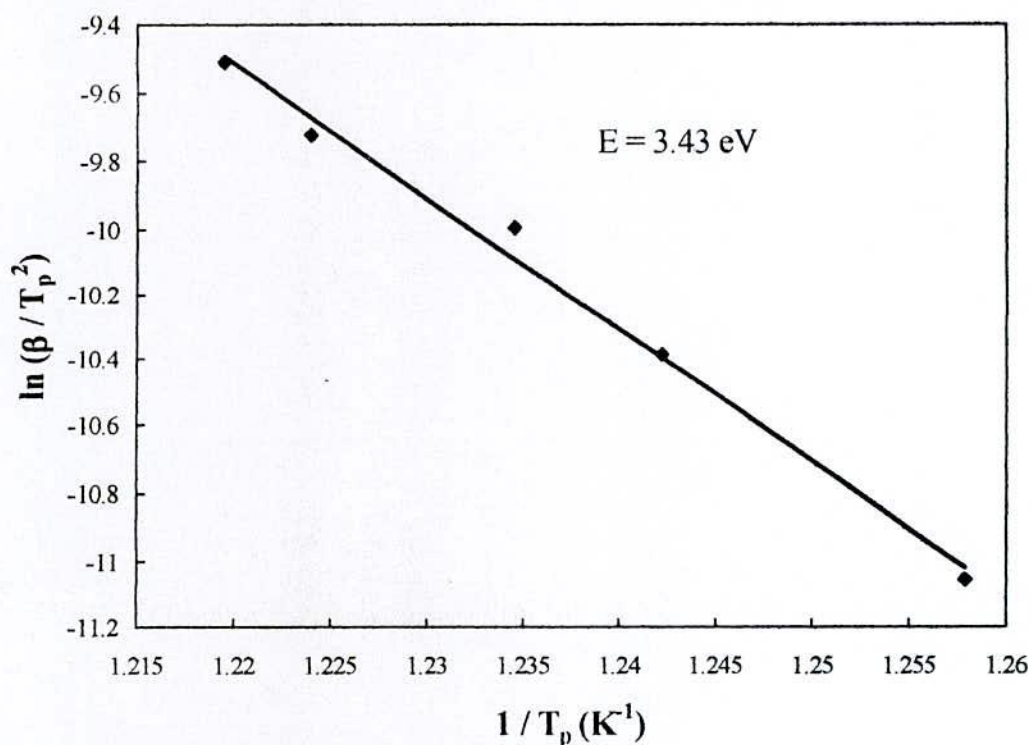
Fig.5.6 $\frac{1}{T'_p} \times 10^3$ versus $\ln\left(\frac{\beta}{T_p^2}\right)$ curve for T_{x_1} phase of the nanocrystalline amorphous

ribbon with composition $Fe_{73.5}Cu_1Mo_3Si_{13.5}B_9$

Fig.5.7 $\frac{1}{T'_p} \times 10^3$ versus $\ln\left(\frac{\beta}{T_p^2}\right)$ curve for T_{x_2} phase of the nanocrystalline amorphous

ribbon with composition $Fe_{73.5}Cu_1Mo_3Si_{13.5}B_9$

The activation energy of T_{X_1} [$\alpha - Fe(Si)$] and T_{X_2} [Fe_2B] phases have been calculated using Kissinger plot as shown in fig.5.6 and fig.5.7 and the values are depicted in table-5.4. It is seen that the first thermal crystallization activation energy for $\alpha - Fe(Si)$ phase (E_1) is 3.42eV and that of second Fe_2B phase (E_2) is 4.38eV.

5.1.3 DTA Results of Nanocrystalline Amorphous Ribbon with Composition $Fe_{73.5}Cu_1W_3Si_{13.5}B_9$

Fig.5.8 shows DTA diagram of amorphous $Fe_{73.5}Cu_1W_3Si_{13.5}B_9$ ribbons measured in nitrogen atmosphere with heating at the rate of $10-40^0 C/min$ with the step of 10°C with continuous heating from room temperature to 800 °C. Two well defined exothermic peaks typical for two steps of crystallization processes are manifested from the DTA traces. The first one corresponds to the crystallization of α-Fe-Si phase and the second one is related to the crystallization of Fe_2B phase. The on set of crystallization temperatures T_{X_1} & T_{X_2} have been estimated from the data of DTA curve. In table-5.3 crystallization peak temperatures of two phases $\left(T_{p_1} \& T_{p_2}\right)$ and crystallization starting temperatures $\left(T_{X_1} \& T_{X_2}\right)$ are illustrated for different heating rates.

Table - 5.3 Effects of heating rate on 1st and 2nd crystallization states of the nanocrystalline amorphous ribbon with composition $Fe_{73.5}Cu_1W_3Si_{13.5}B_9$

Heating rate in $^0C/min$	1st starting T_{X_1} °C	1st peak T_{p_1} °C	Temperature range of 1st state in °C	2nd Starting T_{X_2} °C	2nd peak T_{p_2} °C	Temperature range of 2nd state in °C	$T_{p_2} - T_{p_1}$ in °C
10	460	471	11	540	549	9	78
20	470	482	12	550	560	10	78
30	472	485	13	555	566	11	81
40	480	495	15	563	575	12	80
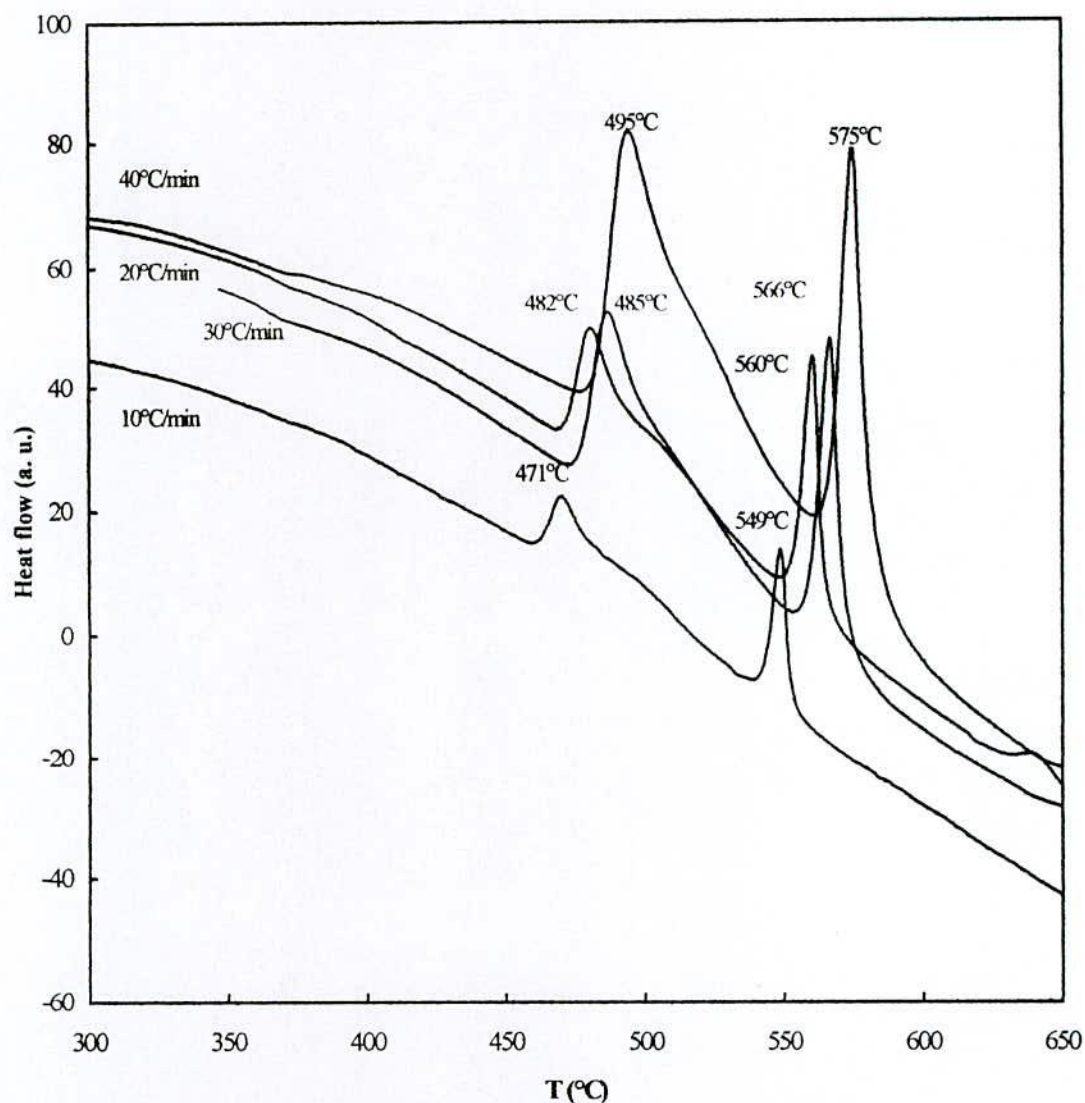
Fig.5.8   Effects of heating rate on DTA traces of the nanocrystalline amorphous ribbon with composition $Fe_{73.5}Cu_1W_3Si_{13.5}B_9$

It is observed that the crystallization of first phase has occurred within the temperature range of 11°C to 15°C. But this range for the second phase is 9°C to12°C. So it is notable that this crystallization temperature range for the first peak is always larger than the second peak. It is also observed that the peak temperature shifts to higher values and the crystallization temperature range increases with the increase of heating rates i.e. enthalphies. From fig.5.8 it is seen that two crystallization phenomena have taken place within a temperature gap around 80°C. This temperature gap is smaller than the other two studied alloys.
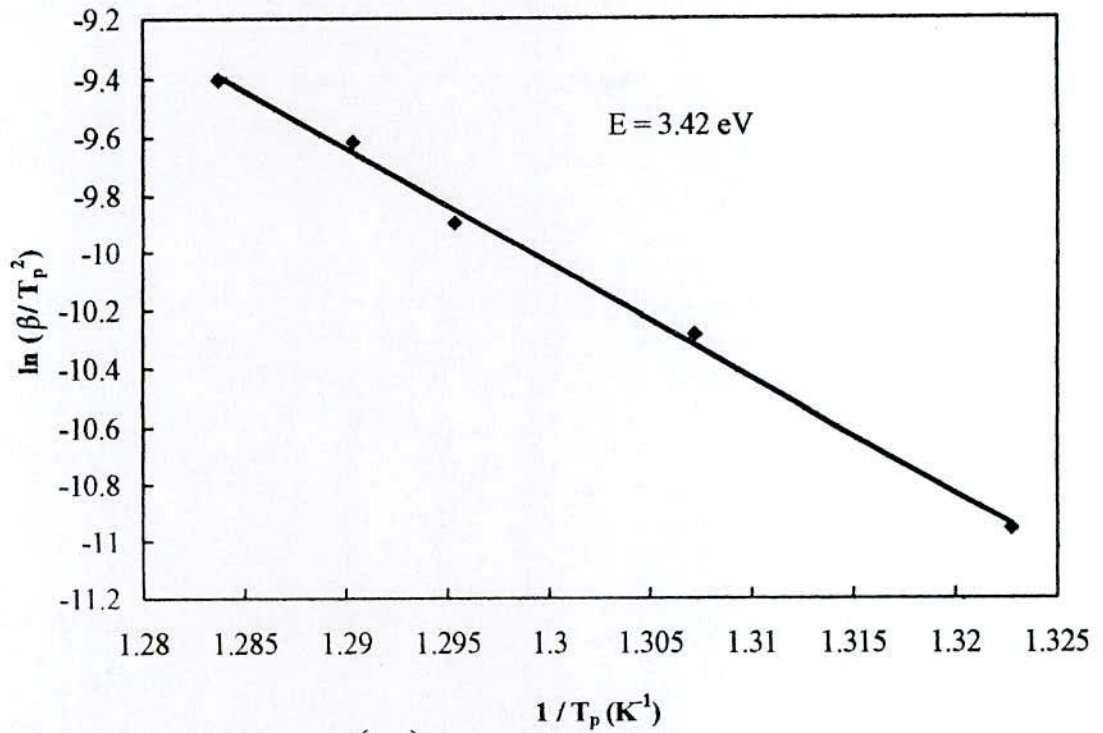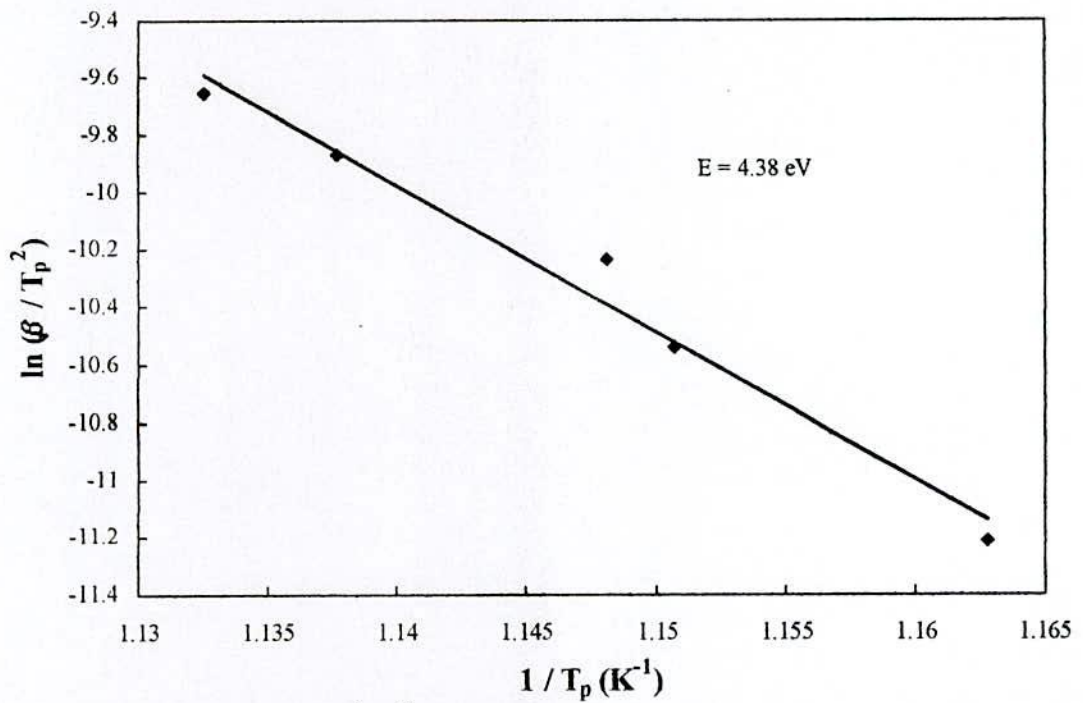
Fig.5.9 $\quad \dfrac{1}{T_p} \times 10^3$ versus $\ln\left(\dfrac{\beta}{T_p^2}\right)$ curve for T_{x_1} phase of the nanocrystalline amorphous

ribbon with composition $Fe_{73.5}Cu_1W_3Si_{13.5}B_9$

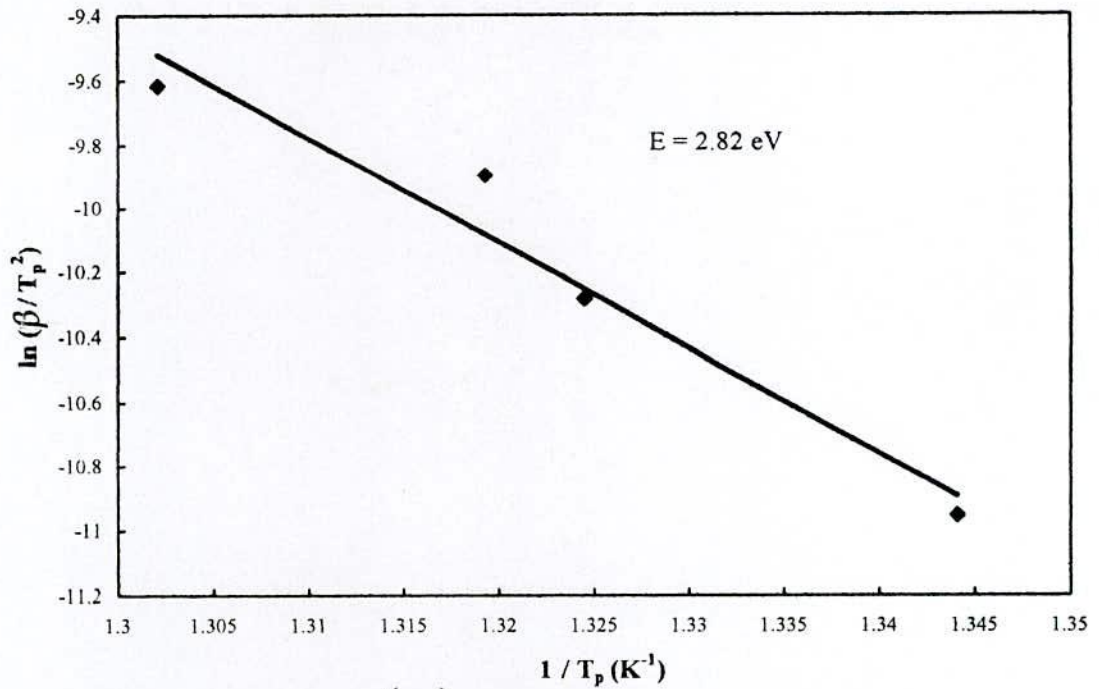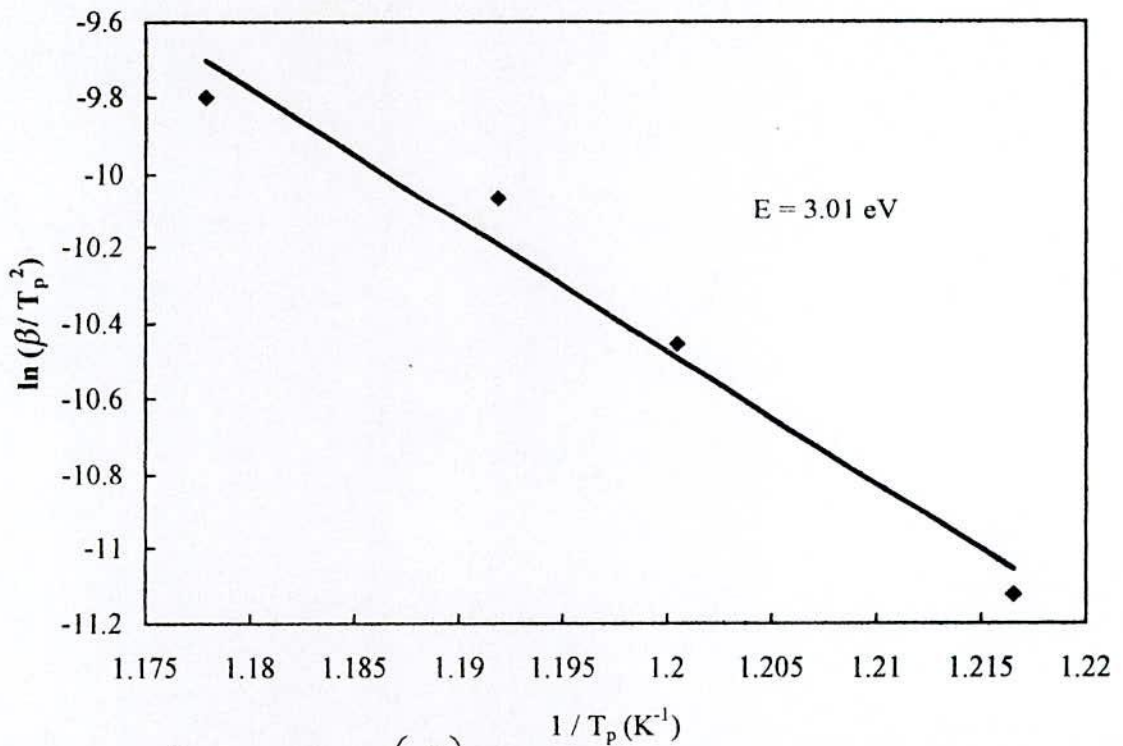Fig.5.10 $\quad \dfrac{1}{T_p} \times 10^3$ versus $\ln\left(\dfrac{\beta}{T_p^2}\right)$ curve for T_{X_2} phase of the nanocrystalline amorphous

ribbon with composition $Fe_{73.5}Cu_1W_3Si_{13.5}B_9$

The activation energy of T_{X_1} $[\alpha - Fe(Si)]$ and T_{X_2} $[Fe_2B]$ phases have been calculated using Kissinger plot and shown in fig.5.9 and fig.5.10 and the values are depicted in table-5.4. It is seen that the first thermal crystallization activation energy $\alpha - Fe(Si)$ phase (E_1) is 2.82eV and second Fe_2B phase (E_2) is 3.01eV.

5.1.4 Compare DTA Results Analysis between $Fe_{71.5}Cr_2Cu_1Nb_3Si_{13.5}B_9$ and $Fe_{73.5}Cu_1M_3Si_{13.5}B_9$ (M = Mo & W) Samples

From the DTA study it is well accepted that the crystallization characteristics of amorphous nanocrystalline alloys are strongly dependant on heating rate, temperature and also the alloy compositions. The crystallization temperature range between initiation of crystallization and peak temperature is different for the three samples with respect to the peaks T_{p1} and T_{p2}. The crystallization temperatures for the three samples are different. The order of the three samples with respect to their crystallization temperature range and peak temperature can be arranged.

$$Fe_{71.5}\,Cr_2Cu_1Nb_3Si_{13.5}B_9 > Fe_{73.5}Cu_1Mo_3Si_{13.5}B_9 > Fe_{73.5}Cu_1W_3Si_{13.5}B_9$$

The temperature difference between T_{p1} and T_{p2} are 140°C for the composition $Fe_{71.5}\,Cr_2Cu_1Nb_3Si_{13.5}B_9$, 100°C for the composition $Fe_{73.5}Cu_1Mo_3Si_{13.5}B_9$, 80°C for the composition $Fe_{73.5}Cu_1W_3Si_{13.5}B_9$. The change in temperature difference also obey the mentioned order. From all the DTA curves it is observed that 1st peak is greater than the 2nd one. It is evident that the 1st peak associated always with the primary crystallization becomes more prominent than the 2nd one, with the increase of heating rate something that has already been observed through DSC measurement [5.4].

In table-5.4 the experimental value of DTA parameters of three samples are given. In this table few DTA parameters which are taken from the work of different authors for the comparison are presented. From Table 5.4 it is seen that T_{p1} for the sample with 3% Nb measured by different authors are in a range of 542°C – 570°C but for the present the sample with Nb 3% is obtained 522°C-547°C which shows a low value. It may be due to the substitution of 2% Cr by Fe. The other two experimental samples are just substitution of 3% Nb by 3% Mo and 3% W. T_{p1} for the sample with 3% Mo is lower than the sample with 3% Nb. T_{p1} for the samples with W_3 is lower than all the samples. This order also exists for the 2nd crystallization temperature.

Table – 5.4   Activation energy & peak temperature of different samples

Sample	Heating rate in $^{o}C/min$	T_{P_1} in °C	T_{P_2} in °C	E_1 in eV	E_2 in eV
$Fe_{71.5}Cr_2Cu_1Nb_3Si_{13.5}B_9$	10 –50	522 -547	661 -686	2.46	3.43
$Fe_{73.5}Cu_1Nb_3Si_{13.5}B_9$ [5.5]	40	562°C		4.3	
$Fe_{73.5}Cu_1Nb_3Si_{13.5}B_9$ [5.6]	10 –50	542 -570	686 -719	3.21	3.81
$Fe_{72.5}Cr_1Cu_1Nb_3Si_{13.5}B_9$ [5.7]				2.85	3.74
$Fe_{70.5}Cr_3Cu_1Nb_3Si_{13.5}B_9$ [5.7]				2.82	3.59
$Fe_{73.5}Cu_1Mo_3Si_{13.5}B_9$	10 -50	483-506	587-610	3.42	4.38
$Fe_{73.5}Cu_1W_3Si_{13.5}B_9$	10-40	471- 495	549-575	2.82	3.01

Activation energies of the 1st crystalline phase of all the samples with 3% Nb are shown in the range of 2.82 eV - 4.3 eV. But for the present the sample with 3% Nb this value is 2.46 eV which very lower than the above range. Phuc et al [5.8] shows that activation energy depends on % of Cr component that is substituted for Fe. Activation energy increases with decrease of Cr %. From this point the activation energy of the composition with $Fe_{71.5}Cr_2Cu_1Nb_3Si_{13.5}B_9$ must be in between 2.82-2.85 eV. But present result does not agree with this conclusion. The activation energy of the sample with 3% Mo is higher than other two experimental samples with W and Nb. The activation energy of the sample with W shows the lowest value. The nature of the 2nd phase is also maintains this order.

Crystallization process is affected by the heating rate as well as by compositions. The composition of the alloy affects both the primary and secondary crystallization process, because the time needed for the constituent atom to have long range order depends on their bond energies [5.9-5.10]. The formation of nucleation centers and their growth need to be inhibited to avoid crystallization on the stability of the crystalline amorphous state is thus studied keeping the heating rate constant. It should be stressed again that good soft magnetic properties require not only a small grains size but at the same time the absence of boron compounds. The amorphous state that maintains its

amorphosity against annealing temperature is said to be stable i.e. a sample with higher crystallization temperature is said to be stable. From this stability condition the stability of these three samples can be expressed as

$$Fe_{71.5}Cr_2Cu_1Nb_3Si_{13.5}B_9 > Fe_{73.5}Cu_1Mo_3Si_{13.5}B_9 > Fe_{73.5}Cu_1W_3Si_{13.5}B_9.$$
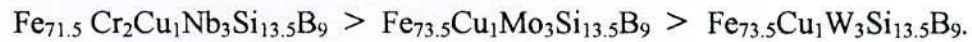
5.2 X-Ray Diffraction (XRD)

X-ray diffraction techniques has been an important tool in both the structural characterization and identification of phase has a prior for the in depth study of nanocrystalline materials. XRD has been used to identify crystalline phase in nanocrystalline materials. In the present work of three experimental nanocrystalline amorphous alloy ribbon were prepared by rapid quenching technique and the amorphous state was confirmed by XRD. However, the appearance of the best properties is sensitive to the alloy's annealing temperature. In the present work the above three samples are annealed at different temperature for 30 minute and every samples were taken under XRD analysis. From the output of XRD analysis three structural parameters such as (i) lattice parameter (a_0) (ii) grain size (D_g) and (iii) Si contents (Si) are calculated.

(i)   Lattice Parameter Calculation

Lattice parameter of crystalline bcc Fe-Si nanograin was determined at different annealing temperature of the experimental alloys. Structure of the bcc Fe-Si grains depends on the annealing temperature. Normally lattice parameter of an alloy composition is determined by the Debye-Scherrer method after extrapolation of the diffraction curve for the sample. Generally for an accurate determination of the lattice parameter a number of fundamental peaks are required but in this type of tailored materials upon crystallization only major fundamental peak (1 1 0) is used in calculation of a_0. We have, therefore, determine the lattice parameter using only that particular reflection using equation

$$2d \sin \theta = \lambda \text{ and } a_0 = d\sqrt{2} \qquad (5.2)$$

Where $\lambda = 1.54178$ Å of Cu - K_α radiation and a_0 is the determined lattice parameter of the grain, d is the inter-planner spacing and θ is the diffraction angle.

(ii)   Grain Size Determination

One of the most important aim of this study was to determine crystalline grain size for all the annealing temperatures. The gain size for all the samples was determined using Scherrer method. Grain size was determined from the XRD patterns of (110) reflections at constant annealing time from which grain size was determined using the formula, $D_g = \dfrac{0.9\lambda}{\beta\cos\theta}$ where $\lambda = 1.54178$ Å is the wavelength of Cu-K$_\alpha$ radiation. θ is the diffraction angle and β is the full width at half maximum (FWHM) of diffraction peak in radian for different steps of annealing temperature.

(iii)   Si Content in Nanograins

The major elements of the amorphous ribbon were Fe and Si with the concentration of 73.5 to 74.5 at % Fe and 13.5 at % Si. Crystalline nanograin were formed on the ribbon in the process of annealing temperature with the alloy composition of Fe-Si. It is therefore important to determine the concentration of Fe and Si and we have experimentally determined the lattice parameter of the alloy nanograins for the compositions of different annealing temperatures. It is easy to calculate the Si contents in the nanograins from the Pearson handbook relationship [5.11]. From this relationship we have considered a simple equation to calculate Si content from lattice parameter. This equation is

$$b = - 467\, a_0 + 1342.8 \qquad\qquad (5.3)$$

Where b is at % Si in the nanograins, a_0 is the lattice parameter of nanograins.

5.2.1 XRD Analysis of the Nanocrystalline Ribbon with Composition $Fe_{71.5}Cu_1Cr_2Nb_3Si_{13.5}B_9$

In the present work, structure of the $Fe_{71.5}Cu_1Cr_2Nb_3Si_{13.5}B_9$ nanocrystalline ribbon alloys, annealed at temperature from 450°C to 675°C for annealing time 30 minutes are investigated by the X-ray diffraction method. Fig.5.11 shows the diffraction spectra of quenched alloy and the alloy annealed at different temperatures for 30 minutes. In the figure, the indices of the reflecting planes are shown in the parenthesis X-ray diffraction results indicate that no α-Fe phases are present in the alloys annealed below 450°C for 30 minutes. When the alloys were annealed at or above 450°C, crystalline phase is developed on the amorphous ribbon. Patterns of $T_a = 500°C$ indicates a clear bcc α-Fe(Si) of said compositions after heat treatment for 30 minuets. The same pattern was

67

observed for all the samples at different annealing temperatures indicating the bcc α -Fe(Si) phase.

The XRD pattern has taken for the samples annealed from 450°C to 675°C under the same condition. The intensity of the diffracted peak of α -Fe(Si) phase in the alloy is increased with the increase of annealing temperature. All the results of θ, d values, FWHM from XRD analysis are listed in table - 5.5. Fig.5.12 shows the variation of lattice parameter, Si content and grain size of α -Fe(Si) phase with respect to the annealing temperature of the samples.
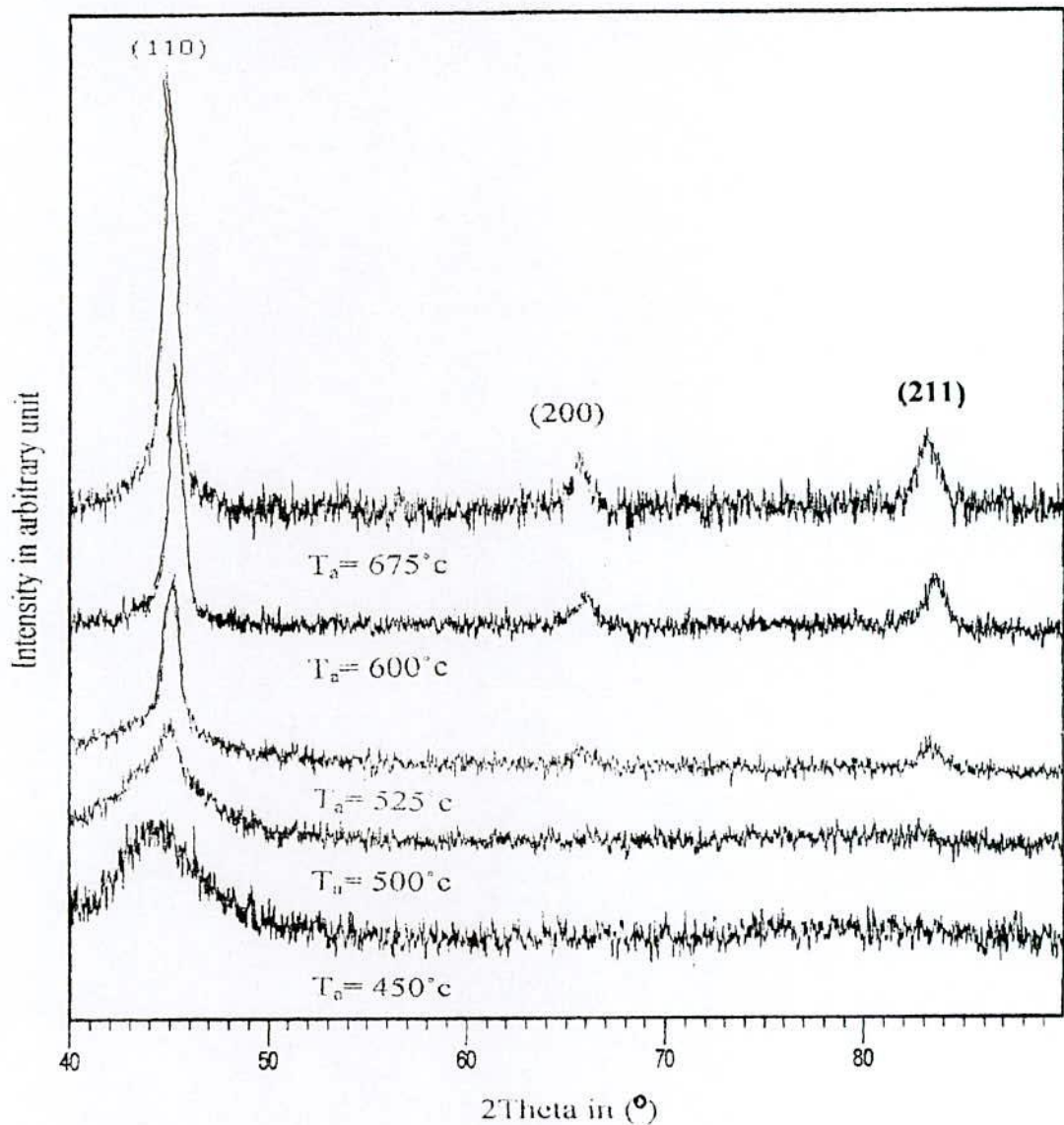
Fig.5.11   X – ray diffraction spectra of $Fe_{71.5}Cu_1Cr_2Nb_3Si_{13.5}B_9$ alloys of annealed at different temperatures

In fig.5.12 shows the lattice parameter of α -Fe(Si) crystallites embedded in the amorphous matrix of various annealed samples in the temperature from 500°C to 675°C has been performed. With the increase of annealing temperature lattice parameter decreases gradually up to 575°C above this temperature it drops rapidly and attains the minimum value at 600°C. For the annealing temperature above 600°C an increase of lattice parameter observed. The lattice parameter of α -Fe(Si) phase is always smaller than that of pure Fe, the value of which is 2.8664A [5.12]. When the annealing temperature is below 600°C there is a decrease of lattice parameter due to the contraction of α -Fe lattice as a result of diffusion of the Si with smaller grain size form a substitutional solid
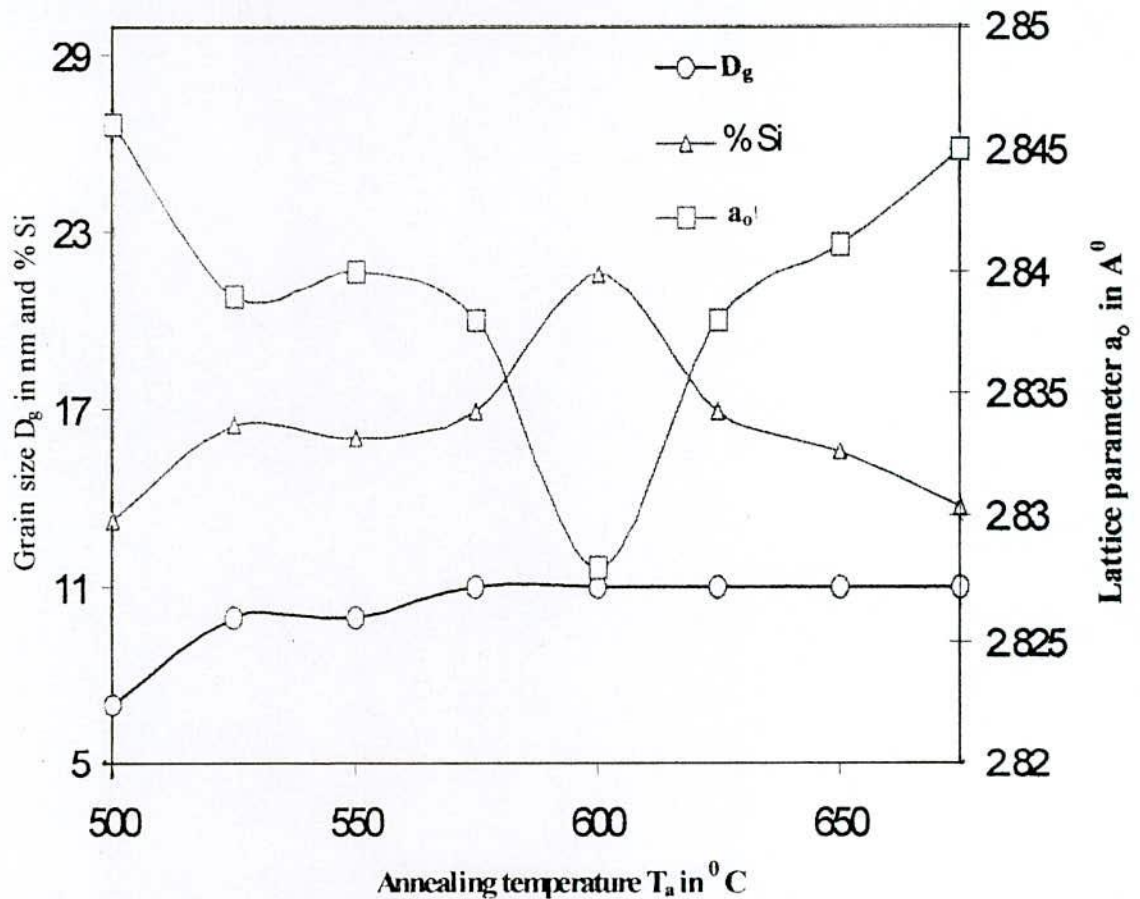
Fig.5.12   Variation of grain size, lattice parameter and Si – content with annealing temperature for the nanocrytalline amorphous ribbon with composition $Fe_{71.5}Cu_1Cr_2Nb_3Si_{13.5}B_9$

solution during the crystallization process of α –Fe-Si. When the annealing temperature is above 600°C some of the Si diffuses out of the α -Fe(Si) lattice and therefore the value of the lattice parameter increase again. From fig.5.12 has been observed that the Si content in α -Fe(Si) phase increases with annealing temperature from 500°C to 600°C. When

annealing temperature increases above 600°C then Si content decrease again. So Si content and lattice parameter is closely related which is expressed in Pearson Handbook Relationship[5.11].

Percentage of Si is the controlling parameter of structural change for the nanocrystalline alloy. Percentage of Si in the Fe-Si phase has a point of saturation i.e. maximum value. For this sample it is about 20.6% and obtained at 600°C. Above or below this critical annealing temperature % Si decreases i.e. lattice parameter increases.

From the Mössbauer study [5.13] maximum value of Si content in Fe-Si crystalline phase is estimated 21 at %. The maximum value of the Si content of this sample is obtained 20.6 at % that is compatible with the above result. Franko et-al [5.14] indicated that Si diffuses out of the α-Fe-Si nanaograins beyond 575°C. For this sample it happens at 600°C which satisfies the result of Franko et-al [5.14].

Table - 5.5   Experimental XRD data of nanocrystalline $Fe_{71.5} Cr_2Cu_1Nb_3Si_{13.5}B_9$ amorphous ribbon at different annealing temperatures

Temperature in °C	θ (°)	d (Å)	FWHM	a_0 (Å)	D_g (nm)	Si (at %)
500	22.52	2.0172	1.17	2.846	7	13.18
525	22.58	2.0078	0.87	2.839	10	16.45
550	22.57	2.0085	0.83	2.840	10	15.98
575	22.59	2.0071	0.80	2.838	11	16.91
600	22.67	2.0000	0.80	2.828	11	21.59
625	22.59	2.0071	0.80	2.838	11	16.91
650	22.56	2.0092	0.79	2.841	11	15.51
675	22.53	2.0120	0.78	2.845	11	13.64

All the values of grain size for every step of annealing temperature of the composition were determined and the values are listed in table – 5.5. In fig.5.11 it is clear that at low temperature the value of FWHM getting smaller. The peak is, therefore, getting sharper with the shifting of peak position towards higher 2θ value. This fact indicates that at 500°C the grain size is smaller in size, 7nm, and with increase of annealing temperature grain size is getting bigger in size within the range of 10 to11 nm.

Annealing at $T_a > 500°C$ leads to nanocrystallization of an Fe(Si) phase. In alloy with a Si content Si < 12 at. % crystallized in the ordered DO$_3$ structure. Mean grain size between 7 and 11 nm were observed depending on annealing temperature. Grain size, phase transition and transition temperatures were observed to depend on the Cu/Nb content. The magnetic properties are strongly correlated to the microstructural features.

5.2.2 XRD Analysis of the Nanocrystalline Ribbon with Composition Fe$_{73.5}$Cu$_1$Mo$_3$Si$_{13.5}$B$_9$

Fig.5.13 shows typical XRD patterns of bcc α- Fe (Si) phase for the sample of composition Fe$_{73.5}$Cu$_1$Mo$_3$Si$_{13.5}$B$_9$ after heat treatment (30 minutes) at different temperature.
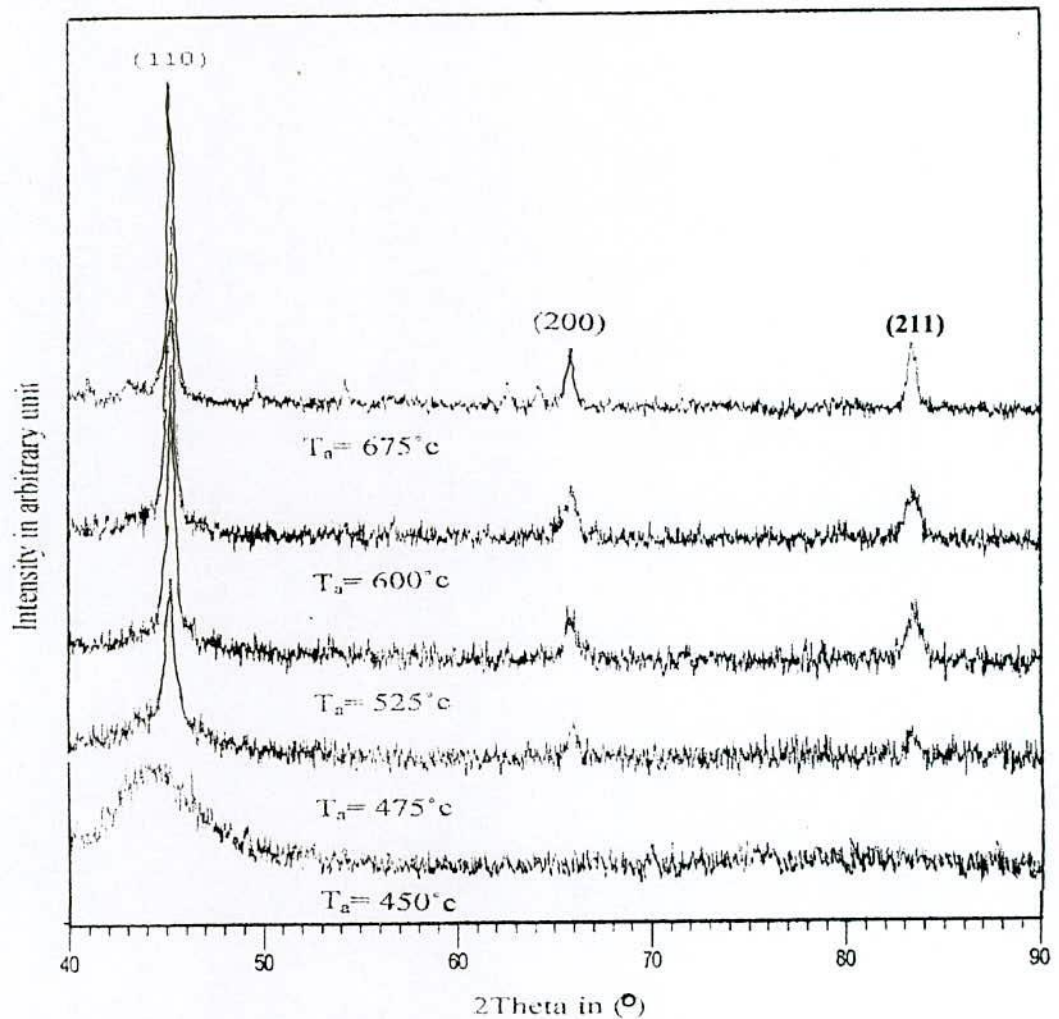
Fig.5.13   X – ray diffraction spectra of Fe$_{73.5}$Cu$_1$Mo$_3$Si$_{13.5}$B$_9$ alloys of annealed at different temperatures

From 450°C to 675°C pattern of $T_a = 450$°C indicates the amorphous nature. After heat treatment at $T_a = 475$°C initiation of crystallization takes place. The same patterns were observed for all samples at different annealing temperature indicating the bcc α- Fe (Si) phase which are developed on amorphous ribbon after heat treatment. Present experiment reveals that 475°C is not sufficient annealing temperature to form crystalline nanograins of bcc Fe — Si on the amorphous ribbon. Moreover, the bcc Fe phase is a unique crystalline of the alloys annealed at 475°C to 675°C, the variation of intensity of the diffraction lines in patterns obtained under the same condition, reveals that the peak of the bcc Fe –phase in the alloys is increased with increase of the annealing temperature of crystalline nanograin of bcc Fe – Si phase. All the results of θ, d–values, FWHM, a_0, D_g and Si (at %) at different annealing temperatures of these composition are listed in table – 5.6.

Fig.5.14 Variation of grain size, lattice parameter and Si — content with annealing temperature for the nanocrytalline amorphous ribbon with composition $Fe_{73.5}Cu_1Mo_3Si_{13.5}B_9$

In fig.5.14 the lattice parameter of α -Fe(Si) crystallites embedded in the amorphous matrix of various annealed samples in the temperature range between 475°C to 675°C has been performed. With the increase of annealing temperature lattice

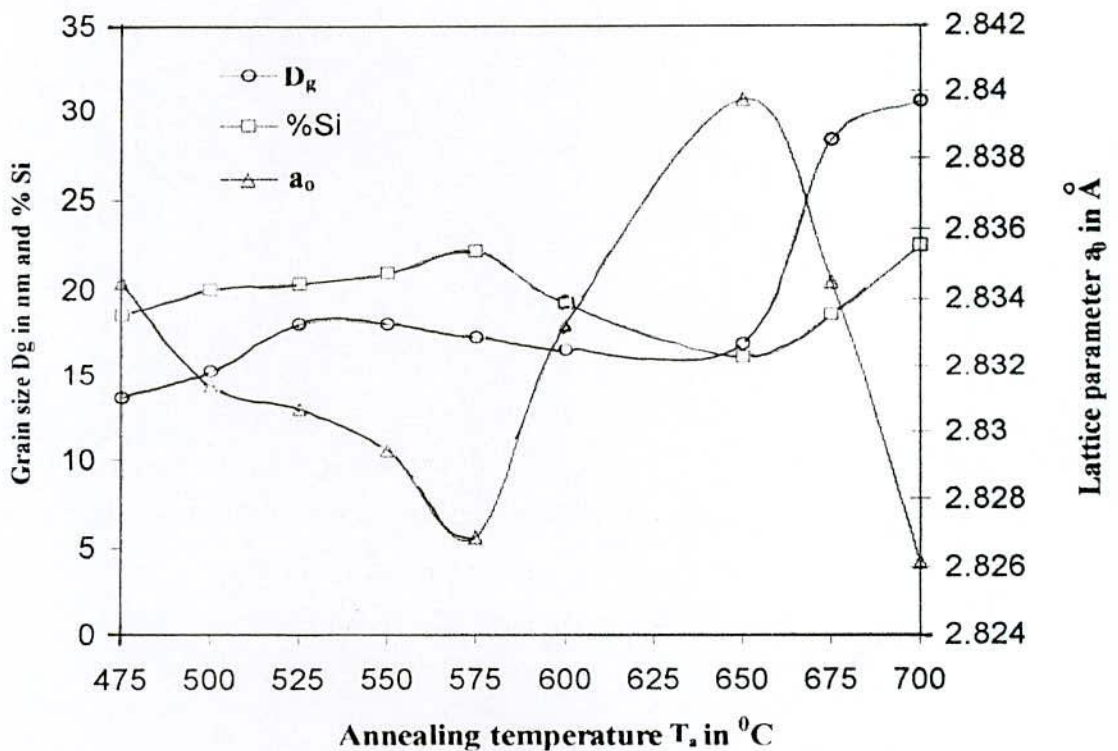parameter drops rapidly and attains the minimum value at 575°C. For the annealing temperature above 575°C an increase of lattice parameter observed. The lattice parameter of α -Fe(Si) phase is always smaller than that of pure Fe, the value of which is 2.8664Å[5.12]. When the annealing temperature is below 575°C there is a decrease of lattice parameter due to the contraction of α -Fe lattice as a result of diffusion of the Si with smaller grain size forming a substitutional solid solution during the crystallization process of α -Fe-Si. When the annealing temperature is above 575°C some of the Si diffuses out of the α -Fe(Si) lattice and therefore the value of the lattice parameter increase again. From fig.5.14 it is observed that the Si content in α -Fe(Si) phase increases with annealing temperature from 475°C to 575°C. When annealing temperature increases above 575°C then Si content decrease again. So Si content and lattice parameter are closely related that is expressed in Pearson Handbook [5.11].

Percentage of Si is the controlling parameter of structural change for the nanocrystalline alloy. Percentage of Si in the Fe-Si phase has a point of saturation i.e. maximum value. For this sample it is about 22.1% and obtained at 575°C. Above or below this critical annealing temperature % Si decreases as lattice parameter increases.

Table - 5.6   Experimental XRD data of nanocrystalline $Fe_{73.5}Cu_1Mo_3Si_{13.5}B_9$
amorphous ribbon at different annealing temperatures

Temperature in °C	θ (°)	d (Å)	FWHM	a_0 (Å)	D_g (nm)	Si (at %)
475	22.62	2.0046	0.63	2.8345	14	18.55
500	22.64	2.0024	0.57	2.8314	15	20.00
525	22.65	2.0019	0.48	2.8307	18	20.33
550	22.59	2.0010	0.48	2.8294	18	20.93
575	22.68	1.9992	0.50	2.8269	17	22.10
600	22.65	2.0014	0.52	2.8300	17	20.65
650	22.63	2.0038	0.51	2.8334	17	19.06
675	22.62	2.0046	0.31	2.8345	28	18.55

From the Mössbauer study [5.13] maximum value of Si content in Fe-Si crystalline phase is estimated as 21 at. %. The maximum value of the Si content of this sample is

obtained as 22.1 at % which is compatible with the above result. Franco et-al [5.14] indicated that Si diffuses out of the α-Fe-Si nanaograins beyond 575°C. For this sample it also happens at 575°C which satisfies the result of Franco et al [5.14].

In table – 5.6 it is clear that with the increase of annealing temperature the value of FWHM decreases. The peak is, therefore, getting sharper with the shifting of peak position forwards higher 2θ value.

In fig.5.14 the mean grain size of the nanograins determined from the X-ray fundamental line (110) using the Scherrers formula are presented. Grain size increases gradually up to the annealing temperature 525°C and than attains a limiting value 17 nm. This limiting value remains constant up to the annealing temperature of 650°C. Above 650°C the grain size increases rapidly and becomes 28 nm at 675°C.

5.2.3 XRD Analysis of the Nanocrystalline Ribbon with Composition $Fe_{73.5}Cu_1W_3Si_{13.5}B_9$

In the present work, structure of the $Fe_{73.5}Cu_1W_3Si_{13.5}B_9$ alloys, annealed at temperatures from 425°C to 600 °C, are investigated by the X–ray diffraction method. Fig.5.15 is the X–ray spectra of as–cast alloy and the annealed alloy at different temperature for 30 minutes. In the figure, the indices of the reflecting planes are shown in the parenthesis. X–ray diffraction results indicate that no α–Fe phases are present in the alloys annealed below 475°C for 30 minutes. When the alloys were annealed at or above 475°C, crystallization phase is developed on this sample.

XRD patterns at annealing temperature $T_a = 425$°C shows the amorphous state. Patterns of $T_a = 450$°C indicates a clear Fe_2B phase of $Fe_{73.5}Cu_1W_3Si_{13.5}B_9$ after heat treatment for 30 minuets. Patterns of $T_a = 475$°C indicates a clear α -Fe(Si) phase and Fe_2B phase of after heat treatment for 30 minutes. The same pattern was observed for all the samples at different annealing temperatures indicating the bcc α -Fe(Si) phase. The XRD pattern has taken for the samples annealed from 475°C to 600°C under the same condition. The intensity of the diffracted peak of α -Fe(Si) phase in the alloy is increased with the increase of annealing temperature. All the results of θ, d values, FWHM, a_o, D_g, Si (at %) at different annealing temperature of the composition are listed in table – 5.7.
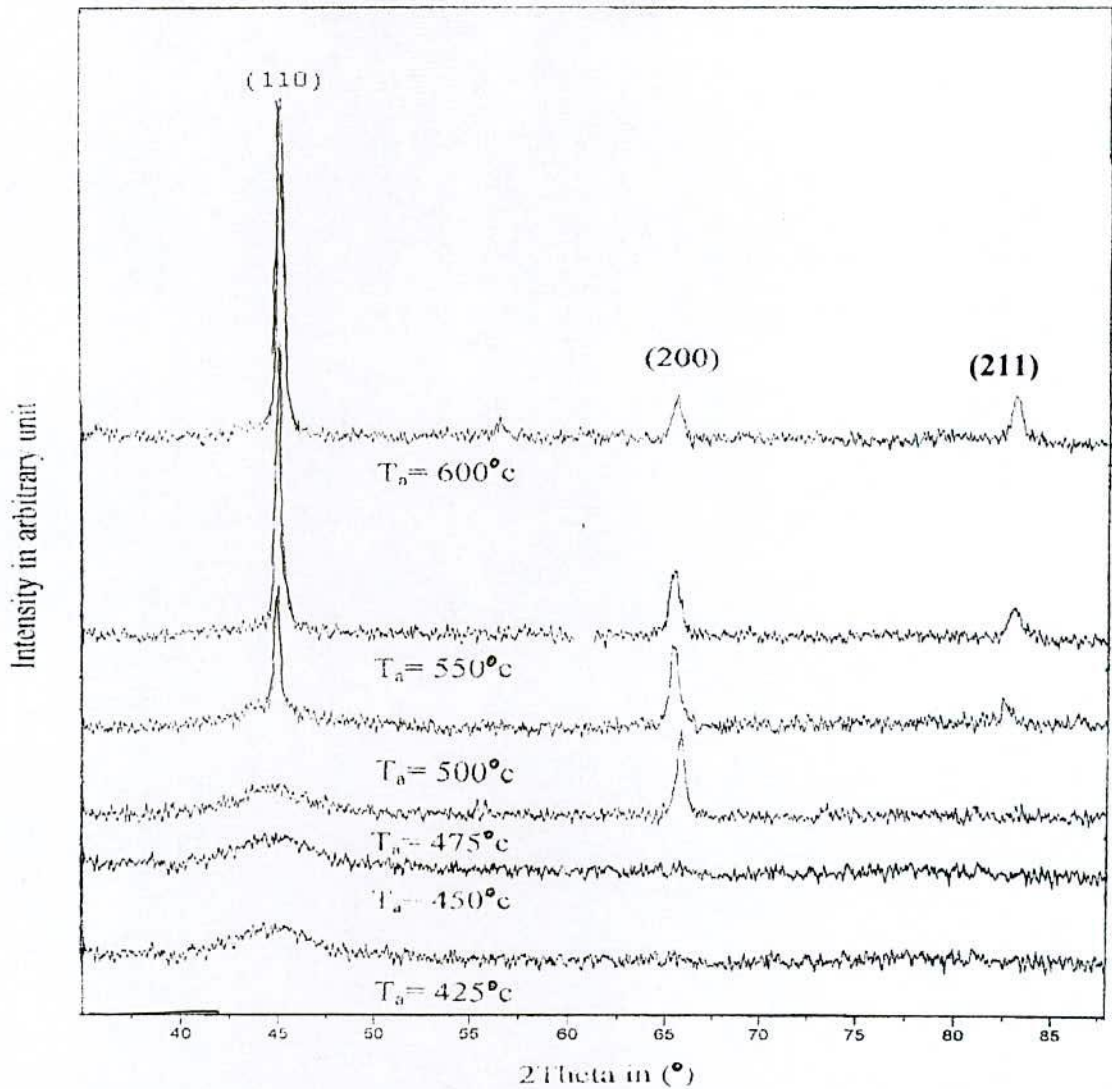
Fig.5.15 X – ray diffraction spectra of $Fe_{73.5}Cu_1W_3Si_{13.5}B_9$ alloys of annealed at different temperatures

In fig.5.16 shows the lattice parameter of α -Fe(Si) crystallites embedded in the amorphous matrix of various annealed samples in the temperature range from 475°C to 600°C has been performed. With the increase of annealing temperature lattice parameter decreases gradually up to 550°C. Above this temperature it drops rapidly and attains the minimum value at 600°C. But lattice parameter remains same for the temperature from 525°C to 550°C. The lattice parameter of α -Fe(Si) phase is always smaller than that of pure Fe, the value of which is 2.8664Å [5.12]. When the annealing temperature is below 600°C there is a decrease of lattice parameter due to the contraction of α -Fe lattice as a

result of diffusion of the Si with smaller grain size form a substitutional solid solution during the crystallization process of α -Fe-(Si).
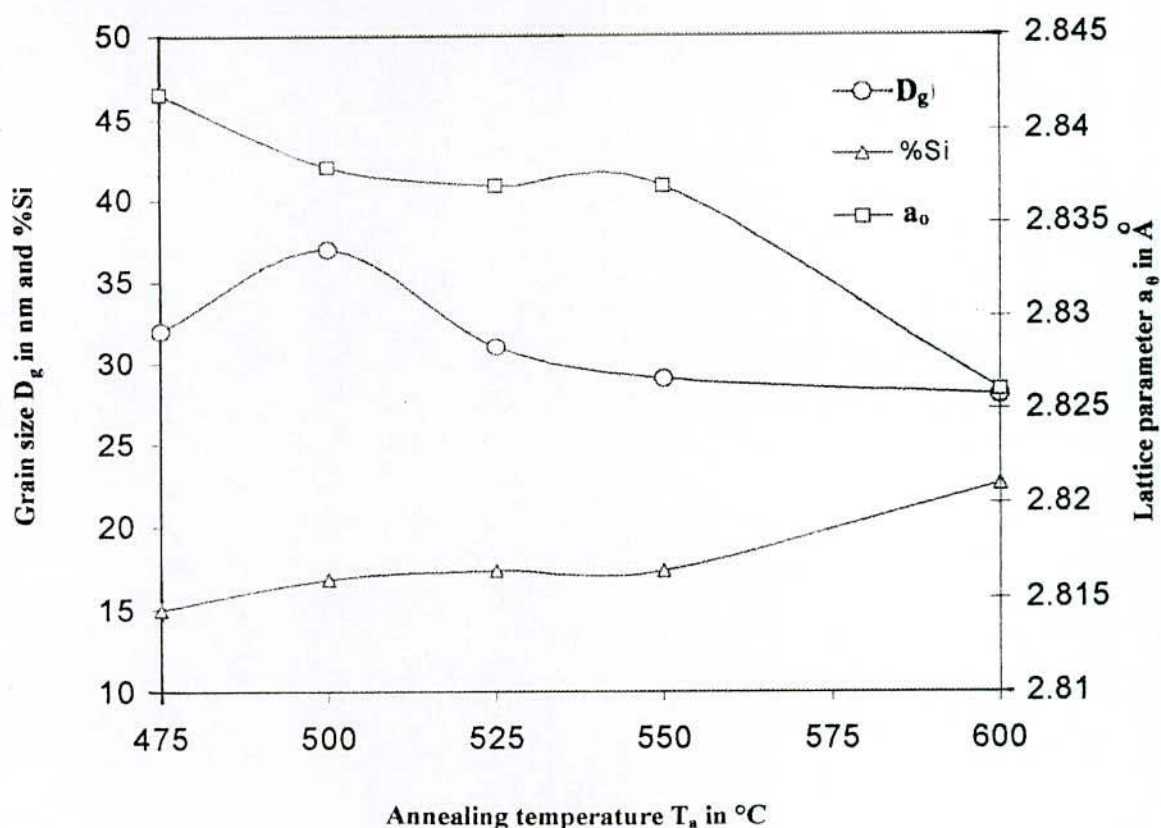
Fig.5.16   Variation of grain size, lattice parameter and Si – content with annealing temperature for the nanocrytalline amorphous ribbon with composition $Fe_{73.5}Cu_1W_3Si_{13.5}B_9$

From fig.5.16 it is observed that the Si content in α -Fe(Si) phase increases with annealing temperature. Percentage of Si is the controlling parameter of structural change for the nanocrystalline alloy. Percentage of Si in the Fe-Si phase has a point of saturation i.e. maximum value. For this sample it is about 22.6% and obtained at 600°C. No annealing has performed above 600°C so it cannot be concluded that 22.6% Si is the saturation value of this alloy. From fig.5.15 it is clear that at low temperature, 475°C the FWHM of the peak is large and with the increase of annealing temperature the value of FWHM decreases. The peak is, therefore getting sharper with the shifting of peak position towards higher 2θ value. This fact indicates that at 500°C the grain size is larger in 37 nm, and with increase of annealing temperature grain size decreases getting within the range 28 nm to 31 nm.

Table - 5.7   Experimental XRD data of nanocrystalline $Fe_{73.5}Cu_1W_3Si_{13.5}B_9$ amorphous ribbon at different annealing temperatures

Temperature in °C	θ (°)	d (Å)	FWHM	a_0 (Å)	D_g (nm)	Si (at %)
475	22.56	2.0098	0.27	2.842	32	15.05
500	22.59	2.0073	0.23	2.838	37	16.92
525	22.60	2.0064	0.28	2.837	31	17.38
550	22.60	2.0064	0.30	2.837	29	17.38
600	22.69	1.9984	0.31	2.826	28	22.57

In fig.5.16 the mean grain size of the nanograins determined from the X-ray fundamental line (110) using the Scherrers formula are presented. Grain size increases gradually up to the annealing temperature 500°C and then they attains a limiting value 37 nm. This limiting value decreases gradually and becomes 28 nm at 600°C.

5.3 Dynamic Magnetic Properties of Nanocrystalline Amorphous Magnetic Materials.

Dynamic magnetic properties of as-quenched nanocrystalline samples with composition $Fe_{71.5}Cr_2Cu_1Nb_3Si_{13.5}B_9$, $Fe_{73.5}Cu_1Mo_3Si_{13.5}B_9$, $Fe_{73.5}Cu_1W_3Si_{13.5}B_9$ respectively have been measured as a function of frequency in the range from 1 kHz to 500 kHz. Permeability measurements were performed on toroidal samples at frequency of 1 kHz to 500 kHz and an applied ac driving field (≈ 0.5 A/m) to ensure the measurements of initial permeability. Frequency spectrum of real and imaginary parts of initial permeability, loss factor and relative quality factor are analyzed. The measurement has been done in the as-cast and different annealing temperature with constant annealing time. In order to avoid experimental error due to fluctuation in ribbon thickness and thermal treatment, just one piece of each ribbon has been measured at room temperature after subsequent annealing temperature at constant annealing time. Magnetic properties of amorphous nanocrystalline magnetic materials are strongly depend on its annealing temperature. The magnetic properties of soft magnetic materials are mainly determined by the domain wall mobility specially in the range of irreversible magnetization. In the

present work initial magnetic permeability of the toroidal shaped samples annealed at different temperatures are measured to understand their soft magnetic properties and correlation with the micro structural features which are obtained from XRD analysis.

5.3.1 Frequency Dependence of Initial Permeability of $Fe_{71.5}Cr_2Cu_1Nb_3Si_{13.5}B_9$ Alloy with Different Annealing Temperature

The measurement has been done on as – cast specimen and also on samples annealed at 250°C to 650°C for 30 minuets as constant annealing time. Fig.5.17 shows the frequency dependence of the real part of the complex permeability for as cast and annealed sample in the temperature range 250°C to 530°C at constant annealing time 30 minutes. From this graph it is observed that the low frequency value of initial permeability increases with the increase of annealing temperature and attains the maximum value at the annealing temperature of 450°C. When the annealing temperature is higher than 450°C initial permeability decreases rapidly. This decrease of permeability may be attributed to the stress developed in the amorphous matrix by growing crystallite. At this temperature (450°C) the initiation of crystallization takes place.

Fig.5.18 shows the frequency dependence of the real part of the complex permeability at the annealed temperature from 540°C to 650°C with constant annealing time of 30 minuets. It is observed from the graph that the low frequency value of initial permeability increases with the increase of temperature and attains the maximum value at the annealing temperature of 560°C. When the annealing temperature is higher than 560°C low frequency value of initial permeability decreases rapidly. The trends of increasing low frequency permeability exist up to 560°C, i.e. maximum permeability (best soft property) is observed at this temperature.

From fig.5.17 it is seen that μ' maintains average value up to some critical frequency like 10 kHz for all the annealed samples. Above this critical frequency μ' drops rapidly due to the increase of loss component of complex permeability. From fig.5.18 the above mentioned nature is also observed for the samples annealed at 540°C to 650°C. But this critical frequency is lower than 10 kHz, it is approximately around 7 kHz.

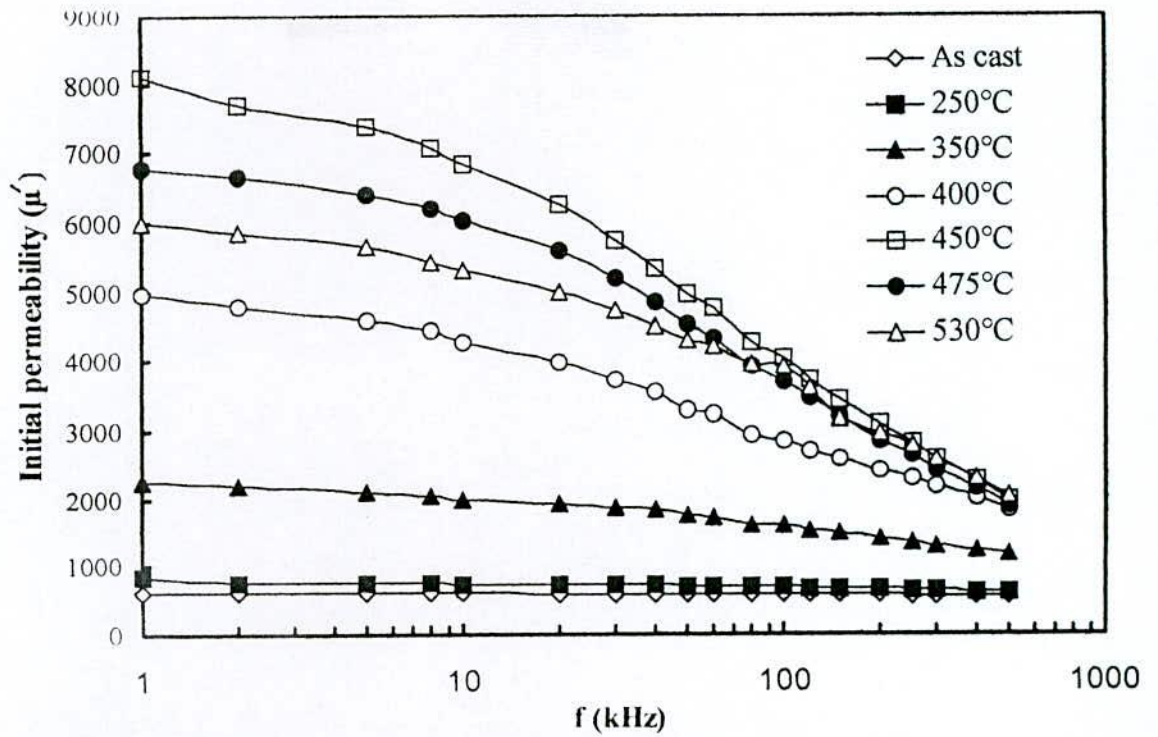Fig.5.17   Frequency dependence of real component of initial permeability of as–cast and different annealed samples for constant annealing time 30 minutes of $Fe_{71.5}Cu_1Cr_2Nb_3Si_{13.5}B_9$ alloy
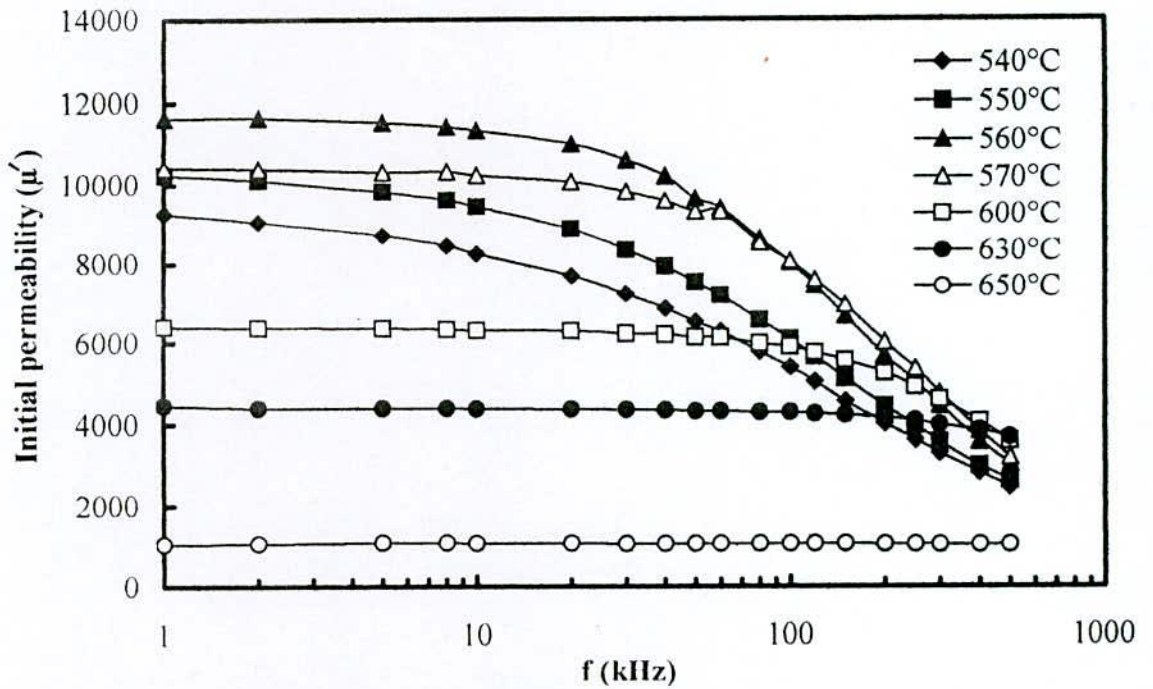

Fig.5.18   Frequency dependence of real component of initial permeability at different annealing temperature for constant annealing time 30 minutes of $Fe_{71.5}Cu_1Cr_2Nb_3Si_{13.5}B_9$ alloy
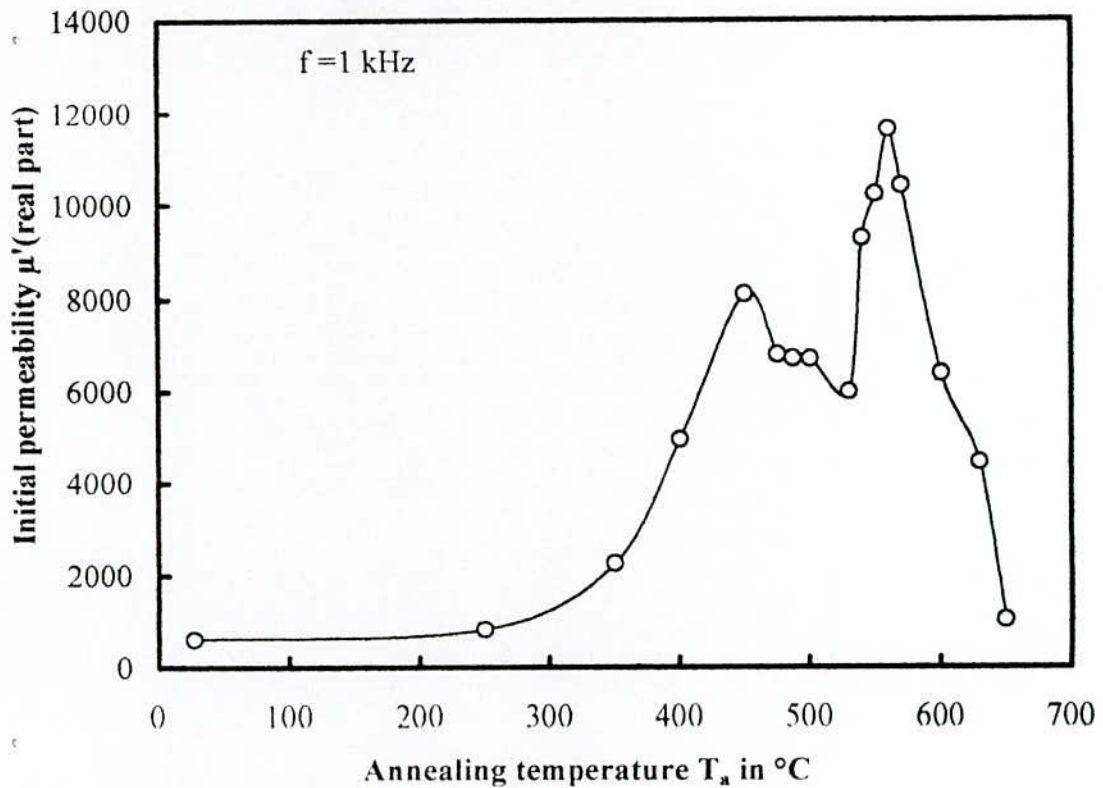
Fig.5.19　Variation of real component of initial permeability of $Fe_{71.5}Cu_1Cr_2Nb_3Si_{13.5}B_9$ alloy with annealing temperature T_a at constant frequency 1 kHz

In fig.5.19 time dependence of real part of the complex initial permeability μ' is plotted as a function of annealing temperature T_a at a fixed frequency of 1 kHz. From this graph it is easy to conclude about the strong dependence of initial permeability on annealing temperature. When annealing treatments are performed below the onset of crystallization an increase of initial permeability with annealing temperature was observed due to the relaxation of the amorphous matrix i.e. stress relief, increase of packing density of atom by annealing out micro voids and changing the degree of chemical disorder. This enhancement of μ' primarily stops at 450°C, and above 450°C permeability decreases and drops to a low value at 530°C. This is the temperature at which initiation of crystallization takes place. This decrease of permeability is due to the stress development in the amorphous matrix by growing crystallites. This act as pinning centers for the domain walls mobility. The growing crystallites are far apart from each other representing small volume fraction that can not be exchange coupled and the anisotropy can not be averaged resulting in weak inter – grain magnetic coupling. Stress

development range of this alloy is 450°C -530°C i e 80°C. Further increase of temperature above 530°C a sharp increase of μ' is observed which is associated with the nano crystallization of α-Fe(Si) phase. An enhancement of initial permeability by two orders of magnitude was observed annealed at 560°C. When the samples are annealed above 560°C, μ' drops to a lower value drastically. The probable reason might be the evolution of boride F_3B phase and nonmagnetic FCC $Cu^{(5.12)}$. At this temperature magnetic hardening takes place.

5.3.1.1 Frequency Dependence of Imaginary Part of the Complex Permeability of Composition $Fe_{71.5}Cr_2Cu_1Nb_3Si_{13.5}B_9$ Alloy with Different Annealing Temperature

The effect of annealing temperature at constant annealing time on the complex permeability and their frequency dependence for the sample composition $Fe_{71.5}Cu_1Cr_2Nb_3Si_{13.5}B_9$ are shown in fig.5.20 and fig.5.21. These results are quite complimentary to the results for the real part of the complex permeability of the sample. The usefulness of the results of the complex permeabilities lie in the determination of the relative quality factor of the sample. The complex permeability for all the annealed samples at low frequencies has relatively high value and corresponds to high loss factor and lower quality factor. The frequency dependence of μ's of the samples annealed at different temperatures can be attributed to the growth and distribution of the crystallites.

5.3.1.2 Relative Quality Factor

The frequency dependence of $\mu'/\tan\delta$ or $\mu'Q$ at constant annealing time 30 minutes with different annealing temperatures are shown in figs.5.22 and 5.23. From these two figures it is observed that relative quality factor increases with the increase of annealing temperature up to 450°C and above 450°C the quality factor decreases and attains a minimum value at 530°C. Further increase of temperature above 530°C a sharp increase of $\mu'Q$ is observed and maximum quality factor is found to be at 560°C, above this temperature quality factor again decreases. From fig.5.22 it is observed that the samples annealed at 450°C and 475°C maintains high relative quality factor covering a frequency band 5 kHz to 90 kHz.
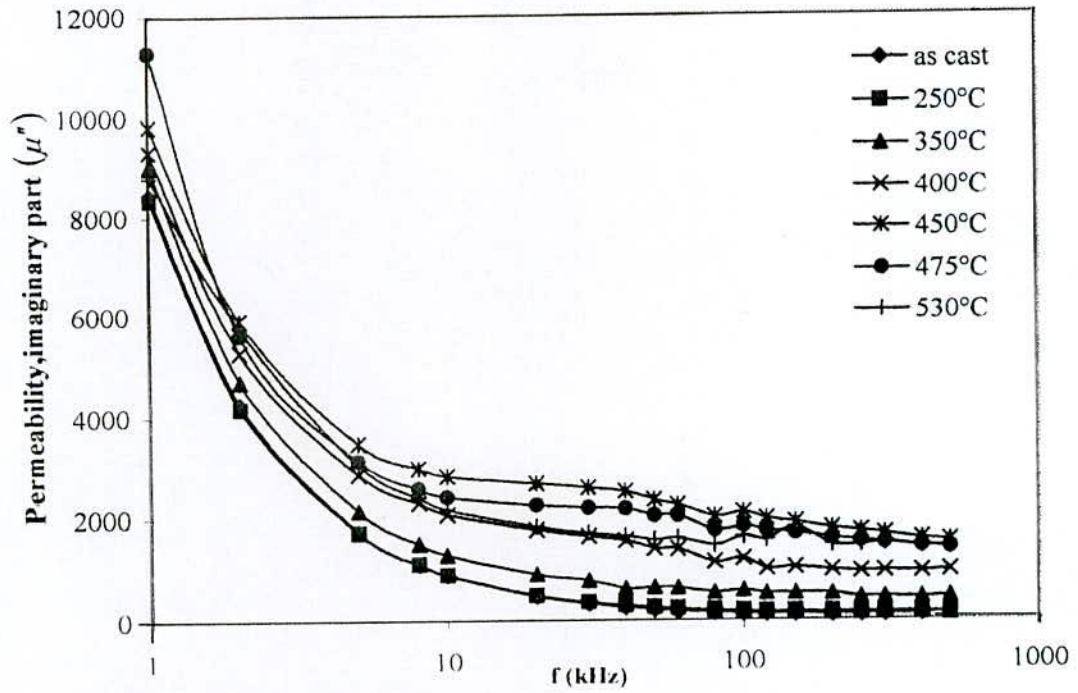
Fig.5.20   Frequency dependence of the imaginary part of complex permeability of Fe$_{71.5}$Cu$_1$Cr$_2$Nb$_3$Si$_{13.5}$B$_9$ alloy at as-cast and different annealing temperature for constant annealing time 30 minutes

Fig.5.21   Frequency dependence of the imaginary part of complex permeability of Fe$_{71.5}$Cu$_1$Cr$_2$Nb$_3$Si$_{13.5}$B$_9$ alloy at different annealing temperature for constant annealing time 30 minutes.

Fig.5.22 Frequency dependence of the relative quality factor of $Fe_{71.5}Cu_1Cr_2Nb_3Si_{13.5}B_9$ alloy at as-cast and different annealing temperature for constant annealing time 30 minutes

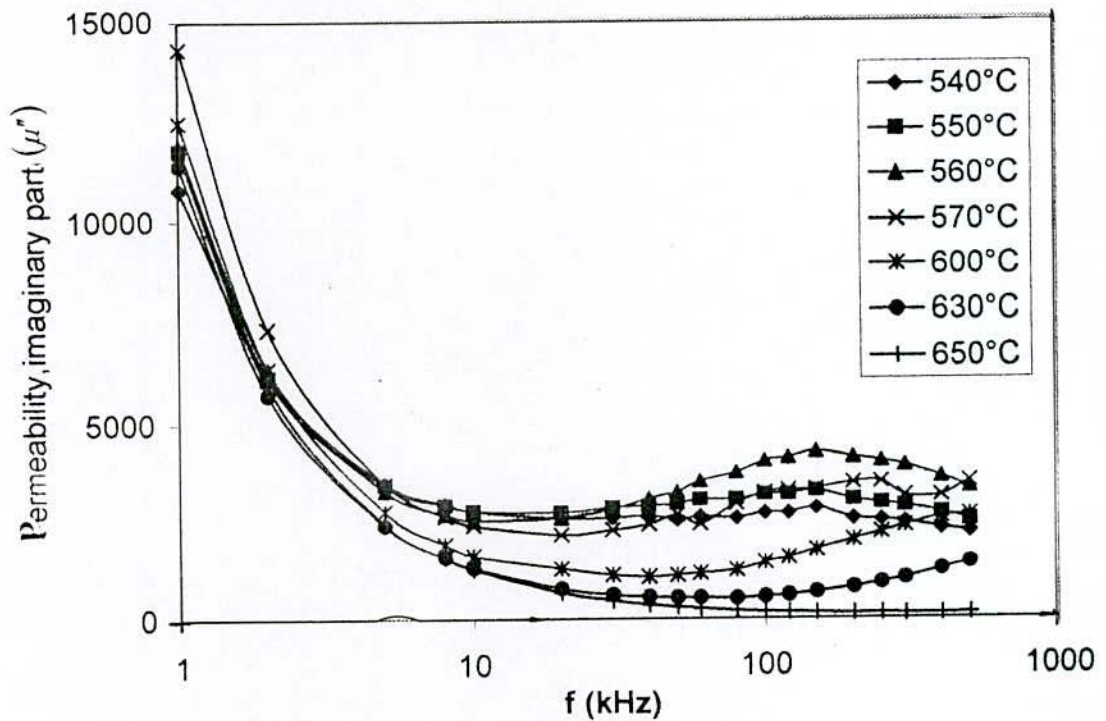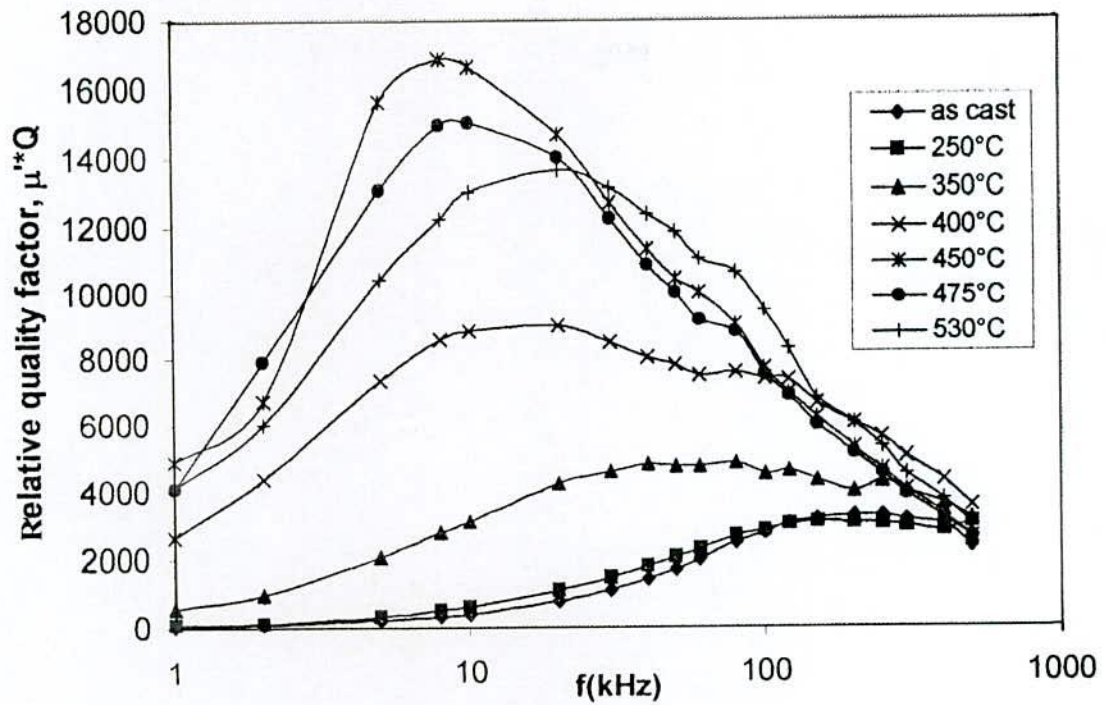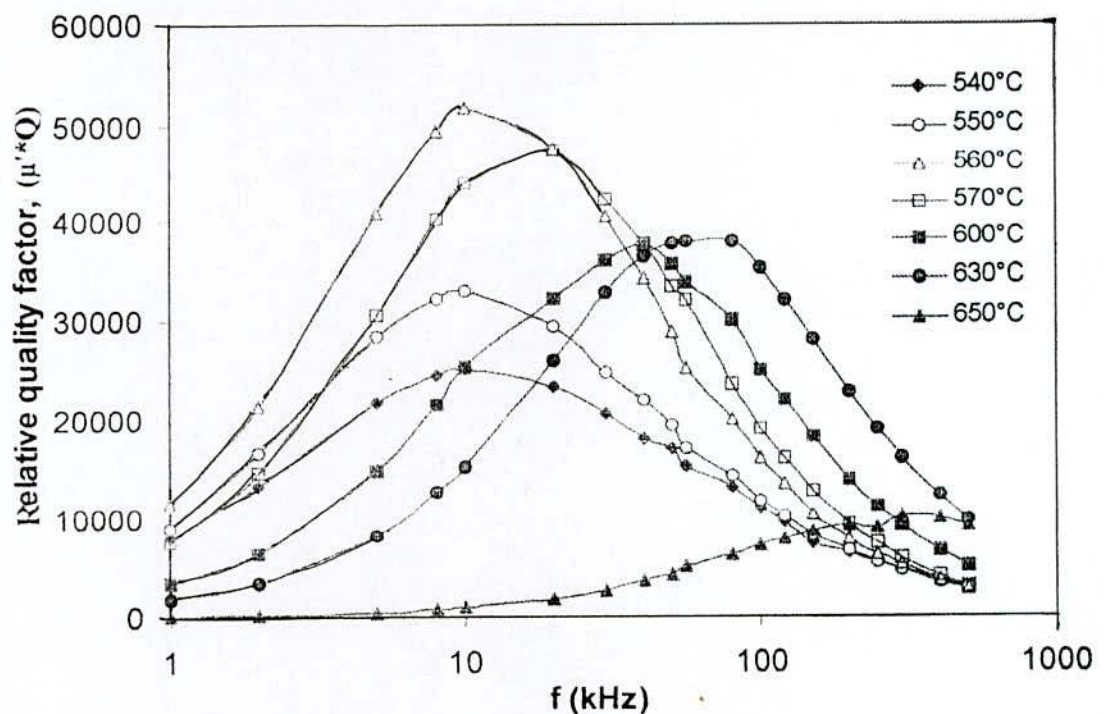Fig.5.23 Frequency dependence of the relative quality factor of $Fe_{71.5}Cu_1Cr_2Nb_3Si_{13.5}B_9$ alloy at different annealing temperature for constant annealing time 30 minutes

From fig.5.23 two frequency bands are observed one for annealing temperatures at 560°C and 570°C having maximum relative quality factor covering frequency from 5kHz to 90kHz, the other is for annealing temperatures at 600°C and 630°C covering frequency 10kHz to 100kHz and 15kHz to 150kHz.From the relative quality factor study perfect annealing temperature and frequency band can be identified at which the sample works as soft magnetic material with low loss.

5.3.2 Frequency Dependence of Initial Permeability of $Fe_{73.5}Cu_1Mo_3Si_{13.5}B_9$ Alloy with Different Annealing Temperature

Magnetic permeability for its real part has been measured in ananocrystalline sample of composition $Fe_{73.5}Cu_1Mo_3Si_{13.5}B_9$ for different frequencies in the range 1kHz to 500 kHz. The results of the as-cast sample and samples annealed at temperature in the range 300^0C to 600^0C for constant annealing time 30 minutes are shown in fig.5.24 and fig.5.25. From this graph it has been observed that the low frequency value of initial permeability increases with the increase of annealing temperature and attains the maximum value at the annealing temperature of 450°C.When the annealing temperature is higher than 450°C initial permeability decreases. This decrease of permeability may be attributed to the stress developed in the amorphous matrix by growing crystallites. At this temperature (450°C) the initiation of crystallization takes place.

Fig.5.25 shows the frequency dependence of the real part of the complex permeability at the annealing temperature from 475°C to 600°C with constant annealing time as 30 minuets. It has been observed from the graph that the low frequency value of initial permeability increases with the increase of temperature and attains the maximum value at the annealing temperature of 525°C. When the annealing temperature is higher than 525°C low frequency value of initial permeability decreases rapidly and becomes flat at 600°C as like as as cast sample. The trend of increases of low frequency permeability up to 525°C annealing temperature, i.e. maximum permeability is observed at this temperature. The greatest advantage of nano structured magnetic material lies in the freedom of tailoring its magnetic softness and hardness as also its frequency response.

From the fig.5.25 can be seen that the μ' maintains average value up to some critical frequency like 20 kHz for all the annealed samples. Above this critical frequency
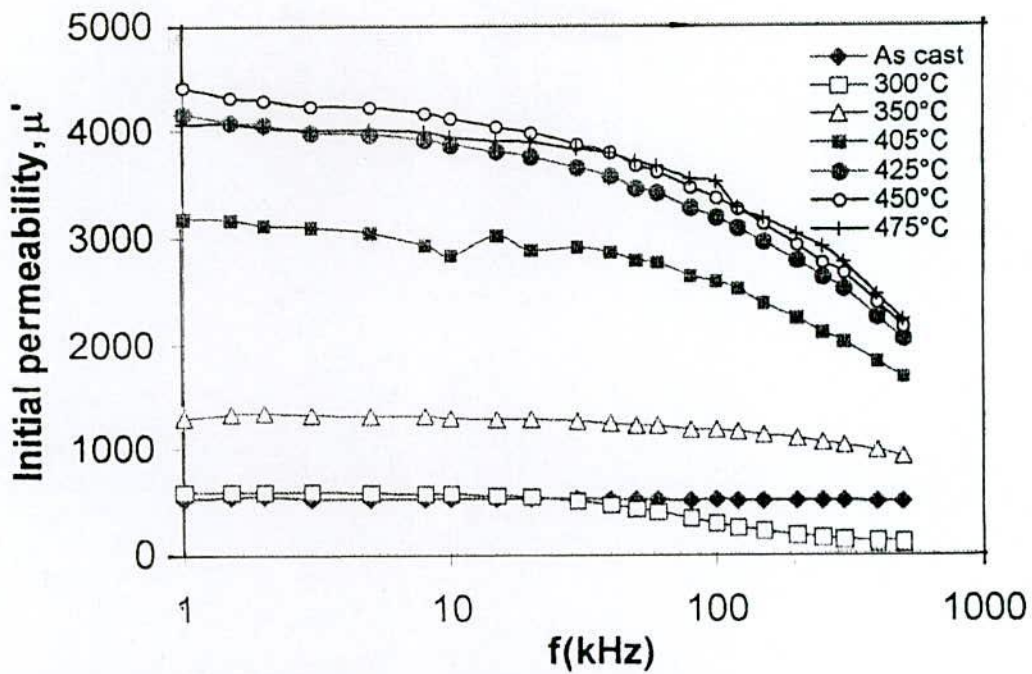
Fig.5.24   Frequency dependence of real component of initial permeability of as–cast and different annealed samples for constant annealing time 30 minutes of $Fe_{73.5}Cu_1Mo_3Si_{13.5}B_9$ alloy
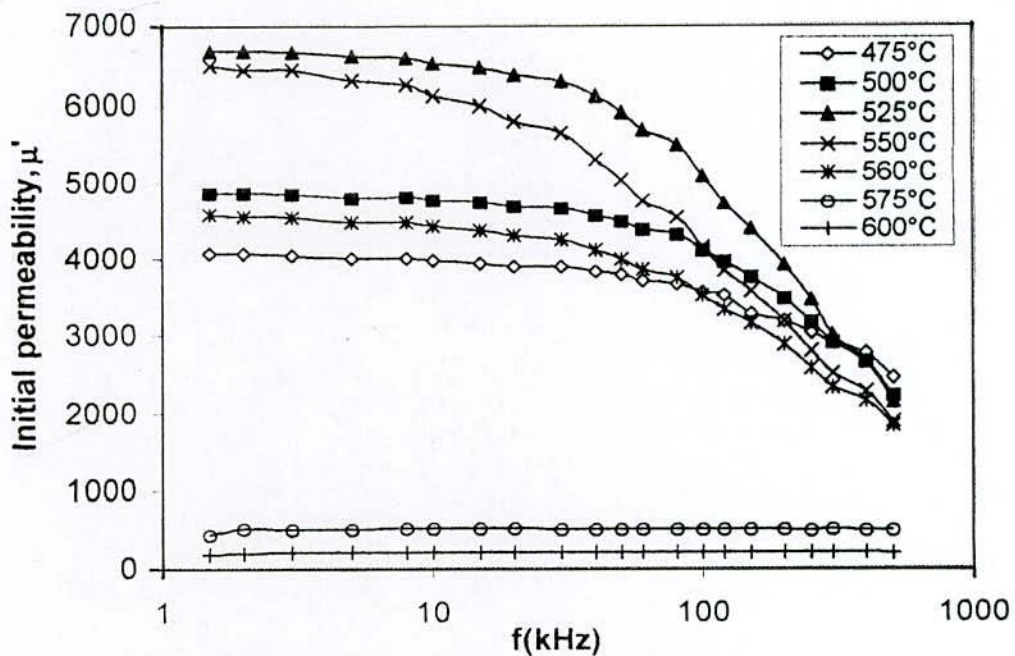

Fig.5.25   Frequency dependence of real component of initial permeability at different annealed samples for constant annealing time 30 minutes of $Fe_{73.5}Cu_1Mo_3Si_{13.5}B_9$ alloy

μ' drops rapidly due to the increase of loss component of complex permeability. From fig.5.25 the above mentioned nature has also observed for the samples annealed at 475°C to 600°C, but this critical frequency is higher than 20 kHz, it is approximately around 35kHz.
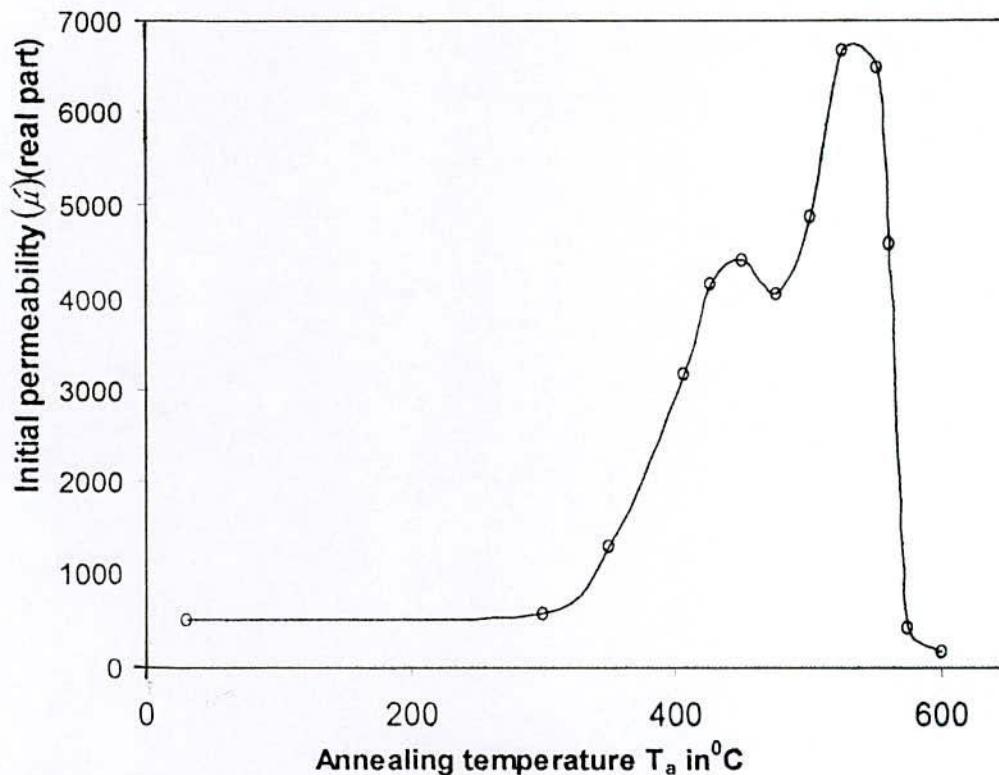
Fig.5.26   Variation of real component of initial permeability of $Fe_{71.5}Cu_1Mo_3Si_{13.5}B_9$ alloy with annealing temperature T_a at constant frequency 1 kHz

In fig.5.26 real part of the initial permeability μ' has been plotted as a function of annealing temperature T_a at a fixed frequency of 1 kHz. From this graph it is easy to conclude about the strong dependence of initial permeability on annealing temperature. When annealing treatments are performed bellow the on set of crystallization an increase of initial permeability with annealing temperature was observed due to the stress relaxation of the amorphous matrix i.e. stress relief, increase of packing density of atom by annealing out micro voids and changing the degree of chemical disorder. This enhancement of μ' primarily stops at 450°C, and above 450°C permeability decreases and drops to a low value at 475°C. This is the temperature at which initiation of crystallization takes place. This decrease of permeability is due to the stress development

in the amorphous matrix by growing crystallites. This act as pinning centers for the domain walls mobility. The growing crystallites are far apart from each other representing small volume fraction that can not be exchange coupled and the anisotropy can not be averaged resulting in weak inter – grain magnetic coupling. Stress development range of this alloy is in the range of 450°C to 475°C. Further increase of temperature above 475°C a sharp increase of μ' is observed for samples which is associated with the nanocrystallization of α-Fe(Si) phase. An enhancement of initial permeability by one order of magnitude was observed annealed at 525°C. When the samples annealed above 525°C μ' drops to a lower value drastically. The probable reason might be the evolution of boride Fe_3B phase and nonmagnetic fcc Cu. At this temperature magnetic hardening takes place.

5.3.2.1 Frequency Dependence of Imaginary Part of the Complex Permeability of Composition $Fe_{73.5}Cu_1Mo_3Si_{13.5}B_9$ Alloy

The imaginary parts of the complex permeability (μ'') at constant annealing time 30 minutes with different annealing temperature over the frequency range 1kHz to 500kHz are shown in fig.5.27 and fig.5.28. These results are quite complimentary to the results for the real part of the complex permeability of samples.

Fig.5.27   Frequency dependence of the imaginary part of complex permeability of $Fe_{71.5}Cu_1Mo_3Si_{13.5}B_9$ alloy at as-cast and different annealing temperature for constant annealing time 30 minutes

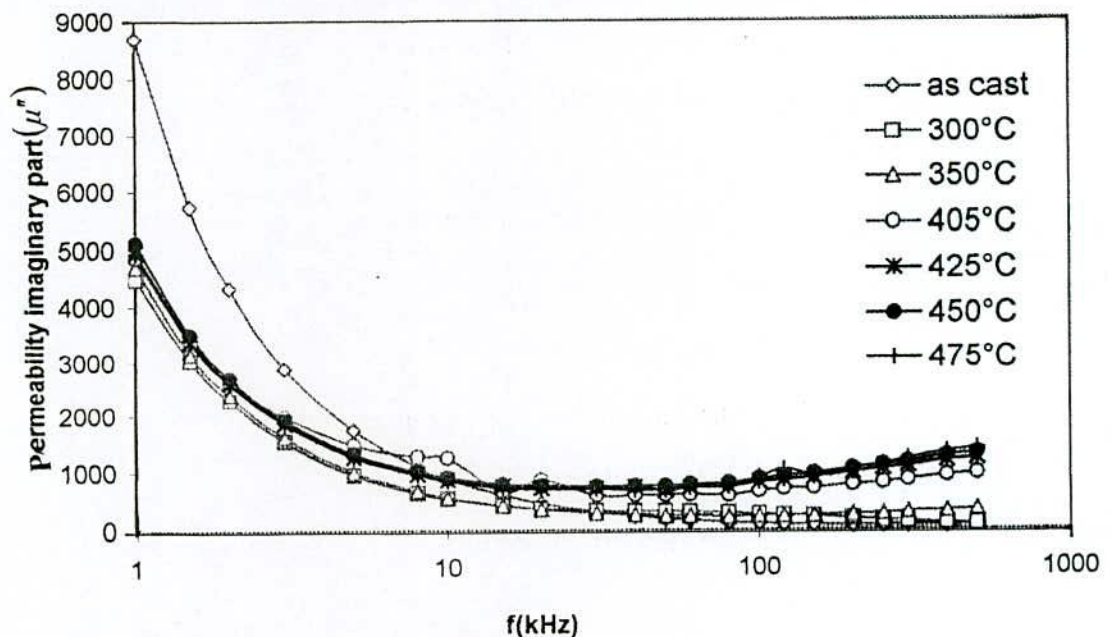Fig.5.28   Frequency dependence of the imaginary part of complex permeability of $Fe_{71.5}Cu_1Mo_3Si_{13.5}B_9$ alloy at different annealing temperature for constant annealing time 30 minutes

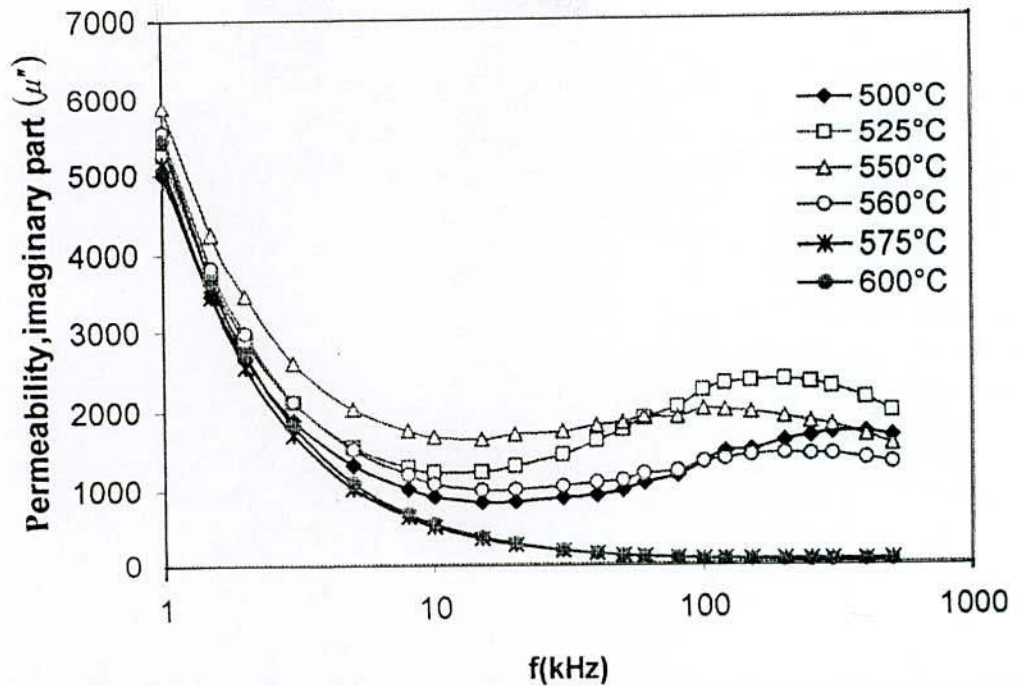The complex permeability for all samples at low frequencies has relatively high value and corresponds to high loss factor and lower quality factor as shown in fig.5.27 and fig.5.28. The μ'' increases for the annealed samples indicating higher annealing temperatures that causes further growth of crystallites and their stability.

5.3.2.2   Relative Quality Factor

The frequency dependence of $\mu'Q$ at constant annealing time with different annealing temperature are shown in figs.5.29 and 5.30. Minimum loss factor and maximum relative quality factors are the preconditions for soft magnetic materials. It is well known that optimal annealing nanocrystalline alloys display minimum loss and every high relative quality factor, $\mu'Q$ with the order of magnitude 2×10^4 to 3.5×10^4. Optimal annealing temperature is determined through successive annealing of the alloys from 300^0C to 600^0C. Fig.5.29 shows the relative quality factor increase with increasing temperature annealing up to 525^0C. Above 560^0C relative quality factor value drastically decreases. $\mu'Q$ as controlled by the real part of the complex permeability have very high values in the frequency range 5kHz to 100kHz for this nanocrystalline ribbon. In these range the sample can be useful as a soft magnetic material.
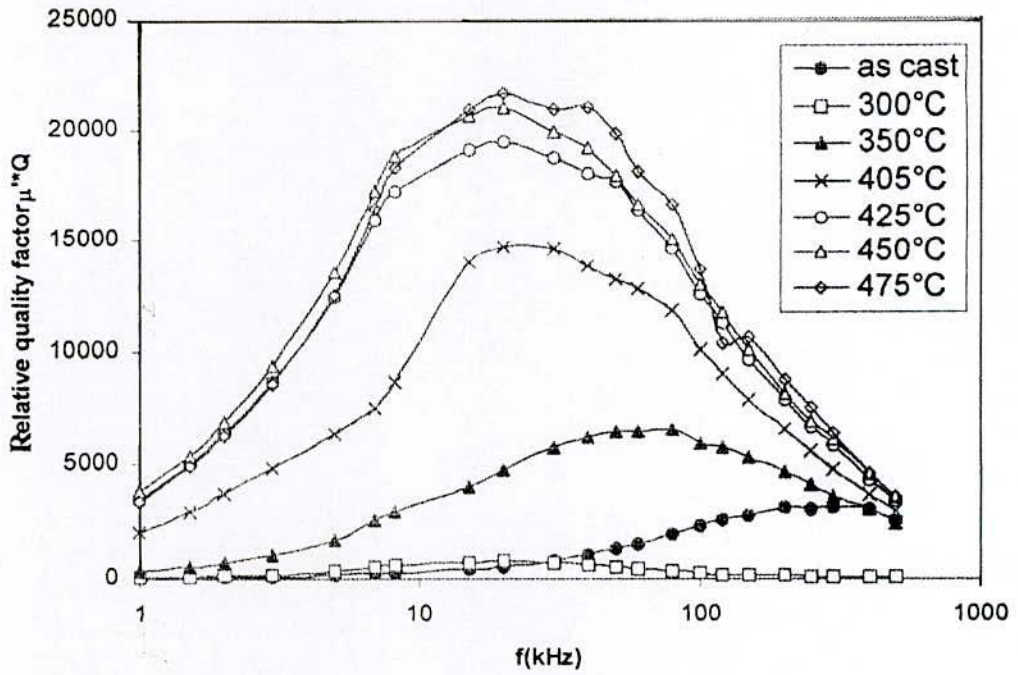
Fig.5.29   Frequency dependence of the relative quality factor of $Fe_{71.5}Cu_1Mo_3Si_{13.5}B_9$. alloy at as-cast and different annealing temperature for constant annealing time 30 minutes
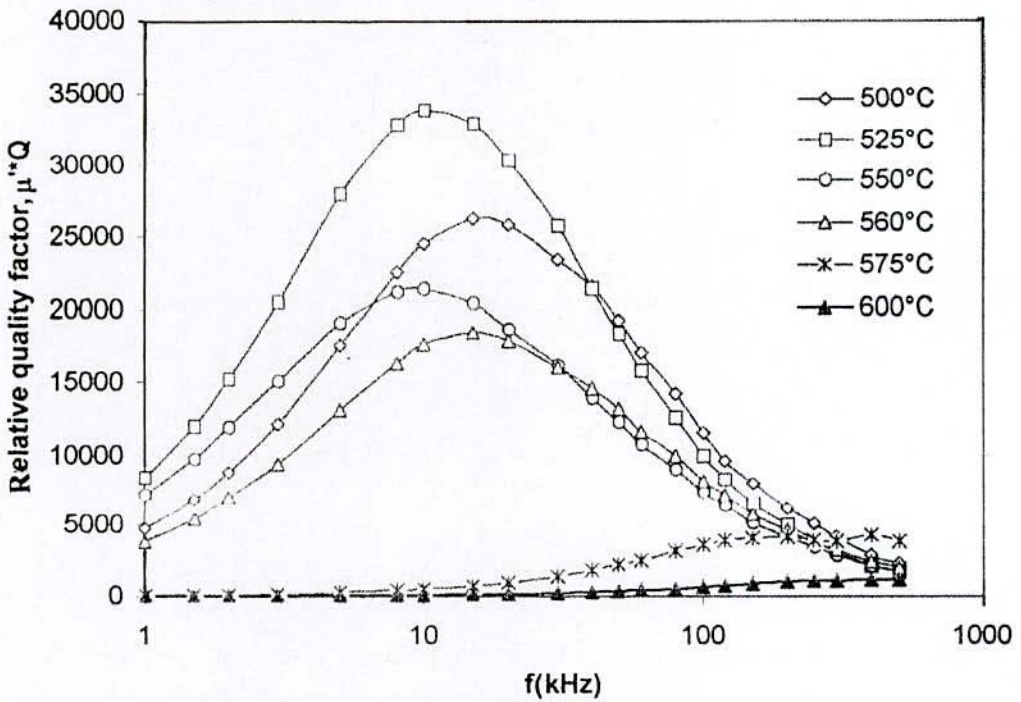

Fig.5.30   Frequency dependence of the relative quality factor of $Fe_{71.5}Cu_1Mo_3Si_{13.5}B_9$. alloy at different annealing temperature for constant annealing time 30 minutes

5.3.3 Frequency Dependence of Initial Permeability of Fe$_{71.5}$Cu$_1$W$_3$Si$_{13.5}$B$_9$ Alloy Different Annealing Temperature

Magnetic permeability for its real part has been measured in a nanocrystalline sample of composition of Fe$_{71.5}$Cu$_1$W$_3$Si$_{13.5}$B$_9$ alloy for different frequencies in the range 1 kHz to 50 0kHz. These results of the as-cast sample and samples annealed at temperature in the range 350^{0}C to 525^{0}C for constant annealing time 30 minutes is shown in fig.5.31. From this figure it has been observed that the low frequency value of initial permeability increases with the increase of annealing temperature and attains the maximum value at the annealing temperature of 425°C. When the annealing temperature is higher than 425°C initial permeability decreases. This decrease of permeability may be attributed to the stress developed in the amorphous matrix by growing crystallites. The trend of increasing low frequency permeability exist up to 425°C, i.e. maximum permeability were observed at this temperature for choosing the best soft magnetic property of these sample.
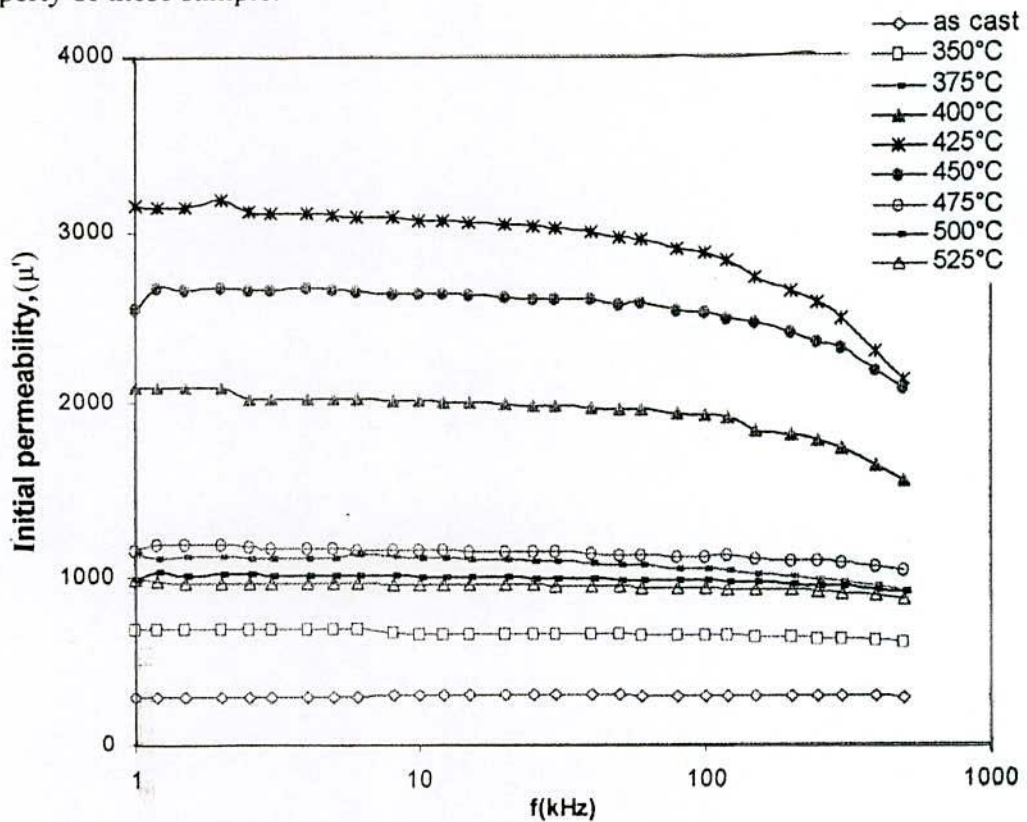

Fig.5.31   Frequency dependence of real component of initial permeability of as–cast and different annealed samples for constant annealing time 30 minutes of Fe$_{71.5}$Cu$_1$W$_3$Si$_{13.5}$B$_9$ alloy

From the fig.5.31 it has been seen that the μ' maintains average value up to some critical frequency like 100 kHz for all the annealed samples. Above this critical frequency 'μ' drops gradually due to the increase of loss component of complex permeability. In case of other two samples (with W_3 with Mo_3) it was observed that μ' decrease rapidly after the critical frequency and reaches a lowest common value at 500 kHz. But for this sample it is observed that μ' drops gradually after the critical frequency and does not meet a lowest common value at 500 kHz, which implies that loss component is not high enough for this sample at 500 kHz.
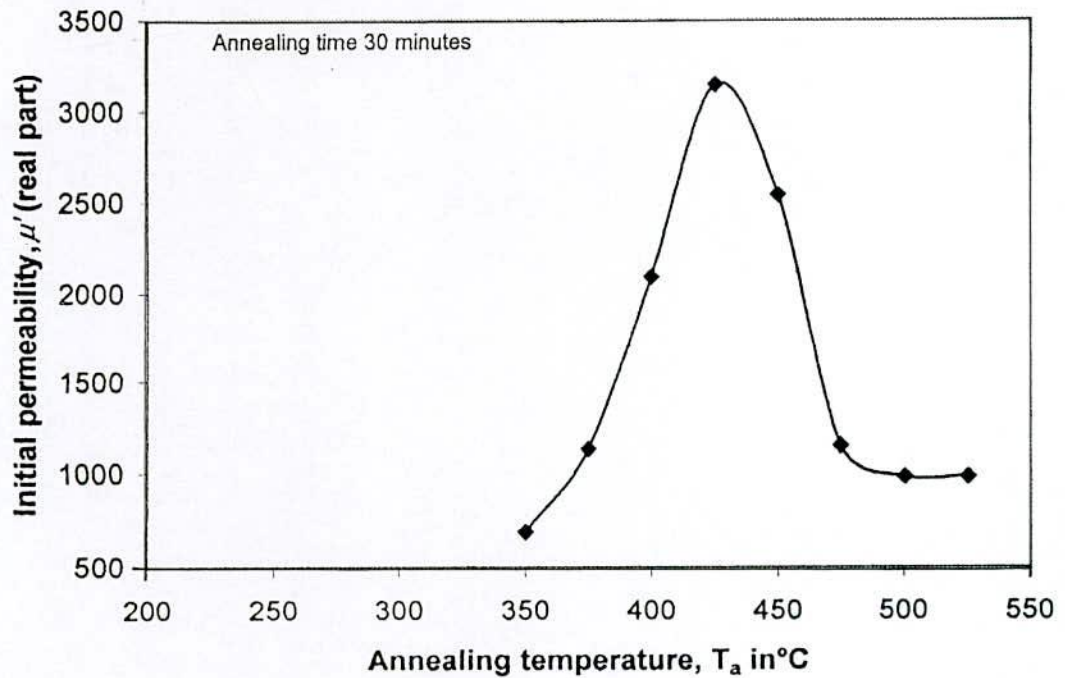
Fig.5.32   Variation of real component of initial permeability of $Fe_{71.5}Cu_1W_3Si_{13.5}B_9$ alloy with annealing temperature T_a at constant frequency 1 kHz

Fig.5.32 shows the real part of the initial permeability μ' is plotted as a function of annealing temperature T_a at a fixed frequency of 1 kHz. From this graph it is easy to conclude about the strong dependence of initial permeability on annealing temperature. When annealed treatments are performed bellow the onset of crystallization an increase of initial permeability with annealing temperature was observed due to the stress relaxation of the amorphous matrix i.e. stress relief, increase of packing density of atom by annealing out micro voids and changing the degree of chemical disorder. This enhancement of μ' primarily stops at 425°C, and above 425°C permeability decreases and drops to a low value at 500°C. Stress development range of this alloy is not observed. An

enhancement of initial permeability by one order of magnitude was observed for samples annealed at 425°C. When the samples annealed above 425°C μ′ drops to a lower value drastically.

5.3.3.1 Frequency Dependence of Imaginary Part of the Pomplex Permeability of Composition $Fe_{71.5}Cu_1W_3Si_{13.5}B_9$ Alloy

The imaginary part of the complex permeability (μ'') at constant annealing temperature over the frequency range 1kHz to 500kHz is shown in fig.5.33. These results are quite complimentary to the results for the real part of the complex permeability of the sample. The complex permeability for all the samples at low frequencies has relatively high value and corresponds to high loss factor and low quality factor. The usefulness of the results of complex permeability lies in the determination of quality factor of sample.

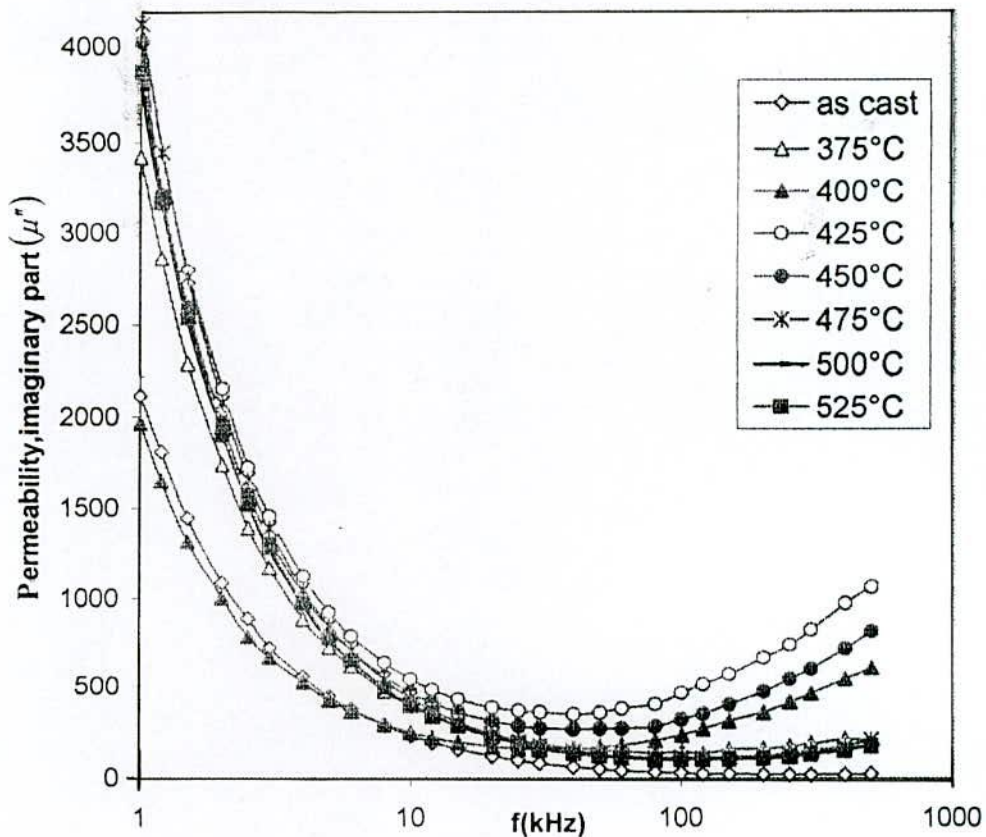Fig.5.33   Frequency dependence of the imaginary part of complex permeability of $Fe_{71.5}Cu_1W_3Si_{13.5}B_9$ alloy at as-cast and different annealing temperature for constant annealing time 30 minutes

5.3.3.2 Relative Quality Factor of $Fe_{71.5}Cu_1W_3Si_{13.5}B_9$ Alloy

The frequency dependence of relative quality factor of the different annealed samples is shown in fig.5.34. The relative quality factors as controlled by the real part of the initial complex permeability have quite high value in the range 8kHz to 200kHz for samples are annealed 400^0C to 450^0C at constant annealing time 30 minutes. This gives a choice of annealing temperature depending on the operating frequency of the specimen having composition $Fe_{71.5}Cu_1W_3Si_{13.5}B_9$. It is well known that upon optimal annealing nanocrystalline alloys display minimum loss and very high relative quality factor, $\mu'Q$ with the order of magnitude 1.5×10^4 to 2.6×10^4. Optimal annealing temperature is determined through successive annealing of the alloys from say 350^0C to 525^0C. Fig.5.34 shows the relative quality factor increase with increasing temperature annealing up to 425^0C and above 425^0C quality factor decreases. Annealing temperature for longer reduces the quality factor in general. The maximum reduction occurs when the sample is annealed at 525^0C. However it is observed that when the quality factor is lower, it is more independent of frequency.
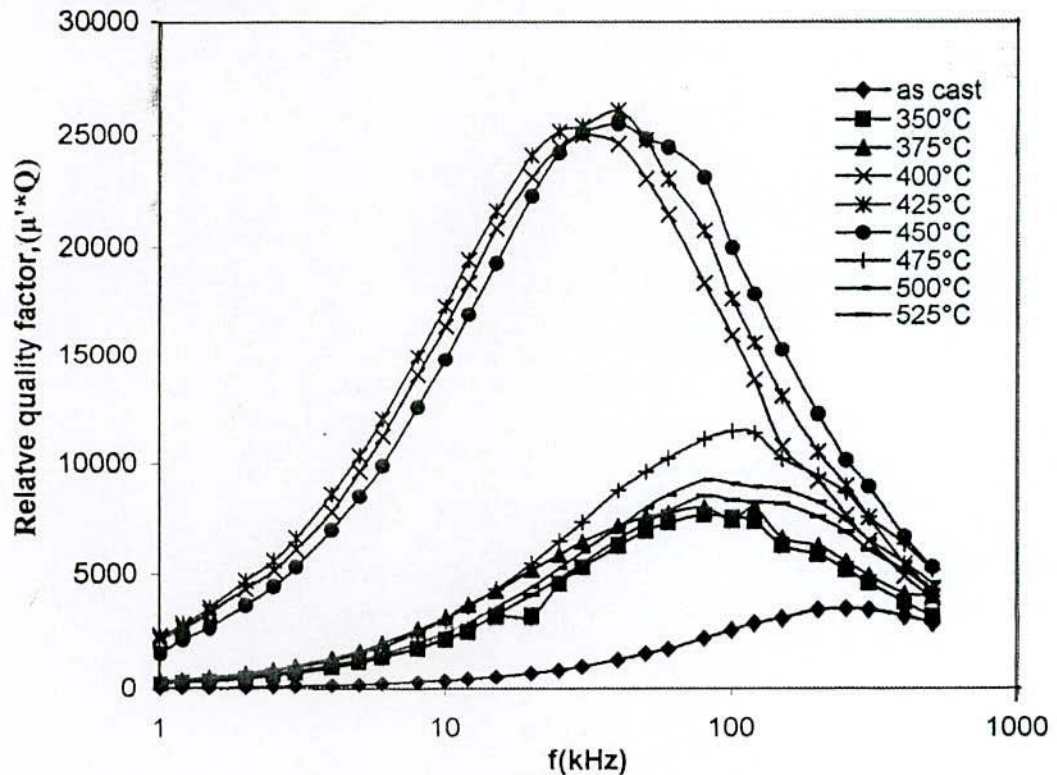

Fig.5.34   Frequency dependence of the relative quality factor of $Fe_{71.5}Cu_1Mo_3Si_{13.5}B_9$. alloy at as-cast and different annealing temperature for constant annealing time 30 minutes

5.4 Curie Temperature Measurements of $Fe_{71.5}Cu_1Cr_2Nb_3Si_{13.5}B_9$ and $Fe_{73.5}Cu_1M_3Si_{13.5}B_9$ [M = Mo & W] Alloys

Nanocrystalline amorphous ribbons of compositions $Fe_{71.5}Cu_1Cr_2Nb_3Si_{13.5}B_9$ and $Fe_{73.5}Cu_1M_3Si_{13.5}B_9$ [M = Mo & W] have been chosen for the determination of the Curie temperature (T_C) using the μ vs. T curves. Temperature dependence of ac initial permeability of the sample subjected to a heating rate $5^0 C/min$ and the constant frequency of 10kHz has been used for exciting current from a signal generator as shown in fig.5.35. The numerical values of $T_c's$ for all the samples are shown in table-5.8.

Table-5.8   Experimental value of Curie temperature

Amorphous nanocrystalline sample	Curie temperature
$Fe_{71.5}Cu_1Cr_2Nb_3Si_{13.5}B_9$	276°C
$Fe_{73.5}Cu_1Mo_3Si_{13.5}B_9$	360°C
$Fe_{73.5}Cu_1W_3Si_{13.5}B_9$	410°C

T_C is a basic quantity in the study of magnetic materials. It is corresponds to the temperature at which a magnetically ordered material becomes magnetically disordered, i.e. becomes paramagnet. T_C also signifies the strength of the exchange interaction between the magnetic atom. In fig.5.35 initial permeability increase with increase of temperature and has the maximum value at a certain point. Beyond this point there is a rapid decrease in the permeability well defined values of T_C, obtained from our measurements support the fact that in spite of chemical and structural disorder, ferromagnetic glasses have well defined magnetic ordering temperature. The sharp fall of the initial permeability are observed at 276^0C for sample $Fe_{71.5}Cu_1Cr_2Nb_3Si_{13.5}B_9$, 360^0C for sample $Fe_{73.5}Cu_1Mo_3Si_{13.5}B_9$ and 410^0C for sample $Fe_{73.5}Cu_1W_3Si_{13.5}B_9$.
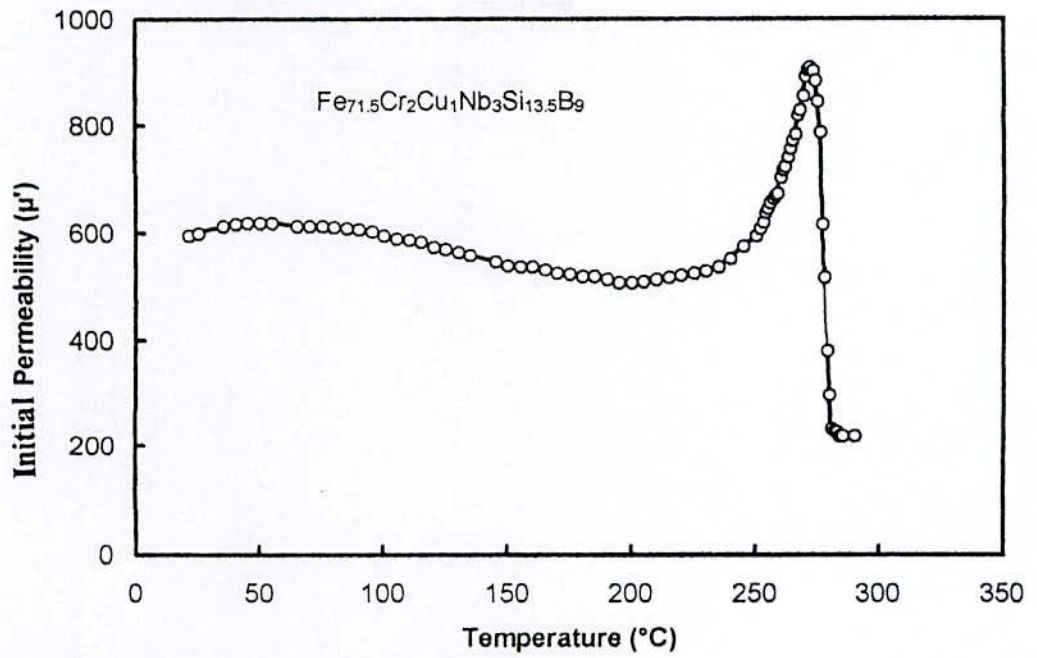
Fig.5.35 (a) Temperature dependence of initial permeability of as-cast nanocrystalline amorphous ribbon for composition with $Fe_{71.5}Cu_1Cr_2Nb_3Si_{13.5}B_9$ alloys
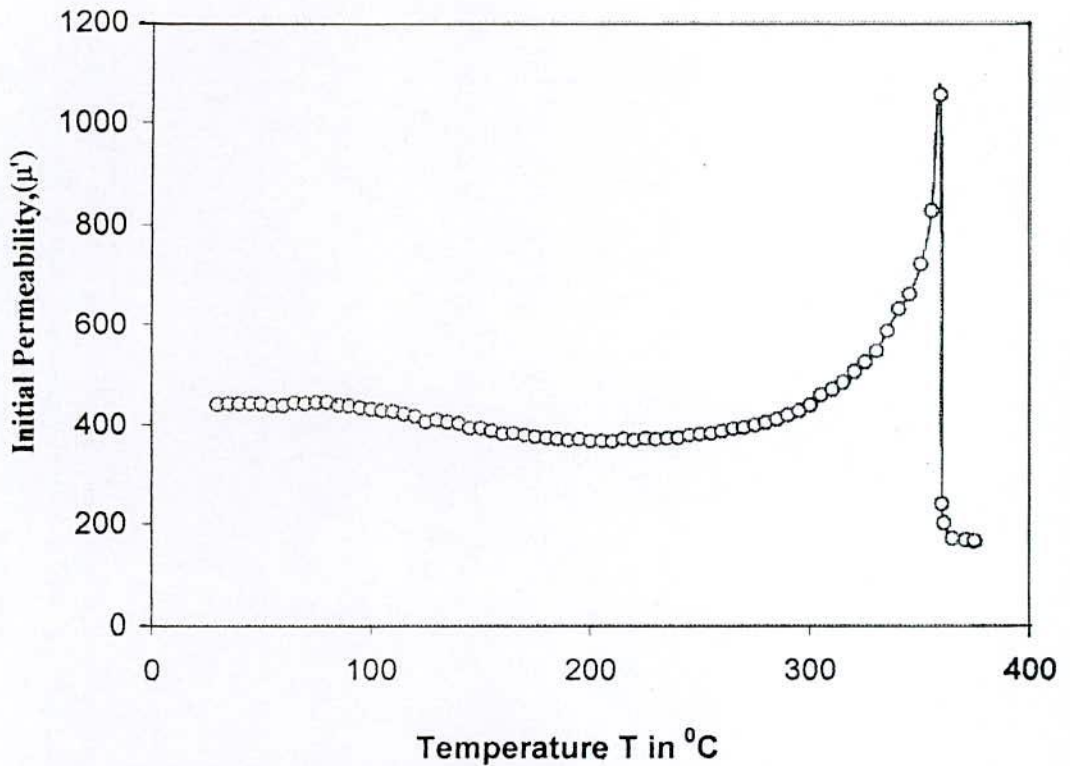
Fig.5.35 (b) Temperature dependence of initial permeability of as-cast nanocrystalline amorphous ribbon for composition with $Fe_{73.5}Cu_1Mo_3Si_{13.5}B_9$ alloys
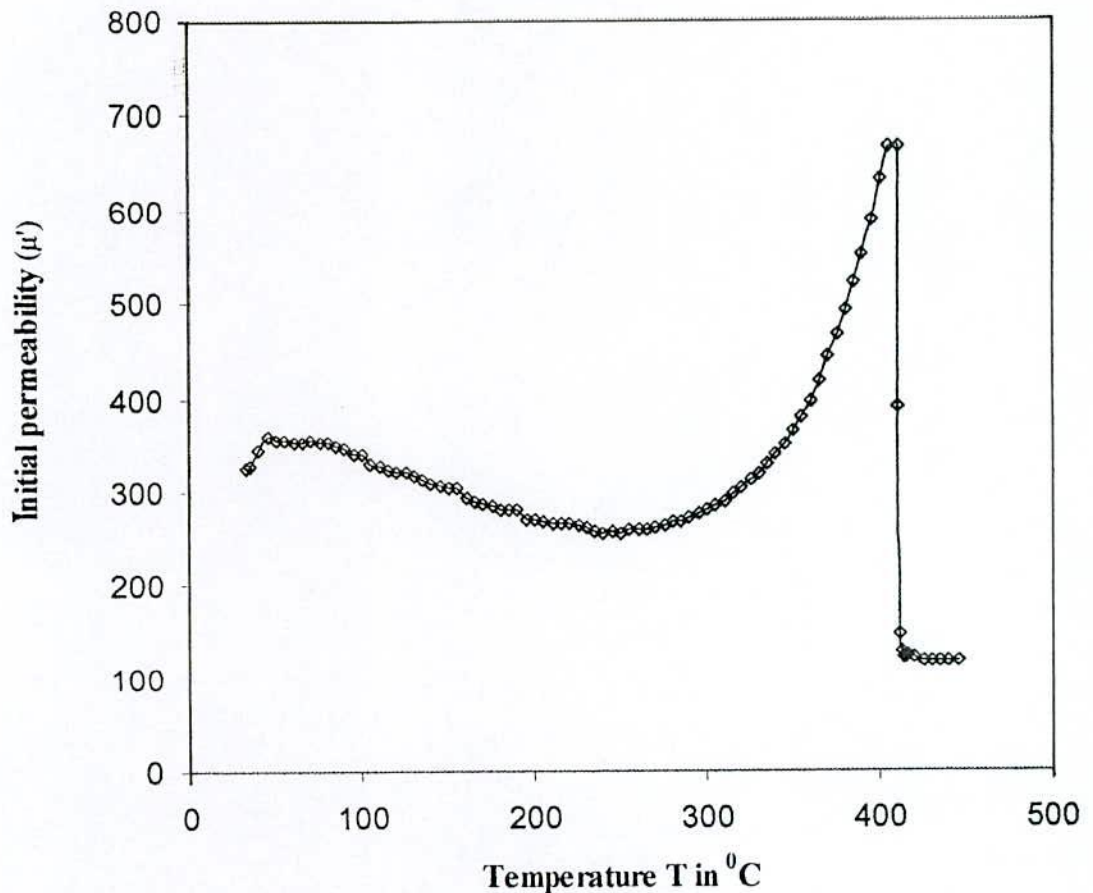
Fig.5.35 (c) Temperature dependence of initial permeability of as-cast nanocrystalline amorphous ribbon for composition with $Fe_{73.5}Cu_1W_3Si_{13.5}B_9$ alloys

From figs.5.35 (a, b, c) it is shown for temperature below 100°C no notice about effects in the glassy materials is produced [5.15]. It is interesting to note that the sharp fall of permeability at the T_c enables us to determine T_c unambiguously. The sharp fall of the permeability at T_c indicates that the material is quite homogeneous from the point to view of amorphosity of the materials. It is also observed from this curve that the permeability increases with the temperature and attains maximum value just before T_c, which we consider as Hopkinson [5.16] effect. In table-5.8 experimental value of Curie temperature of the alloys are shown. In table-5.9 Curie temperatures are shown for the nanocrystalline, which are very close to the nanocrystalline under present study. These nanocrystalline materials are only different with respect to crystallization controlling element. The curie temperatures of these nanocrystallines are taken from the survey of papers.

Table-5.9 Values of Curie temperature from some Papers

Amorphous Nanocrystalline	Curie Temperature
$Fe_{73.5}Cu_1Ta_3Si_{13.5}B_9$	$337°C$ [5.12]
$Fe_{73.5}Cu_1Nb_3Si_{13.5}B_9$	$T_c^{am} - 320°C, T_c^{cr} - 600°C$ [5.17]
$Fe_{73.5}Cu_1Nb_3Si_{13.5}B_9$	$354°C$ [5.6]
$Fe_{71.5}Cu_1Cr_2Nb_3Si_{13.5}B_9$	$273 °C$ [5.18]

Herzer [5.17] could demonstrate that after crystallization, the nanocrystalline material consists of 2 magnetic phases: one α- Fe-Si phase with the Curie temperature of about $T_c = 600°C$ and presumably a grain boundary phase with a T_c of 320°C. This later value coincides with the T_c of the initial amorphous alloy. From tables- 5.8 & 5.9 the Curie temperature of the initial amorphous alloys maintains this result except for the samples with 2%Cr and 3% W.

The experimental value of Curie temperature of the alloy $Fe_{71.5}Cu_1Cr_2Nb_3Si_{13.5}B_9$ is 276°C, which is very low from the expected value. This decrease of Curie temperature is due to substitution of 2% ferromagnetic iron by 2% Cr. The measured Curie temperature of this sample is compatible with the result of Dan et at [5.18]. There is no remarkable relation between Curie temperature and crystallization controlling element observed. The accurate determination of T_c of the amorphous material is really difficult due to irreversible components of the structural relaxation like long-range internal stress, topological and chemical short-range order. The structural relaxation without destroying the amorphous state may influence T_c. Therefore during the measurement of T_c the heating rate should be adjusted in such a way so that no substantial relaxation and crystallization takes place.

Chapter-VI

CONCLUSIONS

6. Conclusions

The early discoveries of magnetic amorphous metallic glasses, their promise for soft magnetic applications has continued to be exploited. Recently, however, a revolution in the understanding of magnetic properties on a nanoscale and the discovery of exciting new nanocrystalline magnetic material has led to new vistas for applications of these soft magnetic material. It appears that a significant need for state of the art application of soft magnetic materials will include high temperature performance of soft magnetic materials. Three sets of nanocrystalline alloys were chosen with compositions $Fe_{73.5}Cu_1Mo_3Si_{13.5}B_9$, $Fe_{73.5}Cu_1W_3Si_{13.5}B_9$ and $Fe_{71.5}Cr_2Cu_1Nb_3Si_{13.5}B_9$. These nanocrystalline alloys are as thin as 20 - 22μm in the amorphous state can be produced by melt spinning technique.

Micro structural changes and crystallization processes in Fe-Cu-M-Si-B amorphous alloys in order to elucidate the roles of combined addition of Cu and M = Mo &W to Fe-Si-B alloys. This in turn has been aimed at furthering the understanding of crystallization of FINEMET alloys. The annealed amorphous ribbons are various temperatures for 30 minutes and observed structure by XRD, crystallization by DTA and complex permeability. The B additions led to the development of two different ferromagnetic phases in the nanocrystalline alloys. From the study of kinetics and the thermodynamic stability of softest magnetic corresponded to those in which primary crystallization of α-(Fe Si) (T_{X_1}) and secondary crystallization of Fe_2B (T_{X_2}) caused magnetic hardening of the nanocrystalline alloys. The best compositions of these three experimental sample is obtained as $Fe_{71.5}Cr_2Cu_1Nb_3Si_{13.5}B_9$ in respect the highest value of T_{X_1} and T_{X_2} which are 509°C and 650°C with a heating rate $10^0 C/min$ respectively. First crystallization phase T_{X_1} indicates stability of amorphous state in respect of structural stability and magnetic ordering. Values of T_{X_1} are observed 509°C for $Fe_{71.5}Cr_2Cu_1Nb_3Si_{13.5}B_9$, 470°C for $Fe_{73.5}Cu_1Mo_3Si_{13.5}B_9$ and 460°C for $Fe_{73.5}Cu_1W_3Si_{13.5}B_9$ with a heating rate $10^0 C/min$. The advantages realized are higher saturation induction and better thermal stability with soft magnetic properties at application temperature.

The crystallization behavior of the alloy has been studied for different annealed conditions and the various crystalline phase that emerge out for each annealing condition

have been carefully identified by using XRD. The microstructure of annealed three experimental nanocrystalline sample and discussing the relationship between the initial permeability. Amorphous precursors were produced in the form of melt-spun ribbons. These were the nanocrystallized and studied by DTA. Cr additions were observed to increase the temperature of the first crystallization peak T_{x_1} while narrowing the interval between T_{x_1} and T_{x_2}. The activation energy of the samples with Mo_3 is higher than other two experimental samples with W_3 and Nb_3.

The crystalline phase of amorphous $Fe_{71.5}Cr_2Cu_1Nb_3Si_{13.5}B_9$ alloy annealed at temperature in the range of 500°C to 675°C for 30minutes is the α-Fe(Si) phase with average grain size 17 to11nm. After heating above its crystallization temperature α-Fe(Si) nanometric crystallites with average grain grown in the amorphous matrix are 14 to18nm for $Fe_{73.5}Cu_1Mo_3Si_{13.5}B_9$, and 28 to32 nm for $Fe_{73.5}Cu_1W_3Si_{13.5}B_9$.The average grain size is much smaller than that of grains usually obtained by crystallizing conventional metallic glasses (100 to1000 nm). We have also examined the influence of heating on the magnetic properties of FINEMET related alloys $Fe_{73.5}Cu_1Mo_3Si_{13.5}B_9$, and $Fe_{73.5}Cu_1W_3Si_{13.5}B_9$ with contrary observations. The effects of Cr addition for Fe in FINEMET alloys of composition $Fe_{71.5}Cr_2Cu_1Nb_3Si_{13.5}B_9$ were also observed to reduce the primary nanocrystallite grain size and to decrease the Curie temperature. The volume fraction and Si-content of the α-Fe(Si) phase increases with increment of the annealing temperature up to certain level for all the samples. According to our experimental results, when alloys are annealed in a certain temperature range 525 to 675°C for Cr-based, 525 to 650°C for Mo-based and 475 to 550°C for W-based samples, the size of α-Fe(Si) grain remains essentially constant.

The improvement of magnetic properties with increase of annealing temperature is mainly connected with the microstucture i.e. with the certain of free randomly oriented bcc α-Fe(Si) grains in the residual matrix. The increase of the permeability with increasing annealing temperature is connected with more effective averaging out of the magnetocrystalline anisotropy due to the increase of the nanocrystalline phase with nanometric grain as well as decrease of the magnetstriction constant. The improvement in

the soft magnetic properties can be ascribed to the much refined grain structure obtained at temperature annealing conditions. When alloys has been annealed for 30 minutes ar various temperatures, the maximum initial permeability (μ') were observed at $T_a = 560^0C$ for $Fe_{71.5}Cr_2Cu_1Nb_3Si_{13.5}B_9$, $T_a = 525^0C$ for $Fe_{73.5}Cu_1Mo_3Si_{13.5}B_9$ and $T_a = 425^0C$ for $Fe_{73.5}Cu_1W_3Si_{13.5}B_9$. These temperatures are corresponds to a maximum initial permeability and to lowest high frequency losses. It has been found that the relative initial permeability at 1KHz increases from 7000 to 11000 for Cr-based sample, 4000 to 6800 for Mo-based sample and 2000 to 3200 for W-based sample with increasing annealing temperature.

There is an increase of initial permeability with increasing annealing temperature due to the removal of defects and inhomogeneity but with further increase of annealing temperature the initial permeability decreases due to nucleation of crystallites and their growth. These nanocrystalline alloys are suitable for magnetic core in the pulse transformer, which works well at frequencies of 5 to 50KHz for Cr-based, 5 to 75KHz for Mo-based and 4 to 100KHz for W-based nanocrystalline sample. For technological uses of nanocrystalline materials at elevated temperature and for magnetic stability it is important to look for compositions that give higher values of T_c. The T_C of 276^0C for Cr-based, 360^0C for Mo-based and 410^0C for W-based maintained amorphous nanocrystalline samples. The observed T_C of the intergranular amorphous phase to remain relatively invariant during the crystallization process.

These soft magnetic properties required for rotor applications in the more electric aircraft are in some sense less restrictive than those for applications of FINEMET. Permeabilities of 10^2 to 10^3 are sufficient for their application require these permeabilities to only 1KHz. On the other hand, large inductions at temperature between 450^0C to 550^0C are an important requirement which seemingly eliminate all experimental sample. Promising initial results on FINEMET alloys suggest that they might also find their way in high temperature soft magnetic applications. The playground of microstructural engineering of soft magnetic properties will undoubtedly after new discoveries for future materials scientists and engineers.

Further work with finer variation of experimental composition can be useful in detailing out the effect of nanograin forming material in magnetic characteristics. Certain important parameters like magnetic anisotropy, magnetization and magnetostriction need to be studied in detail for their heat treatment. Mössbaur study will provide information regarding the distribution of the iron atoms, the hyperfine fields, phased formed in annealing of FINEMET alloys and subspectra of various Fe present in the DO_3 structure.

REFERENCES

Chapter 1

1.1   Chikazumi, S. and Stanly H Charap; Physics of Magnetism, John Wiley and Sons, Inc., New York, London, Sydney. pp 12-13, 1964

1.2   Duwez, P., R.H. Willens and W. klement; 1960, J. Appl. Phys. 31, 1136

1.3   Simpson, A.W. and D.R. brambley; 1971, Phys stat. Sol.(b) 43,291

1.4   Warlimont, H., Mater. Sci. Eng. 99 (1988) 1

1.5   Egaml, T., Rep. Prog. Phys. 47 (1984) 1601

1.6   O'Handley, R.C., J. Appl. Phys. 62 (1987) R15

1.7   Herzer, G. and H. R. hilzinger, Phys. Scripta T24 (1988)22

1.8   Konczos, G., E. kisdi-koszo and A. Lovas Phys. Scripta T24 (1988)42

1.9   Herzer, G. and H. R. hilzinger, in: Proc. Symp. on Magnetic Properties of amorphous Metals, Benalmadena 25-29 May 1987 (North- Holand. Amsterdaam. 1987) P. 354

1.10   Anantharaman, T.R. and C. Suryanarayana. Rapidly Solidified Metals – Atechonological Overview. Trans. Tech. Publ. (1988)

1.11   Yoshizawa, Y., S. Oguma and K. Yamauchi, J. Appl. Phys. 64(1988), P. 6044 Abstract-INSPEC/Order Document/ Order Document/ Full Text Via Cross Ref/ Abstract+ References in Scopus/Cited By in Scopus

1.12   Yoshizawa, Y. and K. Yamauchi, IEE Trans. Magn. 25(1989), P. 3324. Abstract-INSPEC/Order Document/ Order Document/ Full Text Via Cross Ref/ Abstract+ References in Scopus/Cited By in Scopus

1.13   Vacuum schmelze GmbH, Troidal Cores of VITROPERM, Data Sheet PW-014 (1993)

1.14   Herzer, G., IEEE Trans. Magn. 25; (1989) 3327

1.15   Herzer, G., IEEE Trans. Magn. 26; 1397 (1990)

1.16   Hono, K., K. Hiraga, Q. Wang, A. Inoue, T. Sakurai, Acta Metall. Mater 40(1992)2137

1.17   Kim, H., M. matsuura, M. Sakurai, K. Suzuki, Jpp. J. Appl. Phys. 32 (1993) 676

1.18   Sakurai, M., M. matsuura, S. H. Kim, Y. Yoshizawa, K. Yamauchi, K. Suzuki, Mater. Sci. Eng. A179/180 (1994) 469

1.19   Ayers, J.D., V.G. Harris, J.A. Sprague, W.T. Elam, Appl. Phys. Lett 64 (1994) 974

1.20 Yoshizawa, Y. and K. Yamauchi, Paper AQ2, Digest Intermag Conf. (28-31 March 1989) Washington

1.21 Alben, R., J.J. Becker, M.C. Chi; j. Appl. Phys. 49(1978) 1653

1.22 Harnando, A., M. Vajquez, T. kulik and C. Prados; Phys. Rev. B 51 (1995) 1381

1.23 Harnando, A., T. kulik; Phys. Rev. B 49 (1994) 7064

1.24 Grossinger, R., D. Holzer, C. Ksshach, H. Sassic, R. Sato Turtelli, J. P. Sinnecker and E. Witting; J. Magn. Magn. Mater; in Press

1.25 Noh, T.H., M.B. Lee, H.J. Kim, I.K. Kang; J. Appl. Phys. 67 (1990) 5568

1.26 Herzer, G., H. Warliment; Nanostucture Mater. I (1992) 263

1.27 Vazquez, M., P. Marin, A.O. Olofinjana, H.A. Davies; Mater Sci. Forum 179-181 (1995) 521

1.28 Kollar, P., J. Fuzer, P. Maa, T. Svec and, M. Konk; J. Magn. magn. Mater, 157-158 (1996) 213

1.29 Kulik, T., A. Harnando; Magn. Magn. Mater 160 (1996) 269

1.30 Conde, C.F. V. Franko, A. Conde, Inip. Duhaj, P. mrafko, P. Svec(Eds); Rapidly Quenched and Metastable materials, Elsevier, Amsterdam, (1997) P. 254

1.31 Slawska-Waniewska, A., M. Gutowski, H.K. Lochowiez, T. Kulik and H. Matyza; phys.Rev.B 46 (19920)

1.32 Herzer, G. and H.R. Hilzinger; J. Magn. Mag. Mater. 62, 143

1.33 Herzer, G. and H. R. Hilzinger. Physca. Scripta 1989; 39: 639

1.34 Herzer, G, J. Mag.Mag.Mat. 1992; 112: 258

1.35 Coey, JMD, Rare-earth iron permanent magnets. Oxford: Oxford Science Publications, Clarendon Press, 1996

1.36 Kneller, EF, Hawig R. IEEE Trans. Mag. 1991; 27: 3588

1.37 Skomski, R, Goey JMD; Phys. Rev. B 1993; 48:15812

1.38 Kulik, T., Antonio Hernando and Manual Vazquez; J. Magn. Magn.; 133 pp. 310-313, 1994

1.39 Duhaj, P., P. Svec, D. Jamoclpvic, I. Mako and M. Hlasnik, Mat. Sci. Eng. B 14(1992) pp 357

1.40 Sikder, S. S. and M. A. Asgar, Thermochimika Acta, Vol. 326, pp. 119-126,1999

1.41 Asgar, M.A. and S.S. Sikder; Indian J. Phys., vol. 73a(4), pp. 1-10; 1999

1.42 Estevez Rams, E., J. Fidler, M. Dahlgren, R. Grossinger, M. Knobel, P. Tiberto, P. Alia and F.vinal; J. phys. D; Appl. Phys. 29(1996) 848-854

1.43 Yshizawa, Y., K. Yamauchi, T. Yamane, H. Sugihara, J. Appl. Phys. 64 (1988) 647

1.44 Yoshizawa, Y. and K. Yamauchi; 1990a, Mater. Trans. JIM 31,307

1.45 Herzer, G., IEEE Trans. Magn. 25; (1989) 2227

1.46 Herger, G., Proc. Inst. Symp. 3-d Transition semi metal Thin Film Magnetism and Processing, Sedi, japan (1991)

Chapter 2

2.1 Duwez, P., J Am Inst. Metall Eng 1951; 191:765

2.2 Duwez, P., R.H. Willens and W. klement; 1960, J. Appl. Phys. 31, 1136

2.3 Duwez, P, Trans Am SOC Met 1967; 60:607

2.4 Duwez, P, Ann Rev Mat Sci 1976; 6:83

2.5 Mader, S, Nowick As. Appl Phys Left 1965; 7:57

2.6 Tsuei, C. C., P. Duwez, J Appl Phys 1960; 37:435

2.7 Yshizawa, Y., S. Oguma and K. Yamauchi, J. Appl. Phys. 64 (1988) 6044

2.8 Yshizawa, Y., K. Yamauchi, T. Yamane and H. Sugihara, J. Appl. Phys. 64 (1988) 6047

2.9 Kojima, A., H. Horikiri, Y. Kamamura, A. Makino, A. Inoue, T. Matsumoto, Mat Sci Eng 1994; A179/A180:511

2.10 Mizoguchi, T., IBM Research report, RC 6054, 1976

2.11 Alben, R., J.I. Budnic and G.S. Gargill; α_{111} Metalic Glasses, " American SOC. for metals", pp.304, 1978

2.12 Yoshizawa, Y. and K. Yamauchi; 1990a, Mater. Trans. JIM 31, 307

2.13 Hono, K. and T. Sakuria; 1995, Appl. Surf. sci. 87-88, 116

2.14 Hono, K., K. Hiraga, Q. Wang, A. Inoue and T. sakuria; 1992, Acta meall. Matre. 40, 2137

2.15 Ayers, J.D., V.G. Haris, J.A. Sprague and W.T. Elan; 1994, Appl. Phys. Lett. 64, 974

2.16 Koster, U., M. Schonemann, B. Bewersdorft, S. Brauer, M. Sutton and G.B. Stephenson; 1991, Mat. Sci. Ing. A133,611.

2.17 Herzer, G; 1991, In: Proc. of Int. Symp. on 3ab Transiton-Semi Metal Thin Flimss, Magnetism and Processing (Japan Soc for the Promotion of Science,131committee, Sendia, Japan) p. 130

Chapter 3

3.1   Trunball, D.; J. de Physique, vol.35, C4-1,1974.

3.2   Takayama, s.; J. Materials Sci, vol.11, pp.164,1976.

3.3   Cohen, M.H. and D. Turnbull; Nature vol.189, pp.131, 1961.

3.4   Gargil, III. G.; 1970, J. Appl. Phys, 41. 2248.

3.5   Chen, H.S.; 1974, Acta Met. 22, 1505.

3.6   S.R. and J. Taue; 1975, Phys. Rev. Lett. 35, 380.

3.7   Laborskey, F.E.; J. Magn. and Magn. Matter, vol. 7, pp. 143, 1987

3.8   Kissenger, H.E.; 1957, Anal, Chem. 29, 1702

3.9   Boswell, F.G.; 1980, J. Thermal Anal 18, 353

3.10   Chrissafis etal. Journal of Alloys and Components, 386 (2005) 165-173

3.11   H.E Kissinger. J. Rss. Nat. Bur. Stand. 57 (1956) 217

3.12   Cullity, B.D.; Elements of X-ray diffraction; Reading, M.A : Addisonwesley,1978

3.13   Yoshizawa, Y. and K. Yamauchi; 1990a, Mater. Trans. JIM 31,307

3.14   Hono, K. and T. Sakuria; 1995, Appl. Surf. sci. 87-88, 116

3.15   Sikder, S.S., M.A. Asgar and M.A. Hakim; Indian J. Phys. 73A 639 (1999)

3.16   Irvine, J. T. S., E. Amano, A. Huanosta, R. Valenzuela and A. R. Wesf; Solid State Ionies 40/41, 220, (1990)

1.17   Bozorth, R; 1951 Ferromagnetism (D. Van nostrand, Princeton N.J.) p. 76

Chapter 4

(4.1)   Chatelier, H. Le.; Bull SOC. France. Mineral, Vol. 10, pp. 204, 1887

(4.2)   Pearson, W. B.; A Handbook of Lattice spacing and Structures of Metals and Alloys (Oxford Pergamon) 1958

Chapter-5

5.1   Clements, W.G. and B. Cantor, 1976,in Rapidly quenched metals, Section-1, (eds.N.J.Graut and B.C. Giessen)(MIT Press Cambridge, Mass) P.267

5.2   Luborsky, F.E., Materials Sci. Engg-28 (1977), P.139

5.3   Kissinger, H. E., J. Res. Nat. Bur. Stand. 57(1956) 217.

5.4   Illekova, E., Thermocin. Acta 280-281 (1996), 289

5.5 Bigot, J., N. Lecaude, J. C. Perron, C. Milan, C. Ramiarinjaona, J. F. Rialland, Journal of Magnetism and Magnetic Materials 133(1994) 299-302

5.6 S. Noor, M. Phil Thesis, March 2005, KUET, p 99

5.7 Hoa, N. Q., N. Chau, H.D. Anh, N.H. Luong, M.A. Asgar, Sh. Sh. Sikder, Md.S. Mahmud, Proceedings of the Seventh Vietnames-German Seminar on Physycs and Engineering, Halong City, from March, 28 to April, 5, 2004

5.8 Nguyen Xuan Phuc, Ngo Quang Thang, Nguyen Huy Dan and Nguyen Hoang Nghi unpublished

5.9 Chen, C. L. and R. S. Hasegwa; ibid, vol. 49, pp. 1721, 1978.

5.10 Morjani, K., S. K. Chatak, R. V. Rao, B. Kramer and H. S. Chen; International Conference on liquid and amorphous metal, Grenomle, Franch, 1980

5.11 Pearson, W. B.; A Handbook of Lattice Spacings and Structures of Metals and Alloys (Oxford Pergamon) 1958

5.12 Hakim, M. A., S. Manjura Huq, Journal of magnetism and magentic materials, 284, 2004, p400

5.13 Brzozka, K., A. Slawska-Waniewska, M. Gawronski, K. Jezuita, H. K. Lachowicz, J. Magn. Magn. Mater. 140-144 (1995) 481

5.14 Franco, V., C. F. Conde, A. Conde, J. Magn. Magn. Mater 185 (1998) 353

5.15 Luborsky, F. E., J. J. Decker & R. O. McCary, IEEE Trans. Mag. 11, 1644, 1975

5.16 Kersten, M., Z, Angew, Phys. 7, 313 (1956), 8, 382, 496 (1956)

5.17 Harzer, G., paper AQ3, Digest Intermac Conf. (28-31) March 1989, Washington, U.S.A.

5.18 Dan, N. H., N.X. Phuc, N.Q. Thang and N.H. Nghi, Proceedings of 7th Asia Pacific Physics Conferene, 19-23 august 1997,Beijing, China

Publications

1. The study of temperature dependence of magnetization in nanocrystalline materials with composition $Fe_{73.5}Cu_1Si_{13.5}B_9M_3$ [M=Mo,Cr&W] - **P.K. Roy**, S.S. Sikder & M.A. Asgar, Biennial Symposium on Physics and Modern Development, Organized by Bangladesh Physical Society, Atomic Energy Centre Dhaka, Bangladesh, 30-31 March, 2002, **31,** p 18

2. Ultra-Soft magnetic behavior and initial permeability of nanocrystalline $Fe_{71.5}Cr_2Cu_1Nb_3Si_{13.5}B_9$ alloy - **P.K. Roy**, Md. Sultan Mahmud, S.S. Sikder, M.A. Hakim & Manjura Haque, Annual Conference Organized by Bangladesh Physical Society, Bangladesh University of Engineering and Technology (BUET), Dhaka 1000, Bangladesh, 04 – 05 May, 2007, **P-21,** p 54

3. Influence of annealing temperature on the nanocrystallization and initial permeability of $Fe_{73.5}Cu_1Mo_3Si_{13.5}B_9$ alloy - **P.K. Roy**, S.S. Sikder, M.A. Hakim & S. Manjura Haque, Annual Conference Organized by Bangladesh Physical Society, Bangladesh University of Engineering and Technology (BUET), Dhaka 1000, Bangladesh, 04 – 05 May, 2007, **IV-CP-12,** p 23